ISBN 978-82-326-8064-1 (printed ver.)
ISBN 978-82-326-8063-4 (electronic ver.)
ISSN 1503-8181 (printed ver.)
ISSN 2703-8084 (electronic ver.)

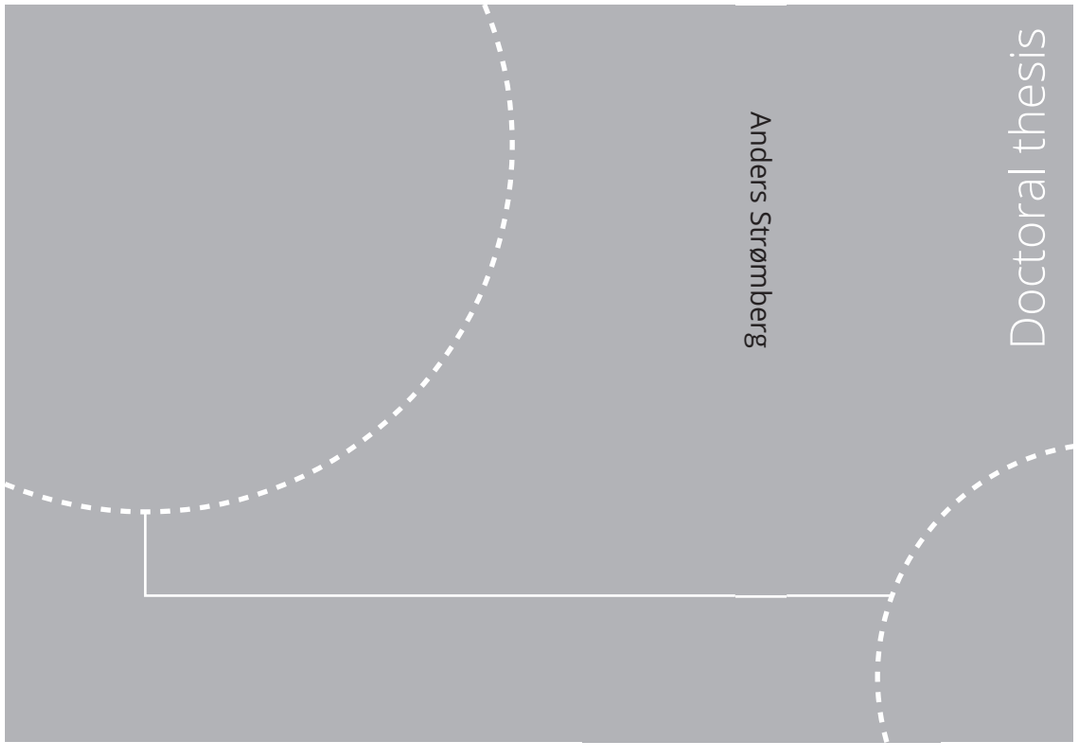


Doctoral theses at NTNU, 2024:236

Anders Strømberg

# Design and control of artificial spin ice

Doctoral theses at NTNU, 2024:236

NTNU

Norwegian University of
Science and Technology

**NTNU**
Norwegian University of
Science and Technology
Thesis for the degree of
Philosophiae Doctor
Faculty of Information Technology
and Electrical Engineering
Department of Electronic Systems

NTNU

Norwegian University of
Science and Technology

Anders Strømberg

# Design and control of artificial spin ice

Thesis for the degree of Philosophiae Doctor

Trondheim, June 2024

Norwegian University of Science and Technology
Faculty of Information Technology
and Electrical Engineering
Department of Electronic Systems

**NTNU**
Norwegian University of Science and Technology

Thesis for the degree of Philosophiae Doctor

Faculty of Information Technology
and Electrical Engineering
Department of Electronic Systems



ISBN 978-82-326-8064-1 (printed ver.)
ISBN 978-82-326-8063-4 (electronic ver.)
ISSN 1503-8181 (printed ver.)
ISSN 2703-8084 (electronic ver.)

Doctoral theses at NTNU, 2024:236



Printed by Skipnes Kommunikasjon AS

Lovingly typeset in LaTeX 2$_\varepsilon$ and the KOMA-Script book-class. Illustrations by the author. Intended for color printing.

# Abstract

Developing sustainable and robust data processing technology is an increasingly important global priority in an energy-scarce world where computational resources limit state-of-the-art applications. Power-hungry generative artificial intelligence systems consume vast amounts of energy and are finding important new use cases along with fast-paced technological progress. One strategy for surpassing the bottlenecks of development is to create new and improved materials with properties that help solve the technological challenges in a more energy-efficient manner. Metamaterials are one group of candidate material systems where an engineered micro- or nanostructure can give rise to tunable material properties beyond those available in common compound materials. These metamaterials can help with the posed challenges by offering computation as a property of the substrate itself; *in-materio* computation. This thesis concerns one specific group of metamaterials: artificial spin ices, which are magnetic systems composed of engineered configurations of nanomagnets. In artificial spin ices, the magnetic dipolar coupling between nanomagnets on a two-dimensional surface is defined by its geometric configurations. Large arrays of these nanomagnets with a vast number of interactions exhibit exotic emergent properties, such as tunable magnetic order and emergent chiralities, and might also exhibit emergent information-processing properties. The thesis aims to offer new methods of understanding, designing, and controlling these systems, and it builds on three papers. The first paper considers how to efficiently model artificial spin ice systems on a large scale, where emergent properties of the materials will manifest. A versatile and efficient simulator is introduced, the foundation of the rest of the work. In the second paper, the transition between two well-known artificial spin ice geometries is introduced, modeled, and investigated experimentally. The magnetization of the nanomagnets in the investigated artificial spin ices order into antiferromagnetic or ferromagnetic order, and we observe regions of metamaterial domains of particular magnetic orders. We find a controllable antiferromagnetic–ferromagnetic order transition by rotating the elements of a square lattice artificial spin

ice. The transition is shown to have specific properties, continuity and coupling-dependence, that require a slight modification of the point-dipole simulator to model reliably. The second paper demonstrates experimentally the predictive power of the simulator. The third paper introduces a new method of controlling artificial spin ice. This method relies on details of the switching mechanism of the nanomagnets, represented by an astroid-like characteristic switching curve. Local control is achieved using globally applied magnetic fields that exploit the inherent dynamics present at domain wall boundaries. This technique represents a new way to interact with artificial spin ice systems that rely on the current microstate of the system and selectively evolves the state only at applied field pulses. The dynamics are governed by each field pulse in the sequence and we call the method *astroid clocking*. Through these three papers, the thesis introduces practical advances in designing and controlling artificial spin ices. These advances are interesting from a fundamental physics perspective and can help discover metamaterial properties useful for energy-efficient and scalable computation.

# Sammendrag

*Dette sammendraget er ikke en oversettelse av Abstract, men et forsøk på å gjøre motivasjonen og hovedfunnene i forskninga tilgjengelig for et bredere publikum.*

Vi lever i en verden der stadig mer energi brukes på elektronisk databehandling. Dette gjør vi fordi vi tror det er nyttig, selv om energien vi bruker er en begrenset ressurs. Noen anvendelsesområder av digital regnekraft kan være ekstremt nyttige, for eksempel i form av kunstig intelligens, men er begrenset av tilgjengelig regnekraft. Hovedmotivasjonen bak denne forskninga er et ønske om å gjøre regnekraften vi bruker mer energieffektiv og mer skalerbar, som vil si kraftigere.

For å jobbe mot dette målet har vi i denne forskninga undersøkt nye, muliggjørende materialer. En stor del av grunnlaget for moderne informasjonsteknologi ligger i gode materialer med passende egenskaper. Materialenes egenskaper, som kan være alt fra kompresjonsstyrke til mer abstrakte egenskaper som signalresponsen i nervevev, bestemmes blant annet av deres sammensetning og atomstruktur. Ved hjelp av nanoteknologi kan vi lage helt nye materialer med helt nye egenskaper. Dette kan vi for eksempel gjøre ved hjelp av konstruerte strukturer som har en størrelse mellom atomenes verden og den makroskopiske verden vi opplever. Slike materialer kalles ofte metamaterialer.

Denne avhandlingen omhandler et spesifikt magnetisk metamateriale som kalles *kunstig spinnis*. Denne typen materiale består av knøttsmå nanomagneter arrangert tett i tett, som vekselvirker gjennom sine magnetfelt. Avhengig av hvordan vi arrangerer de små nanomagnetene får spinnismaterialene forskjellige egenskaper, for eksempel hvordan de reagerer på magnetfelt i ulike retninger. Vi vet at magnetiske materialer i teorien kan behandle informasjon på en svært energieffektiv måte, og trolig på en svært skalerbar måte. Forskninga vi har gjort tar steg mot å anvende denne

teoretiske muligheten gjennom å forstå systemene bedre og å utvikle nye systemer med nye egenskaper.

Den første delen av arbeidet er en modell for effektiv datasimulering av store sammensetninger av nanomagneter. Videre brukes dette simuleringsverktøyet for å finne fram til nye nanomagnetsystemer med spesifikke makromagnetiske egenskaper midt mellom to kjente, motstridende magnetiske egenskaper. Egenskapene til disse systemene verifiseres eksperimentelt. Til slutt bruker vi innsikt fra modellen til å utvikle en ny metode hvor vi på en praktisk måte kontrollerer magnetiseringen i materialene gjennom anvendte ytre magnetfelt. Denne metoden tillater kontroll på et dypere detaljnivå enn tidligere og benytter seg av de iboende egenskapene i materialet.

Avhandlingen bidrar gjennom utvikling av simuleringsverktøy, nye materialsystem og kontrollmetoder til å forstå hvordan vi kan skape og bruke magnetiske materialer med ønskede egenskaper. Det er mye som gjenstår før slike materialer kan anvendes i energieffektiv og skalerbar regnekraft. Arbeidet presentert her bidrar med viktige steg mot praktisk anvendelse av dette fagfeltet.

# Preface

This thesis concludes my years of studies at the Norwegian University of Science and Technology (NTNU). The work is submitted in partial fulfillment of the requirements for the degree of Philosophiae Doctor (PhD) at NTNU.

The work was carried out at the Department of Electronic Systems (IES) with Professor Erik Folven as the main supervisor. Professor Magnus Själander at the Department of Computer Science was the co-supervisor.

Funding was provided by the Norwegian Research Council through the IKTPLUSS project SOCRATES (Grant no. 270961) and by the EU FET-Open RIA project SpinENGINE (Grant No. 861618). All samples were fabricated at the NTNU NanoLab. The Research Council of Norway is acknowledged for the support to the Norwegian Micro- and Nano-Fabrication Facility, NorFab, project number 295864.

## Acknowledgments

I am grateful for the opportunity to complete a PhD at NTNU. It has taken its time, with a leave of absence to teach, a pandemic, parental leave, and quite a bit of struggle. A lot can happen during the work with a PhD degree, and I have learned a tremendous amount during these past years. Sadly, I have not learned how to do a backflip.

Finally, I submit my thesis and close this chapter. There are many I would like to thank.

First and foremost, thank you to my supervisor, Professor Erik Folven. You are the reason I started this PhD, and you are the reason I finished it. Your blend of intelligence, practical knowledge, hands-on teaching, and good-hearted nature make you the complete package. Thank you for all the engaging discussions, lunch and coffee talks, travels, and friendly competitions over the years. You are a great role model; I am proud to call you a friend.

Thank you to my other academic role models. To Professor Magnus Själander, my co-supervisor, it was always inspiring to discuss my PhD

progress with you. Thank you for providing a second and honest opinion. To Professor Gunnar Tufte, thank you for inspiring insights and theories on an entirely new (to me) and exciting field: computer science. A big thank you to Professor Emeritus Jostein Grepstad for your support and insights, scientifically, academically, and grammatically. I would not be where I am without you.

Thank you to the staff and engineers at NTNU NanoLab. I started my first part-time job with you during my first year as a student. I did not know I would stick around for this long, but I have thoroughly enjoyed working with you, a world-class cleanroom staff.

Thank you to Astrid Aksnes and Thomas Tybell, who are great role models as leaders of my academic unit and department, respectively. I have always felt that you looked after me and supported my cause in work-related issues. Thank you.

To all my former and current office mates: Sam, Fredrik, Ambjørn, Einar, Jakob, Ida, Dheerendra, and Mukesh. Thanks for all the fun talks, and sorry for disturbing you so much. A special thanks to Einar, in particular, for showing me all the ropes of the lab as a fresh student and being a role model in my life as a PhD candidate. Thank you to everyone who has contributed to the social environment at the department; Silje, Gara, Jens, Jens, Amund, Amund, Michael, David, Roger, Veslemøy, Vitor, Ashkan, Bettina, Farrokh, Florian, Julia, Brage, Fredrik, Kristina, Lukas, and probably too many that my tired brain can't think of. To everyone in the Oxide Electronics Group; Kristoffer, Roman, and all my office mates again. A special thanks to Torstein, who trusted me to teach. Thank you to all the master students, Thorstein, Amanda, Yannis, Håvard F., Rune, Marte, Susanne, Svein, Gunvor, Jonas, Håvard Å., and Ida. I hope you learned as much from me as I did from you.

A big thank you to the COMET group for an exciting and invaluable collaboration. To 'gutta på gølvet' over at IDI Odd Rune, Johannes, and Arthur. You have taught me much, and I look forward to our future partnership.

Thank you to my family for always supporting me. To my parents, Asbjørn and Maibritt, for letting me find my own ways and for letting me come home to unwind during holidays. To my sister, Anne Line, for showing me the value of finishing my homework in a timely manner.

To my daughter, Solveig, if you ever read this, thank you for all your excited screams and smiles at the end of a long day. You bring me so much joy, and I will always be proud of you. Our time together during my parental

leave was the best part of this whole time working as a PhD candidate. Thank you for providing perspective and motivation to finish this work.

Finally, my sincerest and most heartfelt thanks to my partner, Ragnhild. It is hard to overstate how much your support has meant to me over these past years. I am so lucky to have you in my life. Thank you.

# List of papers

The following is a list of publications that are included in this thesis:

**I** **flatspin: A large-scale artificial spin ice simulator**
*Physical Review B*, vol. 106, no. 6, art. no. 064408, Aug. 2022.
DOI: 10.1103/PhysRevB.106.064408
J. H. Jensen, A. Strømberg, O. R. Lykkebø, A. Penty, J. Leliaert, M. Själander, E. Folven, and G. Tufte

Jensen and Strømberg are shared first authors and contributed equally to this work. Jensen and Lykkebø did the principal engineering work on the simulator, with important contributions from Strømberg and Penty. Strømberg conceived and engineered the thermal model with input from all authors. The main authors of the paper were Jensen, Strømberg, Lykkebø and Penty. Själander, Folven and Tufte contributed with text and corrections. All authors contributed with ideas and discussions, both regarding the design of the simulator itself and its verification.



**II** **On the Antiferromagnetic-Ferromagnetic Phase Transition in Pinwheel Artificial Spin Ice**
*In review*
DOI: 10.48550/arXiv.2404.03973
A. Strømberg, E. Digernes, R. V. Chopdekar, J. Grepstad, and E. Folven

Strømberg conceptualized and designed the study. Strømberg fabri-

cated the samples, led the XMCD-PEEM experiments and Digernes and Folven contributed to these measurements. Strømberg analyzed the results. Chopdekar provided support during XMCD-PEEM measurements. Strømberg wrote the manuscript, Grepstad and Folven provided feedback, with input from all authors.



**III Clocked dynamics in artificial spin ice**

*Nature Communications*, vol. 15, art. no. 964, Feb. 2024.
DOI: 10.1038/s41467-024-45319-7
J. H. Jensen, A. Strømberg, I. Breivik, A. Penty, M. A. Niño, M. W. Khaliq, M. Foerster, G. Tufte, and E. Folven

Jensen and Strømberg conceived and designed the study and contributed equally to this work. Jensen did the initial discovery in simulations and did the simulation study. Strømberg fabricated the samples. Strømberg led the XMCD-PEEM experiments and Jensen, Breivik, Penty, Tufte, and Folven contributed to these measurements. Foerster, Niño, and Khaliq provided support during XMCD-PEEM measurements and PEEM vector magnet operation. Strømberg and Jensen performed the analysis with assistance from Breivik and Penty. Folven and Tufte oversaw the project and provided feedback and direction throughout. Jensen and Strømberg wrote the manuscript with input from all authors.

## Other publications

As a part of their work the candidate has contributed to other publications which are not part of this thesis.

**i Direct imaging of long-range ferromagnetic and antiferromagnetic order in a dipolar metamaterial**
*Physical Review Research*, vol. 2, no. 1, art. no. 013222, Feb. 2020.
DOI: 10.1103/PhysRevResearch.2.013222
Einar Digernes, Sam D. Slöetjes, Anders Strømberg, Ambjørn D. Bang, Fredrik K. Olsen, Elke Arenholz, Rajesh V. Chopdekar, Jostein K. Grepstad, Erik Folven

**ii Sustainability in project-based learning: Project themes and self-perceived competencies**
*Nordic Journal of STEM Education*, vol. 5, no. 1, MNT-konferansen 2021, Feb. 2021.
DOI: 10.5324/njsteme.v5i1.3925
Torstein Bolstad, Lars Lundheim, Anders Strømberg, Milica Orlandic, Pauline Hardeberg Zimmermann

**iii Anisotropy and domain formation in a dipolar magnetic metamaterial**
*Applied Physics Letters*, vol. 118, no. 20, art. no. 202404, May 2021.
DOI: 10.1063/5.0045450
Einar Digernes, Anders Strømberg, Carlos A.F. Vaz, Armin Kleibert, Jostein K. Grepstad, Erik Folven

**iv Effects of array shape and disk ellipticity in dipolar-coupled magnetic metamaterials**
*Physical Review B*, vol. 104, no. 13, art. no. 134421, Oct. 2021.
DOI: 10.1103/PhysRevB.104.134421
Sam D. Slöetjes, Einar S. Digernes, Anders Strømberg, Fredrik K. Olsen, Ambjørn D. Bang, Rajesh V. Chopdekar, Erik Folven, Jostein K. Grepstad

v **Do Students Reflect on Sustainability? Student Development of Competencies for Sustainability in Project-Based Learning**
*Nordic Journal of STEM Education*, vol. 7, no. 1, pp. 73-83, May 2023.
DOI: 10.5324/njsteme.v5i1.3925
Torstein Bolstad, Lars Lundheim, Anders Strømberg, Milica Orlandic, Pauline Hardeberg Zimmermann

vi **Design thinking and shared ignorance as a framework for student-faculty partnerships: A case study of the creation of teaching activities for wicked problems**
*International Journal for Students as Partners*, vol 8., no 1., May 2024.
DOI: 10.15173/ijsap.v8i1.5614
Torstein Bolstad, Anders Strømberg, Sven Amberg, and Ida Bjørnevik

For an updated list, including contributed talks, the reader is referred to the Current Research Information System in Norway (CRISTIN, person #717966).

# Contents

# 1 Introduction

> We are living in a material world.
>
> Madonna

A material can be a single pure substance, a complex mixture of substances, or a macroscopic composite of other materials, described by its properties, structure, the way it is made, or simply by its use[1]. Historical periods are named after essential materials of their time, a witness to materials' defining societal, technological, and cultural significance. However, the available selection of materials is defined by the materials of the natural world or man-made composites of such materials. Technological progress is coupled with an insatiable appetite for better and more sustainable materials for a better world. Nanofabrication advances answer this call by introducing novel material applications and a new distinct class of materials: *metamaterials*.

Metamaterials are materials with properties that go beyond what can be obtained with conventional composite materials. These new or extended properties are obtained by constructing materials of repeated microscopic or nanoscopic elements, *metaparticles*, with a range of interactions[2]. Similar to conventional composite materials, metamaterials are manufactured. In contrast to conventional composites, metamaterials derive their unique properties not from the mixture of chemically distinct components but from their structure, metaparticles, and local interactions. While conventional composites like the straw-reinforced clay brick have existed for millennia, composite metamaterials are a recent addition[3].

The first examples of metamaterials were created in the second half of the 1940s as materials with new properties for radio frequency waves by W. E. Kock [4–6]. The metaparticles of Kock's radio frequency metamaterials

were rather large metallic elements on the centimeter scale, suitable only for radiation with wavelengths larger than, or comparable to, these metallic elements. With the advent of nanotechnology, it has become feasible to create metamaterials with applications relevant to much more than radio waves, such as optical properties requiring features well below 1 µm[7, 8].

Technological advancements provide the metamaterial toolbox of tuning, extending and combining materials, creating a vast space of possible properties — and the list of sought after properties is long. Examples include mechanical, chemical, optical, and electrical properties, such as the compressive strength of concrete, the chemical inertness of glass, the refractive index of a polymer coating, and the tunable conductivity of a semiconductor. There are also more specialized and complex properties, such as the signal response of neural tissue, which is highly dependent on the networked structure within the material. Improved technological capabilities broaden available characteristics of engineered materials and allow a high degree of material control. This control extends to the class of magnetic properties, an integral part of current and developing technological use.

Magnetic properties in materials are critical for various applications, from data storage and magnetic sensors to energy generation and medical imaging. The use of, not to mention the fascination with, magnets is ancient. One example is their use in navigation as compass needles. The origin of the term *magnet* itself was first described by the natural philosopher Pliny the Elder (23–79 CE) in his *Historia Naturalis*[9]. While he perished in the Mount Vesuvius eruption of 79 CE, along with thousands of scrolls of ancient texts such as the Herculaneum scroll, magnets and magnetic materials continued to develop and be used. In October 2023, magnets were vital to reviving the first text passages of the Herculaneum scroll using the Diamond Light Source synchrotron[10], although there is little hope for Pliny himself.

In summary, materials define the world. With nanotechnology, we can more fully define their properties, including the magnetic properties. Magnetic materials are marvels of the past, present, and future. The following sections will provide a more detailed historical and technological context for using magnetic materials and explore the primary motivation for this work: scalable, energy-efficient computing using nanomagnets.

## 1.1 Historical and technological context

The foundational understanding of magnetism in the context of modern technology began with Ørsted's discovery in the early 1800s, linking electricity and magnetism[11]. Maxwell's formulation of electromagnetic theory further established a theoretical description of electromagnetic fields and their interactions with matter[12]. Maxwell's equations created a framework for technological applications such as wireless telegraphy, radio, and a vast number of electromagnetic devices. In the early 1900s, Pierre Weiss established a microscopic origin of magnetism and introduced the concept of magnetic domains, clarifying how materials exhibit magnetism at the macroscopic level[13]. Developing a theoretical understanding of magnets provided the foundation for the modern use of magnetic material properties.

Magnetic domains of ferromagnetic materials were used as recording and data storage media soon after their discovery[14]. During the 20th century, magnetic materials developed and became widespread, from ferrite magnets used in magnetic core memory to floppy disks and hard disk drives. At the end of the 20th century, giant magnetoresistance (GMR) was simultaneously discovered by two independent research groups led by Albert Fert and Peter Grünberg[15, 16], which dramatically increased the data storage density as read heads switched from inductive to much more sensitive resistive readout.

The discovery of GMR significantly enhanced magnetic storage media by utilizing the electron's spin, a quantum mechanical property of the electron, marking the beginning of the *spintronics* era. In spintronics, the electron spin, not just their electric charge, is exploited for information processing and storage.

Following the discovery of GMR, several important discoveries directly impacted storage media, sensors, and computer technology. The discovery of tunnel magnetoresistance (TMR)[17] in magnetic tunnel junctions (MTJs), and spin transfer torque (STT)[18] led to the development of magnetoresistive random-access memory (MRAM)[19] and the conceptualization of STT-MRAM[20]. The latter has the potential to dramatically impact how we use the modern computer by providing a competitive universal memory technology that combines permanent and fast storage. In the early 2000s,

there were several milestones in spintronics, such as the discovery of the spin Hall effect[21], topological insulators[22], and the quantum spin Hall effect[23].

The field of spintronics utilizes many magnetic materials with different magnetic orders. Electronic switching of an antiferromagnet was established within the last decade, and paves the way for technology that can offer faster and more energy-efficient magnetic switching[24]. This energy efficiency might be further enhanced by eliminating electron transport through devices based on the waves of the electron spins, with the field of magnonics emerging[25]. Another avenue for energy efficiency is emerging spintronic devices. These devices are based on novel material structures, such as two-dimensional magnetic crystals[26] or the quantum anomalous Hall effect enabling the switching of magnets with tiny currents[27]. Advances in material quality and material engineering facilitated these developments. Recently, a new phase of magnetic order has gathered attention, termed altermagnetism[28, 29]. A brand new phase of magnetic order is a prominent example of magnetic material properties as a relevant research avenue.

What material properties are relevant, and what materials are technologically available? While most of the novel magnetic materials with exotic spintronic properties are chemically or physically synthesized, they are governed by the stable states of the arrangements of atomic matter. With nanofabrication and the concept of metamaterials, a top-down approach is feasible, introducing many degrees of freedom in designing materials and their resulting properties.

Magnetic metamaterial tuning involves structurally manipulating these at the nanoscale to tailor their magnetic properties for specific applications. This tuning can lead to materials with customizable magnetization dynamics, enhanced magnetic field sensitivity, or novel quantum effects, offering a pathway to overcoming the limitations of conventional magnetic materials.

One example of such magnetic metamaterial systems is artificial spin ices (ASIs), first introduced by Wang et al.[30]. Nanofabrication techniques, notably electron beam lithography, enable the fabrication of large arrays of single-domain nanomagnets that interact through their dipolar fields. These systems exhibit a plethora of emergent behavior and have attracted considerable research interest[31, 32]. They come in a large variety of config-

urations, typically in some variation of two-dimensional tiling. Applications range from model systems of statistical thermodynamics to next-generation computing devices. Their shared features are metaparticles of well-defined magnetization arranged in an extended geometric configuration, well in line with the definition of a metamaterial (barring the typical two-dimensionality of ASIs).

With ASIs, it is possible to engineer specific material properties. These properties are not limited to the materials' magnetic properties, but can be more abstract and complex. One important example is the artificial spin ice (ASI) response to some signal, analogous to the signal response of neural tissue mentioned earlier. The possibility to design material properties makes ASIs relevant for several applications in computing devices, such as computation *in-materio*[33]. Recently, researchers have performed experiments where ASIs are used in the first step towards neuromorphic computation with nanomagnets[34, 35]

## 1.2 Motivation for the thesis

> Your scientists were so preoccupied with whether or not they could, they didn't stop to think if they should.
>
> Dr. Ian Malcolm, Jurassic Park

### 1.2.1 Energy efficient compuation

The information and communication technology (ICT) sector is a significant consumer of global electricity, a scarce resource that is still directly linked to $CO_2$ emissions. In 2022, data centers and telecommunication networks alone accounted for between 2.8% to 3.8% of all electric energy use in the EU[36]. The ICT sector is growing rapidly; from 2010 to 2018, the global installed storage capacity increased by a factor of 26 and data center internet traffic by a factor of 11[37]. Current generative artificial intelligence (AI) models are particularly power-hungry, and generating a single artificial image can consume as much energy as a full battery charge of a typical smartphone[38]. With the exponential growth of data production fueled by advancements in AI, internet of things (IoT), and cloud services, this computation consumption is expected to increase, posing immense challenges in sustainability and energy efficiency. Fortunately, the significant increases in scale have up until now been offset by considerable energy efficiency increases. However, continued focus on research and innovation is required to keep pace with the rapidly growing consumption of ICT services.

The pursuit of energy-efficient computation naturally poses the question of fundamental limits of information processing. In his foundational work, Rolf Landauer proposes a theoretical thermodynamic minimum amount of energy required to erase one bit of information, the so-called Landauer limit [39]. The Landauer limit establishes a boundary on the minimum energy cost for the irreversible manipulation of information, due to a corresponding and unavoidable increase in entropy[40]. This limit has since been established experimentally and is not a completely esoteric concept[41]. Landauer's

insight reveals that computing will never be entirely energy-free, but there is significant room to improve the energy efficiency of current technologies. Standard electronics see substantial energy dissipation through resistive loss due to the need for electron transport.

Devices based on magnetic material systems offer pathways to increase energy efficiency in computation. Unlike traditional electronic devices that rely on charge-based information transfer by electron transport, magnetic systems can leverage spin-based information processing. Nanomagnetic systems can operate with substantially lower energy dissipation, shown to approach the Landauer limit in simulations of nanomagnetic logic[42]. Research into novel magnetic materials and new computation paradigms using nanomagnetic systems are critical research areas for a sustainable ICT sector.

### 1.2.2 Scalable neuromorphic computation

The exponentially growing consumption of computation requires vast amounts of energy but is ultimately driven by important societal and technological needs. One recent example is the vast amounts of computer power required to train large language models (LLMs) for artificial intelligence (AI). Such models are trained using a staggering number of floating-point operations (FLOPs), such as GPT-4, which used $2.1 \times 10^{25}$ FLOPs, or 21 billion petaFLOP, using the method of reinforcement learning on large data sets[43]. Google Deepmind's Gemini Ultra model, trained in the same manner, is nearing 80 billion petaFLOP and rapidly approaching the disclosure limit of the recent U.S. Executive Order of 100 billion petaFLOP[43, 44]. Currently, consumption of FLOPs for training AI increases at 0.6 orders of magnitude each year[44].

It might be possible to decrease the computation required for AI performance by algorithmic improvements rather than scaling. Such algorithmic improvements could be explicitly engineering in human insights instead of relying on shear brute-force computation by reinforcement learning. However, as the father of reinforcement learning, Richard Sutton, puts forth in his argument on the "Bitter Lesson", this strategy historically and ultimately falls short of upscaling computation[45]. The critical insight of the Bitter Lesson suggests

that general methods leveraging computation, such as search and learn, are ultimately more effective than approaches relying on humanly designed features or conceptions of knowledge. Thus, the scalability of computation presents another significant global challenge.

Magnetic computation, e.g., computation with ASI systems, presents an innovative approach to scaling computation beyond Moore's law. By leveraging the magnetic properties of materials for computation *in materio*, magnetic systems potentially offer a scalable alternative that surpasses traditional electronic constraints[46]. Traditional computers rely on myriads of transistors in simple logic gates that build an ever-expanding hierarchical tower of abstractions. However, other computation paradigms exist, and we already know of some, such as the computation offered by neural tissue in the brain. These new computational models rely on entirely different architectures of computation; one example is commonly referred to as neuromorphic computing.

Neuromorphic computing is computing based on a network of computational parts and nodes. The network structure, reminiscent of the architectural model of the human brain, enables more efficient processing of complex data patterns and adaptive learning capabilities. Unlike traditional computing architectures that separate memory and processing units, neuromorphic systems integrate these functions in a network of artificial neurons and connections. While many current instances of neuromorphic computing use virtual nodes and simulated connections, material neuromorphic computation can be realized in custom hardware and is a developing area of research[47].

In conventional CMOS technology there are also promising computational models for scalable computation that involve specialized hardware. While the increase in base clock frequency of commercial processors stalled more than a decade ago, manufacturers have pivoted to provide multi-core processors or specialized GPU hardware to keep up with the development[48]. GPU price-performance improvements hint at how successful this approach has been, as the cost of computation capacity (measured in FLOPs per second per dollar) halves roughly every 2.5 years[49]. This immense success of GPUs is evidence that specialized hardware is a viable strategy. Computation using magnetic materials, e.g., neuromorphic computation, can be a potential avenue for future specialized hardware[46].

In summary, the research of this research is driven by the urgent need for more energy-efficient electronics, sensors, and computers to address the environmental impact of our growing digital footprint. Moreover, it is inspired by the potential of ASI systems to usher in a new computation paradigm. This paradigm could significantly reduce energy consumption and enhance scalability, thus contributing to the development of sustainable AI. This effort towards more sustainable computing practices embodies both a technical challenge and a moral imperative. We must consider the broader implications and costs of the capabilities we unlock through technological innovation in the big picture.

The research is inspired by the possibility of mitigating the energy consumption of computation and the scalability issues current applications face. We believe this can be done by exploiting ASI systems and their unique advantages, which combine the energy-efficient information processing of magnetic systems, the available tunability of the emergent properties, and the access to directly observe and understand their behavior. However, there is a long way to go, but it will be necessary to start with mastering the design and control of the material systems. The following section presents the direct goals of the thesis.

## 1.3 Aim of thesis

The main goal of this thesis is to expand the framework for designing, controlling, and analyzing metamaterial systems of ASI. In order to achieve this, the work presented herein involves extensive modeling and experimental work.

The overall goal can be divided into the following specific goals:

1. Model the physics of ASI systems practically and efficiently to manifest large-scale material properties.

2. Develop and optimize the design process for fabricating ASI systems of any configuration.

3. Control the state and dynamics of ASIs.

4. Develop tools to analyze ASI states and responses to stimuli.

Together, these goals expand the foundation for ASI systems as a theoretical and experimental testbed for new and useful magnetic materials. With the tools and methods presented herein, ASI systems demonstrate new metamaterial properties and provide information processing substrates for next-generation computation.

# 2 Nanomagnetic systems

## 2.1 Magnetism

To understand the modeling of nanomagnetic systems, it is helpful first to understand what a nanomagnetic system is or even what a magnet is. In the colloquial sense, magnets are objects of a magnetic material, typically ferromagnetic, that exhibit a spontaneous net magnetization. In other words, magnets are objects with an internal quantity of magnetic moment that does not cancel out, and thus also with an extended magnetic field outside it, the so-called magnetic stray field[9, 50]. For the layman, the stray field that interacts with other materials is a magnet's quintessential and nearly magical property. The stray field of a magnet can induce a magnetization in another object, which in turn can favor energy-minimizing attraction between the two. Magnetization and stray fields are fundamental concepts that underlie the work of this thesis. However, the atomic origin of magnetism will not be necessary for the discussion in this thesis, and the reader is referred to the excellent work of Stöhr and Siegmann for more information[9].

Magnetization is a measure of the density of magnetic moments. Magnetic moments, or magnetic dipole moments, are vector quantities (noted $\mathbf{m}$) that we define here as the source of a magnetic field, the vector representing the moment strength and direction. By the superposition principle, magnetic moments accumulate or cancel out, and magnetization typically refers to the net magnetic moment of an object divided by its volume to provide a measure of magnetic moment density. It is useful to describe magnetization as a vector field, $\mathbf{M}$, a field which is zero at any point $\mathbf{r} = (x, y, z), \in \mathbb{R}^3$ outside a magnetic material and non-zero inside:

$$\mathbf{M}(\mathbf{r}) = M_x(\mathbf{r})\,\hat{\mathbf{i}} + M_y(\mathbf{r})\,\hat{\mathbf{j}} + M_z(\mathbf{r})\,\hat{\mathbf{k}}, \tag{2.1}$$

where $M_x(\mathbf{r})$, $M_y(\mathbf{r})$, and $M_z(\mathbf{r})$ are the components of the magnetization vector in the $x$, $y$, and $z$ directions, respectively, each as a function of $\mathbf{r}$.

The magnetic field, or magnetic flux density (noted $\mathbf{B}$), is a slightly more nuanced physical quantity. It can be defined by the Lorentz force it exerts on charged particles or simply by the magnetic torque $\tau$,

$$\tau = \mathbf{m} \times \mathbf{B}, \tag{2.2}$$

that a single magnetic moment $\mathbf{m}$ experiences in its presence. The magnetic flux density $\mathbf{B}$ encompasses both an applied magnetic field and the magnetization response of a material subjected to $\mathbf{B}$. However, it is useful to distinguish these effects, and an auxiliary field $\mathbf{H}$ is defined such that

$$\mathbf{B} = \mu_0(\mathbf{M} + \mathbf{H}), \tag{2.3}$$

where $\mu_0$ is the vacuum permeability. $\mathbf{H}$ is also known as the magnetic field strength, and outside a magnetic material, i.e., where $\mathbf{M} = \mathbf{0}$, it is proportional to $\mathbf{B}$. In this thesis, it will be most relevant to refer to the magnetic field outside of magnetic materials, and the term *stray field* (occasionally dipolar field or demagnetization field) will be used to refer to the $\mathbf{H}$-field originating from a magnet. For practical reasons, values for the $\mathbf{H}$-field magnitude will be given in units of tesla (T, or often mT), technically designating the quantity $\mu_0 H$ where $H$ is the magnitude of $\mathbf{H}$.

The most relevant aspects of magnetism necessary to understand this thesis are the magnetization of magnetic materials, or magnets, and the magnetic stray field they emit. However, magnets come in all shapes and sizes, which affects their magnetic properties and introduces new important aspects such as anisotropies and switching.

## 2.2 Origin of nanomagnetism and 2D nanomagnets

While the magnetization of a macroscopic magnet often can be described as an average magnetization or a single total magnetic moment, this is a gross simplification. In the early 20th century, Pierre Weiss introduced the concept of ferromagnetic domains[13]. A macroscopic magnet is not

magnetically homogeneous, but rather a collection of microscopic regions with uniform magnetization along different directions, known as domains. The magnetization of these domains collectively sum to the magnetization of the magnet. The domains are separated by domain walls, and the exact configuration is a delicate balance of domain walls and domains with their resultant stray fields.

The minimization of the total free energy of the magnet determines the domain structure. For simplicity and relevance to the material system of this thesis, we consider a magnet without material magnetocrystalline anisotropy, and in the absence of an applied field for now. We also ignore contributions like stress and magnetostriction. Two energy contributions remain, and they dominate the magnetic microscopic structure: the energy associated with the stray field and the energy associated with the so-called exchange interactions[51].

The energy cost of the stray field is due to its self-interaction with the magnet, which favors demagnetization. The stray field is, therefore, often called the demagnetizing field (and then refers to the field inside the magnet as well), and the energy is expressed as

$$E_{\text{demag}} = -\frac{1}{2}\mu_0 \int_{\text{magnet}} \mathbf{M} \cdot \mathbf{H}_{\text{demag}} \mathrm{d}V. \tag{2.4}$$

The stray field and thus, $E_{\text{demag}}$, can be minimized by arranging the magnetization of domains to establish magnetic flux closure inside the magnet[52]. Reduction of magnetization by field minimization leads to preferred magnetization directions for magnets of different shapes and sizes, known as shape anisotropy. The magnetization of otherwise magnetically isotropic thin films lie in an in-plane direction due to this shape anisotropy, and this is also why magnetic compass needles have a well-defined magnetization that lies along their long axis.

Exchange interactions put a bound on the intricacy of the magnetic domains that a magnet can exhibit. While the origin of these interactions is quantum mechanical and relates to the atomic origin of magnetism, it can be understood as the energy cost of neighboring misaligned magnetic moments inside the magnet. Inside a magnetic domain, the exchange energy is minimized as all moments align favorably, while the exchange interaction is significant

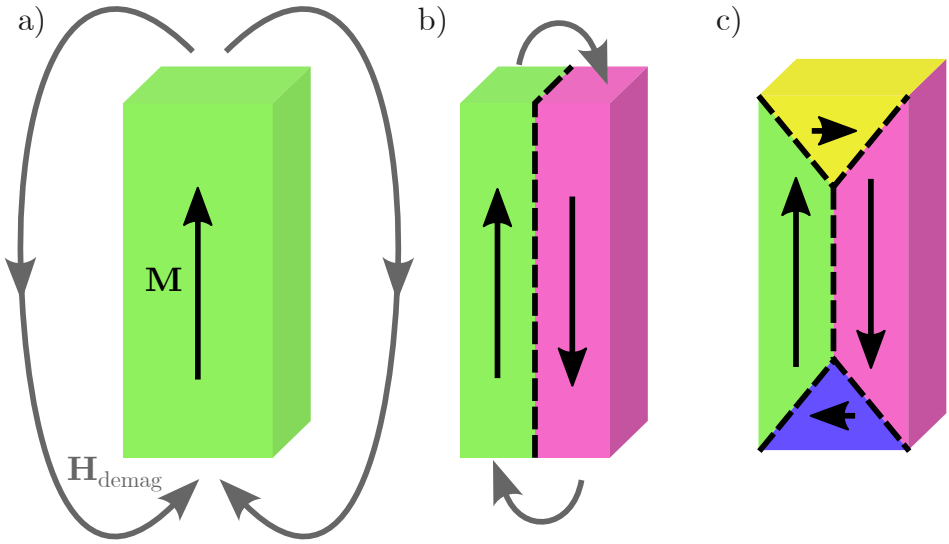


**Figure 2.1:** Schematic of domain creation by minimization of the stray field. a) A single-domain magnet with a significant demagnetizing field $\mathbf{H}_{\text{demag}}$. b) By introducing a single domain wall (dashed line) and a new domain of opposite magnetization, the demagnetizing field is significantly reduced. c) By introducing more domain walls, complete magnetic flux closure can occur within the magnet, and the demagnetizing field is eliminated at the cost of creating domain walls.

across a domain wall where the magnetization changes abruptly. Therefore, the exchange interaction favors minimizing domain walls in a magnet.

Minimization of the stray field by demagnetization and minimization of domain walls are competing effects, illustrated in Figure 2.1. In the single-domain case, the entire magnetization of the magnet contributes to the stray field, which is maximized, but there are no domain walls, so exchange energy is minimized. As domain walls are introduced, the demagnetization energy is decreased, at the cost of exchange energy. This simple picture portrays the competing effects that balance the domain wall formation and the stray field.

It is worth noting that the demagnetization energy is a function of the total volume of the magnet. In contrast, the exchange energy associated with

domain walls is a function of the cross-section. For a magnet of a particular characteristic size $d$, the demagnetization energy contribution grows with the volume ($\propto d^3$), while the domain wall contribution grows with the cross-section ($\propto d^2$). In the limit of very large magnets, we expect to find a magnet with many domains and domain walls but a fully canceled-out magnetization and no demagnetization field. However, in the limit of very small magnets, we expect the energy cost of even a single domain wall to surpass the energy of a completely uniform magnetization: a single-domain particle.

The single-domain magnet is typically observed for submicron particles, i.e., magnetic nanoparticles or nanomagnets[53, 54]. They are the fundamental building blocks of nanomagnetic systems, and the motivation for their size mirrors the classic motivation for nanoparticles, where bulk and surface effects switch dominance. The exact size threshold for single-domain nanomagnets depends on the exact shape and material properties. Due to the shape anisotropy, elongated nanomagnets are more likely single-domain, even at larger dimensions. For elongated magnets, the shape anisotropy also ensures that the magnetization favors alignment along the long axis, establishing two stable magnetization configurations: a bistable nanomagnet[55].

It is worth noting that single-domain particles also exist in the reduced two-dimensional system, e.g., in a patterned magnetic thin film. Domain walls in a thin film are functionally one-dimensional, and the domains that produce the demagnetization field are two-dimensional. The topology restricts the creation and movement of domain walls, affecting nanomagnet behavior such as magnetization reversal.

While a single-domain nanomagnet, by definition, does not have domain walls that can move, the magnetization can change in response to stimuli such as an external field or temperature. Circular and rounded, near-circular nanomagnets do not have significant barriers between stable magnetization configurations, and the magnetization coherently rotates in response to the applied field[56]. Bistable nanomagnets, on the other hand, have a high shape anisotropy-induced energy cost for the magnetization state perpendicular to the long axis, which would occur for coherent magnetization switching. Other switching mechanisms, such as domain wall nucleation and propagation, can occur as the cost of a domain wall across the short dimension is lower

than across the long dimension[54]. Switching is also influenced by other factors such as the edge roughness of the magnet[57].

Switching in single-domain nanomagnets has been well-described mathematically, notably by Stoner and Wohlfarth[58]. They formulate the energy $E$ of an ellipsoidal particle of volume $V$ and saturation magnetization $M_S$ as the sum of two terms,

$$E = KV \sin^2 \theta - M_S V H \cos(\phi - \theta), \tag{2.5}$$

where $\theta$ is the angle of the magnetization direction and $\phi$ is the angle of the applied field, both with respect to the long-axis. $H$ denotes the applied field strength. The first term describes the anisotropy energy and the cost associated with off-axis magnetization, and the second term is the energy due to the applied field, the Zeeman energy[9]. The stable magnetization direction for any given field minimizes the total energy of Equation (2.5). An elongated nanoparticle with a magnetization along one direction of the long axis can be described as a stable point in an energy landscape. There is also a stable point at the opposite magnetization direction, separated by an energy barrier, see Figure 2.2a. If an external field is applied, the energy landscape changes as described by Equation (2.5), and the magnetization will favor alignment with the field. When the applied field becomes strong enough, a jump in the magnetization occurs. This hysteresis behavior of the magnetization of a nanoparticle as a function of the applied field in the Stoner-Wohlfarth model is plotted for two applied field angles in Figure 2.2d.

For any applied field direction, there is a corresponding field strength that is strong enough to switch the magnetization, unless the magnetization is already aligned in the energy-minimizing direction. This field is referred to as the critical switching field. The strength of the critical switching field for any direction can be plotted as a curve of field strengths in terms of the parallel and perpendicular field components, see Figure 2.2f. The result is an astroid curve and is called the Stoner-Wohlfarth astroid[58, 59].

One nanomagnet alon and and its states, field, and switching criteria do not give rise to interesting dynamics and ambitious, far-reaching applications. We need many of them for that. *Nanomagnetic systems* are more extensive collections of nanomagnets. Nanomagnets can be colloidal magnetic particles

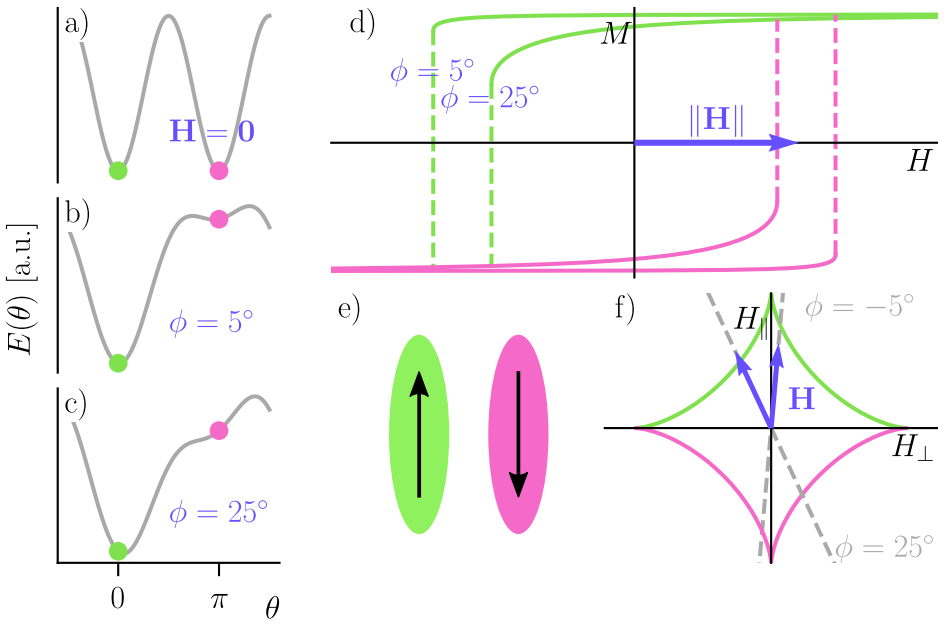


**Figure 2.2:** The Stoner-Wohlfarth model of stable magnetization states for a single-domain particle. a-c) The energy landscape for a single-domain particle as a function of magnetization direction $\theta$ for: a) no applied field, b) a field applied at $\phi = 5°$, and c) the same field strength applied at $\phi = 25°$. d) Hysteresis curves for the two applied field directions, $\phi = 5°$ and $\phi = 25°$, indicating the field-parallel component of the stable magnetization $M$ for a given field strength $H$. Dashed lines indicate a magnetization switch between the up state ($\theta = 0°$, green curve) and the down state ($\theta = \pi$, pink curve). The applied field strength $\|\mathbf{H}\|$ is large enough to switch the magnetization down-to-up if applied at $\phi = 25°$ but not at $\phi = 5°$. e) Schematic of the two stable magnetization states at no applied field. f) The resulting Stoner-Wohlfarth astroid, depicting critical values of the parallel and perpendicular field components, $H_\parallel$ and $H_\perp$, and the two applied fields. An applied field will switch a magnet to the green (pink) state if the vector crosses the green (pink) curve.

that aggregate into micro- or macroscopic structures or simply arranged on a surface as a patterned magnetic thin film. One example of a nanomagnetic system is a collection of two-dimensional particles that interact through their stray fields, such as that of ordered thin film nanomagnets found in artificial spin ice (ASI).

## 2.3 Artificial spin ice

Artificial spin ices are engineered nanomagnetic systems, originally designed to mimic the frustration and degeneracy found in pyrochlore spin ice materials[60–62]. The concept of spin ice materials originates from the study of rare earth titanates[63], and are characterized by so-called frustrated magnetic order. The work with pyrochlore spin ices laid the theoretical groundwork for *artificial* spin ices, which are engineered magnetic systems that deliberately exhibit magnetic frustration by their geometric design. The etymological origin thus derives from the fact that the nanomagnets are not true electron spins but artificial spins (macrospins). Further, the ice nomenclature is inherited from the pyrochlores, whose spin structure resembles the hydrogen orientation in water ice. In the original conception of ASI, artificial spin ice, pyrochlore spin ice, and water ice all obey the so-called ice rules, i.e., vertices of two-in-two-out[64–66]. Several so-called ASI configurations stray significantly from their namesake through the analogy to the water ice structure and could be better termed artificial spin systems[32]. This thesis will use the acronym ASI to describe all ASI derivatives, ice-like or not, for obvious reasons.

Despite the esoteric name ASIs offer a macroscopic scale that allows for practical, direct observation and manipulation of magnetic moments in a nanomagnetic system[67–70]. This practical accessibility makes ASIs relevant as analog model systems for studying magnetic frustration and statistical mechanics[71]. Furthermore, researchers have developed and used ASI systems for a range of other applications, for example as a metamaterial with emergent physical phenomena[72] or as reconfigurable magnonic crystals[73].

There have been many experiments studying ASI and their behavior. The

first physical realization of ASI, lithographically patterned nanomagnet arrays, was designed to topologically mimic the frustration found in pyrochlore spin ice[30]. This first example demonstrated the prototypical square ASI, and focused on studying frustrated magnetism that was directly observable on a macroscopic scale. Various lattice geometries were soon explored in order to study their impact on the magnetic behavior. Examples include the honeycomb lattice ASI, or Kagome ASI, which revealed monopole dynamics, i.e., magnetically charged vertices and how they interact on the lattice[67]. Many experiments were made viable through magnetic force microscopy, which can be used to directly observe the microstates of ASI structures at a single-spin resolution[68, 74]. Emergent phenomena, like the formation of magnetic charge crystallites, i.e., metamaterial domains, were observed directly and highlights the potential for using ASI as a metamaterial[75]. Advancements in the control and manipulation of ASI systems have opened new avenues for research and applications. One example is advanced characterization techniques like photoemission electron microscopy (PEEM) using x-ray magnetic circular dichroism (XMCD) contrast[74, 76, 77]. These studies supplied direct experimental evidence supporting the theoretical framework of spin ices.

The theoretical foundation of ASI is deeply rooted in geometric frustration, where the spatial arrangement of elements prevents the minimization of energy in all interactions simultaneously. Several spins terminate at ASI vertices, and the spin orientation is subject to competing influences by neighboring interactions. This is sometimes referred to as the ice rules, which appear in the square ASI where vertices of similarly low energy compete[78]. This phenomenon often leads to a degenerate ground state and a wealth of emergent behaviors[79]. The topology of the ASI lattice thus plays a crucial role in its magnetic properties. Regular lattices of ordered vertices can support Dirac strings and magnetically charged quasiparticle excitations that emerge from the topology of the spin configurations[80]. These effective particles behave as positive or negative charges and can move through the lattice, providing a macroscopic manifestation of magnetic charge currents[74]. The interplay between geometric frustration, lattice topology, and the dynamics of emergent magnetic charges and their domains[81] creates a platform for exploring fundamental questions in physics, including the nature of phase transitions[82, 83]. These systems also allow the study of collective phenomena. Recent studies focus on the emergent phenomena in

ASI and their applications beyond the study of frustrated magnetism, such as their potential in realizing novel computational paradigms[35, 84].

There is a plethora of established ASI geometries. Some examples include the Ising, square, pinwheel, or Kagome ASIs, illustrated in Figure 2.3. Note that while the Ising model is not, strictly, an example of a spin ice, the physical implementation of the Ising model with artificial spins is here considered as a prototypical artificial spin system and referred to under the ASI label. Furthermore, there are also non-periodic tilings like the ASIs inspired by Penrose tilings[85, 86]. With parametrized design, it is possible to create ASIs of any imaginable design, such as the aperiodic, infinite Einstein tiling[87]. An ASI does not need to tile the plane, and there has been work in limited ASI configurations generated by an evolutionary algorithm to satisfy the demand of a computational fitness function[88, 89]. It is also possible to do arbitrary permutations to well-known lattices in order to introduce new and impactful effects, such as higher-order anisotropies, dilutions, or other methods I am not able to disclose here. ASIs offer an extensive toolbox of interesting nanomagnetic systems with many applications.

Recently, applications for ASI towards computation have been a focus of research. These research efforts make practical relevance of the large foundation of theoretical work related to ASIs, e.g., in implementations of neuromorphic computation or reservoir computation[33–35, 46, 90]. Computational models using a physical substrate, or a metamaterial, as a means of computation are examples of computation *in materio*. Magnetic systems can dissipate very little energy in information processing, and thus, material computation can be a viable candidate for future energy-efficient computation[42, 91, 92].

ASIs are nanomagnetic systems with a solid theoretical foundation and several promising technological applications. They exhibit exotic behavior, such as frustration and emergence, and provide a versatile metamaterial platform because of the tunability of their design. While the technological potential is vast, so is the design space, and much research remains.

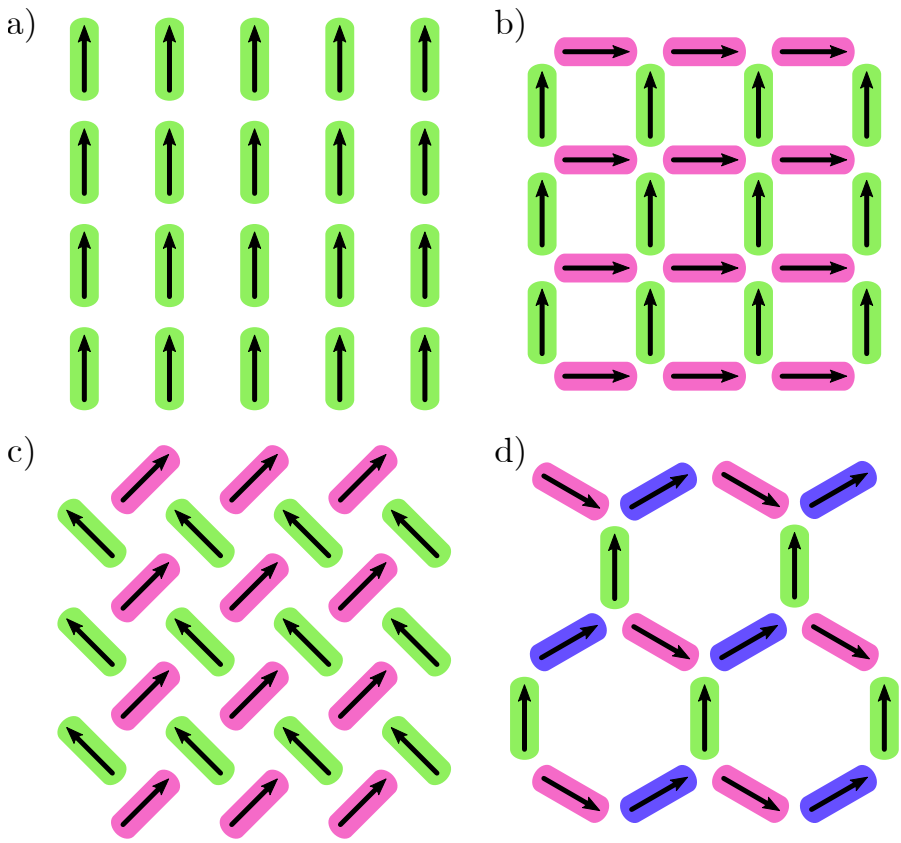


**Figure 2.3:** Schematics of some examples of conventional ASI geometries: a) Ising, b) square, c) pinwheel, d) Kagome.

# 3 Modeling nanomagnetic systems

## 3.1 Micromagnetic modeling

The continuum approximation, where materials are approximated as continuous media[93], is a powerful description of the physical world. When applied to the world of magnetic materials, the continuum approximation is described as the micromagnetic approach[94, 95]. Micromagnetic theory abstracts away the complex atomic origin of magnetism but is detailed enough to resolve domain walls and other sub-micron magnetization details. It can be applied to both magnetostatic equilibrium problems and dynamical problems.

Problems in micromagnetic modeling are solved by defining an initial magnetization state and applying an equation to evaluate and update the state. In equilibrium problems, the goal is to find a stable minimum, and a numerical solver explores the vast space of magnetization states to identify one with minimum energy. In dynamical problems, the goal is to find the next state, i.e., the time evolution of the system. These problems are governed by the Landau-Lifshitz-Gilbert (LLG) equation, which is expressed as

$$\frac{\partial \mathbf{M}}{\partial t} = -\gamma \mathbf{M} \times \mathbf{H}_{\text{eff}} + \frac{\alpha}{M_{\text{S}}} \mathbf{M} \times \frac{\partial \mathbf{M}}{\partial t}, \tag{3.1}$$

where $\mathbf{M}$ is the magnetization vector, $\mathbf{H}_{\text{eff}}$ is the effective magnetic field including external and internal contributions, $\gamma$ is the gyromagnetic ratio, $\alpha$ is the magnetic precession damping parameter, and $M_{\text{S}}$ is the saturation magnetization[96]. The first term on the right-hand side represents the precession of the magnetization vector around the effective field. The second term represents the damping that aligns $\mathbf{M}$ with $\mathbf{H}_{\text{eff}}$, leading to energy dissipation and the eventual stabilization of $\mathbf{M}$ in the direction of $\mathbf{H}_{\text{eff}}$. Equation Equation (3.1) combines both the dynamics of magnetization

precession due to the magnetic field and the relaxation towards equilibrium through damping. In modern uses of micromagnetic modeling, the equation is solved by computationally efficient numerical solvers and simulation tools.

Two of the most common micromagnetic simulation tools are OOMMF and mumax$^3$ [97–99]. The framework most used in this thesis is the mumax$^3$ framework developed by the DyNaMat group at Ghent University. mumax$^3$ uses finite-difference discretization and defines the model world on a grid. Properties like fields and magnetization are evaluated at the grid cell centers, while couplings like the exchange interaction are evaluated at grid cell interfaces. All physical contributions — such as thermal effects, electrical currents, or spin-transfer torques — are expressed in terms of effective fields or magnetic torques. The sum of the effective fields and torques are used to solve Equation (3.1) with respect to energy minimization or time evolution.

The physical contributions available in mumax$^3$ include spin-transfer torques[18, 100], the Dzyaloshinskii-Moriya interaction[101], the magnetocrystalline anisotropy[102], and thermal fluctuations[103]. Including these phenomena allows the assessment of micromagnetic systems for various device applications, including electrical interactions. However, the most relevant contributions for the work in this thesis are the magnetostatic field, the exchange interaction[94], and the Landau-Lifshitz torque[104, 105]. With these three contributions, it is possible to calculate the equilibrium state and switching characteristics of a nanomagnetic element with no magnetocrystalline anisotropy, such as the polycrystalline Permalloy (NiFe) structures used in this thesis. In figure Figure 3.1, the relaxed magnetization configuration of a typical nanomagnetic element is shown. Such simulations can help infer the single-domain state of various nanoparticle shapes, calculate their stray fields, or even their switching characteristics.

mumax$^3$ provides trustworthy solutions to problems relating to the properties of nanomagnetic elements, such as the hysteresis behavior. Simulation of the critical field-strength switching threshold for a range of angles can provide a characteristic switching curve similar to that of Figure 2.2f. In Figure 3.2, the magnetic hysteresis curve for two field angles, the total characteristic switching curve, and the corresponding states of a typical stadium nanomagnet, as obtained from mumax$^3$ simulations, are shown.

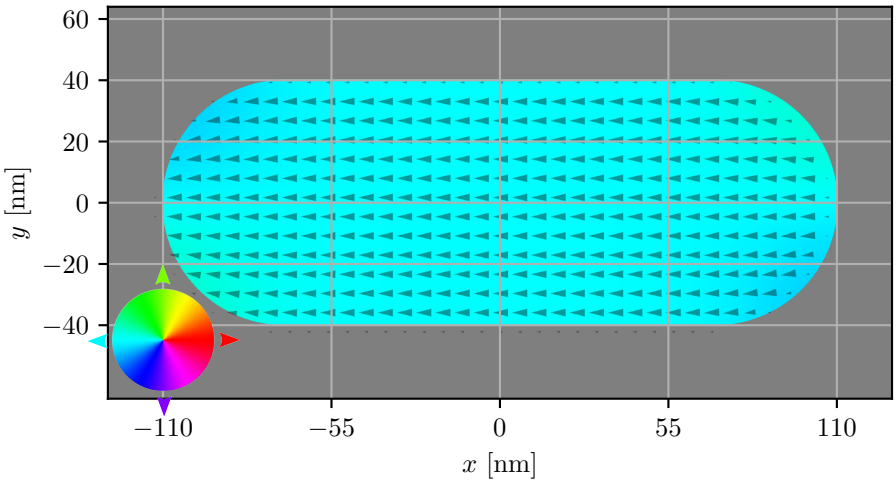


**Figure 3.1:** Mumax simulation showing the relaxed magnetization of a typical stadium-shaped nanomagnet. The magnet is 220 nm × 80 nm in length and width, and 10 nm thick in the plane. The color wheel indicates the magnetization direction that each pixel represents. Gray is non-magnetic. The magnet has a coherent single domain with slight aberrations near the ends due to shape anisotropy.

There are no inherent limitations to the geometries that mumax$^3$ can simulate, except those set by the finite-difference discretization. Parametrization allows a search for optimal properties through the automatic construction of geometries. The configurations are not limited to periodic structures, and other algorithmic tilings are easily accessible. It is only the imagination of the creator that limits the possibilities. One example of a non-regular packing, which tiles the plane and is algorithmically defined, is shown inFigure 3.3. Parametrization of geometric design is a powerful technique that has been extensively used in this thesis.

mumax$^3$ offers an incredibly versatile micromagnetic platform. However, there are limitations, particularly concerning the size of the system. The size limitation is due to the computationally costly nature of micromagnetic modeling. Because simulations using micromagnetic models must be limited in size and scope, at least with the limitations of current computer hardware, a higher level of abstraction is needed to model large-scale nanomagnetic systems.

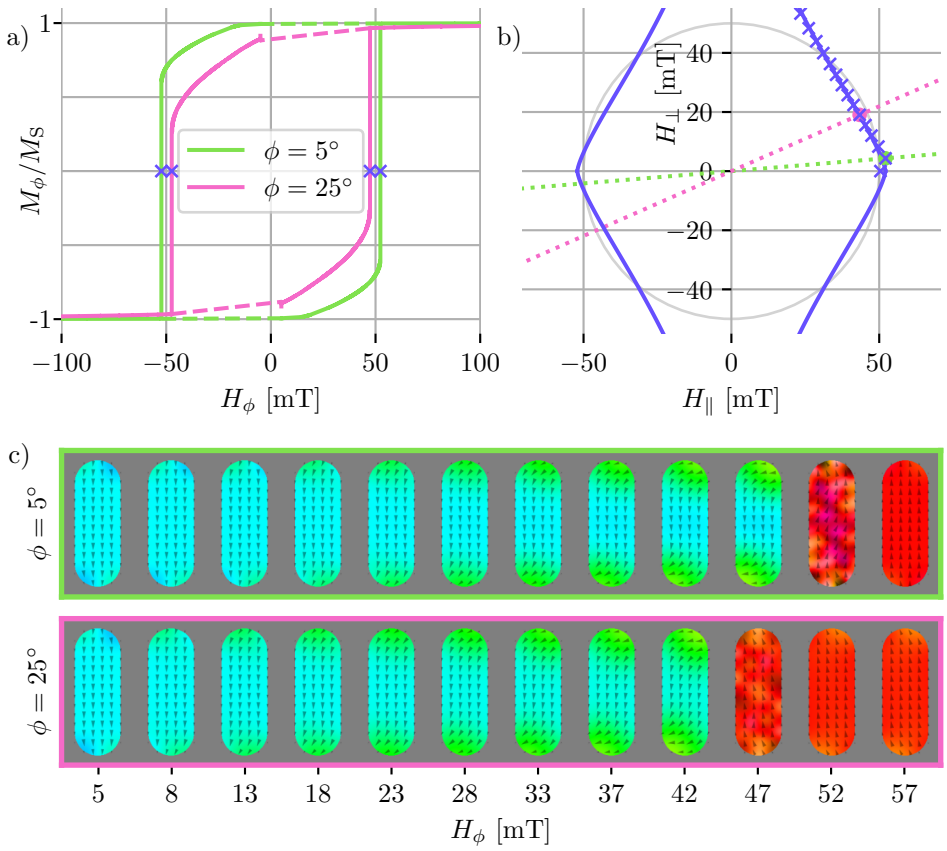


**Figure 3.2:** Switching characteristics of a simulated nanomagnet. a) Hysteresis curves of the stadium-shaped nanomagnet (Figure 3.1) for two applied fields $\mathbf{H}_\phi$ along an angle $\phi$ with respect to the long axis. Purple crosses mark the critical switching field strength where the magnetization switches. Dashed lines are interpolated as only the increasing parts of the field sweeps where simulated. b) Critical switching curve for the nanomagnet (purple line) obtained from mumax[3] simulations. The critical fields are expressed in terms of the parallel and perpendicular components with respect to the magnet's long axis. Purple crosses mark the identified critical switching fields and the purple line represents the extracted critical switching curve mirrored to the other three quadrants. The dotted lines indicate the two field directions of $\phi = 5°$ and $\phi = 25°$). c) Magnetization states for selected values of the applied field $\mathbf{H}_\phi$ up to switching.

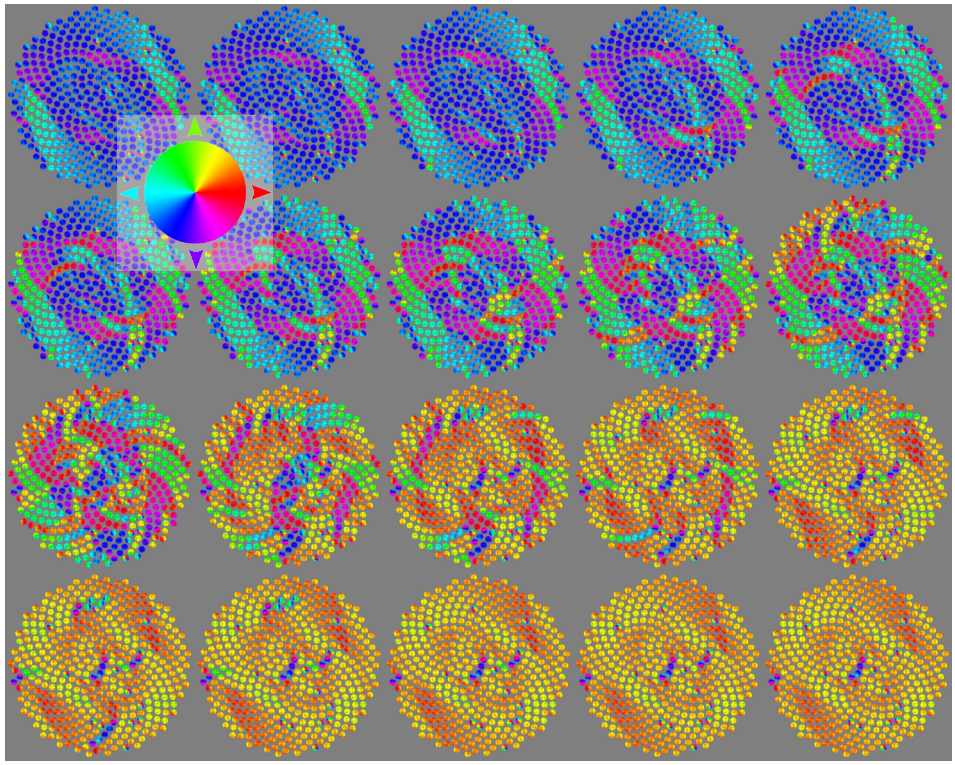

**Figure 3.3:** Example of algorithmically defined nanomagnetic structure simulated in mumax$^3$: a sunflower tiling[106] of NiFe nanodisks. The shown states are the remanent relaxed states at different points during a magnetic field sweep, starting at the top left. Each nanodisk is 100 nm in diameter and each sunflower is 2.8 µm across.

## 3.2 The point-dipole model

The complexity of nanomagnetic systems requires various modeling approaches, each with its abstractions and approximations. A higher level of abstraction compared to micromagnetic modeling is to consider the internal structure of a nanomagnet as being effectively represented by the characteristic behavior of a single spin[107]. This approach leads us to the point-dipole model, a widely used abstraction that, despite its simplicity, provides insightful predictions for the behavior of nanomagnetic systems[75, 108].

In the point-dipole model, each nanomagnet is approximated by a single spin of no physical extent, a point-dipole, and the internal magnetization structure is ignored[72]. The spin has a well-defined state (a magnetic moment), an associated stray field, and criteria for switching. The state is defined by the orientation of a magnetic moment assumed to be concentrated at a single point in space. A bistable magnetic moment similar to the bistable states of an elongated magnetic nanoparticle is often used. For a given state, the point dipole is the source of a magnetic dipolar field. Switching dynamics, or the reorientation of the dipole moment to another stable state, can be induced by stimuli such as external magnetic fields or thermal fluctuations. Th point-dipole model allows for the straightforward calculation of magnetic fields and interactions between dipoles, assuming that the magnetic elements' spatial extension and internal structure can be neglected.

The magnetic field $\mathbf{H}_{\text{point dipole}}$ generated by a point-dipole spin is described by the magnetic dipolar field equation,

$$\mathbf{H}_{\text{point dipole}}(\mathbf{r}) = \frac{1}{4\pi}\left[\frac{3(\mathbf{m}_{\text{dip}}\cdot\mathbf{r})\mathbf{r}}{r^5} - \frac{\mathbf{m}_{\text{dip}}}{r^3}\right], \tag{3.2}$$

where $\mathbf{m}_{\text{dip}}$ describes the magnetic moment of the spin and $\mathbf{r}$ is the position vector relative to the spin with length $r$.

The evaluation and temporal evolution of nanomagnetic systems modeled by point dipoles can be approached through various computational methods. Monte Carlo simulations are particularly common and explore the statistical mechanics of dipolar systems, allowing for the study of ensemble statistics and equilibrium properties. These simulations can be athermal

investigations of applied-field driven dynamics[76, 108] or thermal behavior such as equilibrium and transition rates driven by stochastic Metropolis updates[109, 110] and kinetic Monte Carlo modeling[109, 111]. The investigation of relaxed states of ASI systems has typically used Monte Carlo simulations in conjunction with thermal annealing experiments[70, 112, 113]. While the Monte Carlo approach is a probabilistic model that searches for an outcome, an equilibrium, or stable transition rates, it is not ideally suited for calculating the path or dynamical evolution of a system[114]. Simulating the dynamics of nanomagnetic systems might be better approached through other methods that carefully evaluate the switching criteria and sequences.

With the point-dipole approach, modeling nanomagnetic systems of vast sizes are possible. In this way, the emergent properties of nanomagnetic metamaterials can be explored in a computationally efficient manner. Furthermore, parametric design is essential in optimizing the configurations and interactions within these systems, and the versatility of the point-dipole model helps realize nanomagnetic arrays and devices with tailored properties. One example is shown in Figure 3.4, where parametric design is used to simulate a system that interpolates between the square and 45°-pinwheel ASIs.

The point-dipole model is a robust approximation but is still an approximation. The assumption of magnetic moments being localized to points neglects the effects of spatial extension and non-uniform magnetization textures of real nanomagnets. This neglected detail will, in turn, affect the emitted stray fields and thus the important interactions that govern nanomagnetic systems' emergent behavior. While the point-dipole approximation is often valid and useful, it should be applied cautiously, and its predictions validated against more comprehensive models and experimental observations whenever possible.

## 3.3 The dumbbell-dipole model

Minor adjustments can be introduced to enhance the accuracy of the point-dipole model without significantly increasing computational complexity. One such refinement is the dumbbell-dipole model, which represents each

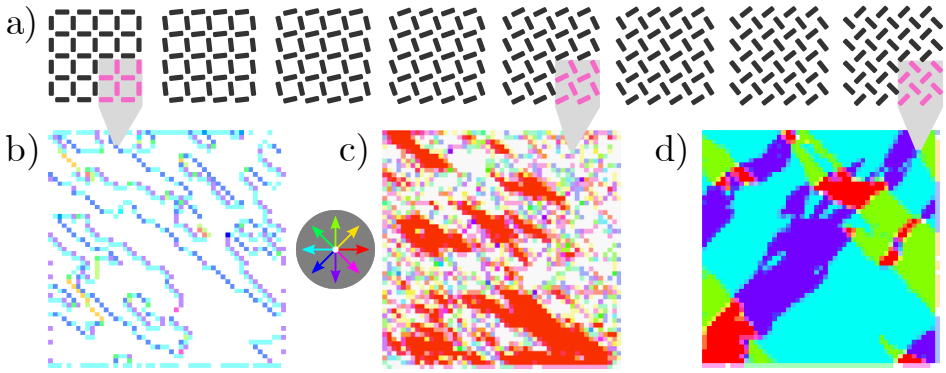


**Figure 3.4:** Examples of parametrized geometries and large-scale simulations. a) The geometries spanning from the typical square ASI to the 45°-pinwheel structure, with intermediate element rotations. b-d) Shows the magnetization of the relaxed states of some of the systems, indicated by gray guides. Each pixel represents the sum of the magnetization of eight magnets, highlighted in pink in a. The circular color chart depicts the color representation of the summed magnetization direction for each pixel.

magnetic moment not as a singular point but as two opposite charges separated by a finite distance. This approach can better capture the spatial extent of magnetic moments and their interactions[72]. It differs most significantly in the near-field region, as illustrated in Figure 4 of Paper II.

The dumbbell-dipole model has been used in theoretical works of ASI where the emergent magnetic monopoles are considered as magnetic charges[80]. In this picture, the dumbbell model is used to calculate the energy contribution of a particular magnet's state using the system's Hamiltonian. This calculation can be done by considering the net magnetic charge at the system's vertices and assigning the corresponding Coulomb interaction energies.

As in the point-dipole approximation, the dumbbell dipole can represent a single magnetic moment in which a magnetic state emits a corresponding stray field. The field produced by a dumbbell dipole can be expressed as a sum of the fields from two magnetic charges (monopoles), incorporating the separation distance to account for the physical extent of the dipole. This

dumbbell-dipole stray field can be expressed as

$$\begin{aligned}\mathbf{H}_{\text{dumbbell}}(\mathbf{r}) &= \mathbf{H}_{\text{monopole}}(\mathbf{r}-\mathbf{a}) - \mathbf{H}_{\text{monopole}}(\mathbf{r}+\mathbf{a}),\\ &= \frac{q_m}{4\pi}\left[\frac{\mathbf{r}-\mathbf{a}}{|\mathbf{r}-\mathbf{a}|^3} - \frac{\mathbf{r}+\mathbf{a}}{|\mathbf{r}+\mathbf{a}|^3}\right],\end{aligned} \tag{3.3}$$

where $\mathbf{r}$ is the position vector relative to the center of the dumbbell-dipole, $q_\text{m}$ is the monopole charge, and $\mathbf{a} = d_\text{dip} \cdot \hat{\mathbf{d}}_\text{dip}/2$ is the distance vector from the center to the dumbbell-dipole ends. The quantity of the magnetic monopole charge $q_m$ is determined using the magnetic dipole (as used in Equation (3.2)) such that $q_\text{m} \cdot d_\text{dip} = |\mathbf{m}_\text{dip}|$.

The two charges of the dumbbell-model and Equation (3.3) are hypothesized magnetic charges and do not represent any fundamental physical magnetic monopoles — these are still forbidden by the conservative magnetic field of Maxwell's electromagnetic formulation[12]. Still, it can be helpful to use such theoretical measures as these models can better capture the fields of real, fabricated nanomagnetic systems in physical experiments.

# 4 Experimental realization and characterization

## 4.1 Fabrication of nanomagnetic systems

Creating nanomagnetic structures requires precision and control at the nanometer scale. One method to achieve such control is electron beam lithography (EBL), a cornerstone technique in nanofabrication. EBL can pattern extremely fine features down to a few nanometers and is widely used to create bespoke nanostructures or the photolithography master masks of the tremendously optimized CMOS industry.

The core concept of EBL is to use a focused beam of electrons that directly writes designs onto a resist-covered substrate. Incident electrons change the chemical structure of the resist. The resist is a polymer coating spin-coated onto the substrate before exposure in the EBL. In the EBL, electrons are emitted from a field emission gun and accelerated to high speeds by acceleration voltages typically ranging from 20 keV to 100 keV[115]. At the surface of the substrate, the focused electron beam interacts with the resist, in a small interaction volume. Within this volume, the resist either undergoes cross-linking, enhancing its resistance to a developer, or scission, making it more soluble depending on the resist used[116]. Electrons that are subsequently backscattered by the substrate will lead to overexposure in a much larger region than the precise beam spot, which is termed the proximity effect[117]. The proximity effect depends on details of the design pattern, the electron beam, the resist and the substrate. This effect is typically mitigated by sophisticated pre-processing and modeling to compensate for the electron scattering[118]. This design correction process is known as proximity effect correction.

After exposure, the substrate develops in a chemical bath to dissolve the

most soluble, non-cross-linked resist, revealing a patterned resist layer. The patterned resist is used as a template for transferring the design pattern in further processing steps.

Following patterning with EBL and development, some material will either be added to or removed from the substrate. In this thesis, the additive process of lift-off was used. First, an electron beam evaporates a target material, depositing thin layers on the substrate that precisely conform to the developed resist pattern. The lift-off process then removes the resist and the material deposited on the resist using a chemical bath with a strong solvent. The solvent dissolves the remaining cross-linked resist, leaving behind the desired structures. In order to create the nanomagnetic systems in this work a magnetic nickel-iron alloy, $Ni_{0.8}Fe_{0.2}$, is used as the target material during the electron beam evaporation. This alloy is also known as Permalloy. Typically, a second material, such as aluminium, is deposited as an oxidation barrier. The EBL and lift-off method ensures high fidelity of the intended design and the final magnetic configuration. An overview of the process is depicted in Figure 4.1

Scanning Electron Microscopy (SEM) characterization plays a critical role in verifying the accuracy and quality of the fabricated structures. The working principle is similar to the EBL's but has a few differences. While the EBL only exposes the sample to the electron beam in areas defined by the design, the SEM raster scans or meander scans an extended field of view. Measuring the rate of emitted electrons, such as secondary electrons, during this scan provides a contrast mechanism for constructing a micrograph. SEM provides high-resolution images that allow for the examination of pattern fidelity, edge roughness, and the detection of any fabrication anomalies. Additionally, it can be used to measure critical dimensions and distances between nanomagnetic elements.

One key parameter in the design and fabrication of nanomagnetic systems is the critical minimum distance between individual elements, which largely determines the magnetic coupling strength. Controlling this distance is crucial for engineering the desired magnetic interactions and behavior within the system. Achieving uniformity and precision in the minimum dimension is essential for the reproducibility and performance of nanomagnetic devices.

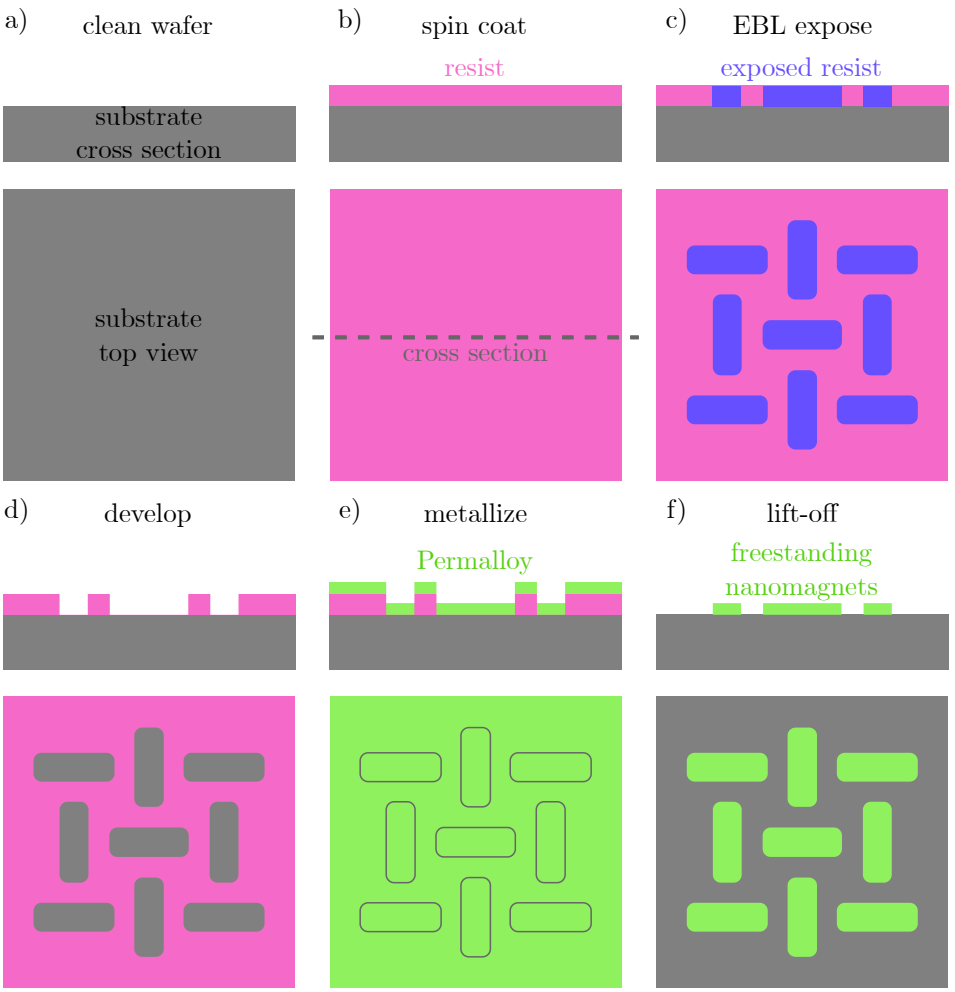


**Figure 4.1:** EBL and lift-off process. a) The process starts with a clean wafer. b) Resist is applied through spin-coating. c) The resist is exposed in the EBL. d) The pattern is developed by dissolving non-cross-linked resist. e) Magnetic material is added through metallization. f) Excess material is removed in the final lift-off step, leaving freestanding nanomagnets.

## 4.2 X-ray magnetic circular dichroism photoemission electron microscopy

Understanding intricate behaviors and properties of nanomagnetic systems, such as artificial spin ice, requires sophisticated imaging and analysis techniques to capture and interpret the tiny magnetic fields and moments these systems exhibit. Many experimental techniques can provide such characterization, such as magnetic force microscopy (MFM), magneto-optic Kerr effect (MOKE) microscopy, and vibrating-sample magnetometer (VSM) measurements or superconducting quantum interference device (SQUID) magnetometry. The experimental characterization presented in the papers of this thesis is performed by probing nanomagnetic systems with x-rays. The technique used in this thesis relies on x-ray magnetic circular dichroism to provide a signal in a photoemission electron microscopy (XMCD-PEEM) setup.

### 4.2.1 X-ray magnetic circular dichroism

Dichroism is the polarization dependent absorption of radiation in a material. This effect can be exploited to probe important material properties, such as a material's magnetization. One specific example of dichroism is x-ray magnetic circular dichroism (XMCD). A testament to the importance of this technique is the experimental observation one year after its theoretical prediction in the mid 1980s[119, 120], despite requiring significant resources. The fundamental principle is the increased or decreased absorption of x-rays with a defined circular polarization depending on the magnetization in the material. An important concept is the optical helicity which is positive for right-handed circular polarization along the propagation direction or negative for left-handed circular polarization. The difference in absorption is due to the selective x-ray excitation of a material's core electrons depending on the helicity of the x-rays and the magnetization of the material.

In the core electrons of a $3d$ transition metal, spin-orbit coupling leads to a splitting of the $2p$ band: the $j = 3/2$ states ($L_3$ edge, parallel coupling) and the $j = 1/2$ states ($L_2$ edge, antiparallel coupling). The electrons in the split $2p$ bands can be excited by incoming x-rays. The probability of

excitation will depend on the available spin-up or spin-down holes, which are a function of the material magnetization. This selective excitation leads to a net increase in absorption for x-rays with positive helicity at the $L_3$ edge (and a net decrease at the $L_2$ edge) for materials magnetized along the direction of positive helicity. The x-ray absorption spectroscopy (XAS) for circularly polarized x-rays is thus a function of the material magnetization direction with respect to the polarization and propagation of the x-rays. The x-ray magnetic circular dichroism (XMCD) signal is defined as the difference between XAS for positive and negative circular polarization and is directly related to the magnetization direction of a material[121].

XMCD requires circularly polarized x-rays, tuned to the specific energies of the $L_3$ or $L_2$ edges in the material. This tunable energy, polarization, and high radiation intensity require a highly specialized radiation source.

### 4.2.2 Synchrotron x-rays

Synchrotrons are the most advanced light sources we have. They are large facilities that house electron accelerators capable of accelerating electrons up to extremely high energies in the giga electron volt (GeV) range[122]. Synchrotron facilities are large premises housing an electron accelerator. These consist of a large storage ring, and typically a linear accelerator and at least one smaller accelerator ring. Along the storage ring there are beamlines that use radiation produced by the ring for a plethora of different experiments, from x-ray powder diffraction to x-ray nanoprobes[123].

The electrons are forced to follow the circular paths of the accelerator ring using powerful bending magnets. At each turn, the electrons are accelerated in order to change direction and this change in momentum emits electromagnetic radiation, the original source of high spectral brightness illumination in synchrotrons. Modern synchrotrons use so-called magnetic insertion devices such as wigglers and undulators in strtaight sections of the ring to produce radiation of even higher spectral brightness[124].

The radiation is thoroughly filtered at each beamline before reaching the experimental end station. In a typical experiment, only a small part of the broad emission spectrum is used; for example, only a narrow energy

range is required for XMCD techniques. For good XMCD contrast in thin films of the magnetic material NiFe, circularly polarized light of the Fe $L_3$ edge around 707 eV is frequently used[125, 126]. These soft x-rays have a shallow penetration depth and special techniques are used to measure the local absorption.

### 4.2.3 Photoemission electron microscopy

When probing a nanomagnetic system using x-ray absorption, it is useful to measure the local absorption with a spatial resolution at least down to the magnet size. Because of the shallow penetration depth of the soft x-rays used for XMCD, transmission techniques require preparation of thin samples, typically on silicon nitride membranes of roughly 100 nm thickness[127]. Scanning transmission x-ray microscopy (STXM) allows superb time and space resolution[128, 129], but requires sophisticated x-ray optics[130]]. Fortunately, x-ray absorption in a material also emits photoelectrons[131] and scattered secondary electrons from the surface. These electrons can be collected, accelerated, and projected onto a detector screen to form a micrograph with XMCD contrast[132]. The electrons escape from a shallow escape depth close to the material surface where there are incident x-rays and thus provide a surface sensitive signal. The result is an absorption signal which is highly selective for two reasons: selective absorption that depends on the direction of magnetization and shallow electron escape depths that provide a signal of this absorption only from the surface of the imaged material. In other words, the signal provides information about the microscopic magnetization of a material at its surface.

Photoemission electron microscopes collect the photoelectrons and secondary electrons emitted from the sample which acts as a cathode placed close to an electrostatic objective lens. The electrons are accelerated using a strong field of about 10 kV to 30 kV between the sample and the objective lens, typically within millimeters of each other. Further, the electrons are collimated and guided by electron optics, such as electrostatic and magnetic lenses. They pass through several apertures and energy filters to select the proper contrast and focal planes. Finally, they reach a phosphor screen or a microchannel plate, where the electrons are captured as a digital image. There are many sources of aberrations and resolution loss, such as vibrations and inherent

astigmatism, and higher-order aberrations in the electron lenses, which can distort the image. The final result is a magnetic contrast image with a spatial resolution down to 20 nm or even a few nanometers[132].

The magnetic contrast images available through XMCD-PEEM offer an invaluable path to direct observation of experimentally fabricated nanomagnetic systems, such as artificial spin ices, and has been extensively used in this work.

### 4.2.4 Data analysis

Obtaining the XMCD-PEEM micrographs is one part of characterizing the microstates of artificial spin ices, although a challenge remains: converting the experimental data to a single-spin-resolved microstate. It is relatively easy to observe the images by eye and make out the apparent states of the ensembles (see Figure 2, Paper II), but with several thousand nanomagnets per ensemble, manual decoding of the microstate is not practical. Machine readout is complicated by non-linear aberrations in the electron optics of the PEEM setup, and it is not possible to simply apply a mask and read out the state of each magnet. In order to decode the experimental data, we perform an extensive semi-automatic segmentation process. The following section is a description of this process as it was performed for Paper II.

The data extraction process starts with a straightforward XMCD-PEEM analysis using the x-ray absorption images of the two polarizations: drift correction, averaging, and calculation of the normalized difference. This processing yields a magnetic contrast image. Through a semi-automatic process, the corners of the ensembles are extracted. Further, a homeographic transformation is applied to square the four corners, correcting some of the original image's non-linearity. The images are cropped to the same size, which includes the ensembles plus some surrounding padding. The dataset is now a stack of 2D images containing a nanomagnetic structure whose orientation and position are identified and can be mapped to the known lithographic mask and the four corners of the nanomagnetic system.

The magnetic contrast image and the mapped nanomagnetic structure are still insufficient for automatic microstate extraction. Despite our best efforts

at regularization, each pixel is subject to noise and significant variations in contrast across the picture. If we run an automatic extraction directly on these pixels based on some fixed or dynamic threshold, we invariably lose details or retrieve a completely useless extraction. The problem is now reduced to a classification task, sorting pixels into categories of positive magnetic contrast, negative magnetic contrast, or no magnetic contrast. Such classification tasks are ideally suited for machine learning.

To perform machine learning on our images, we apply the ilastik framework[133] originally intended for bioimage analysis. It helps researchers perform a semi-automatic segmentation of microscopy images. In order to classify a pixel in a manner more reliable than a simple threshold, we need to account for the context in which it exists, i.e., its neighborhood. The context is accounted for by associating each pixel with multiple values resulting from filters of different types and strengths, e.g., gaussian blurs with different standard deviations, which ilastik terms as pixel features. We then label some pixels for each category, and ilastik trains on the labeled data using standard machine learning algorithms to map features and combinations to different pixel categories. This process is repeated iteratively across images to produce a trained classifier that can classify pixels with high confidence.

By training an image classifier to recognize pixels associated with different magnetic states, a high-confidence segmentation image can be produced for each magnetic contrast image. The resulting segmented images can be used to map the state of the nanomagnetic system with spin-perfect resolution. The extracted microstates can be further analyzed in simulations such as flatspin calculations of the configurational energies. This approach might also be applicable to other imaging techniques, such as MOKE imaging, enabling spin-perfect resolution through machine learning where such data extraction would otherwise be too time-consuming. The method has proven particularly useful where the sheer volume of data or the subtlety of the features of interest would either overwhelm or be unavailable through traditional analysis techniques.

# 5 Discussion

## 5.1 Summary of papers

### Paper I
**flatspin: a large-scale artificial spin ice simulator**
**Physical Review B**

The article introduces *flatspin*, a simulator for large-scale ASI systems. The simulator is based on a point-dipole representation of nanomagnets with bistable spins. It is GPU-accelerated and can handle large systems of two-dimensional configurations. The switching criteria are inherently deterministic and build on the Stoner-Wohlfarth model but are generalized to include the effects of non-elliptical nanomagnets. The switching curves are based on micromagnetic simulations, which offer higher fidelity than the traditional point-dipole picture. All modeled phenomena are encoded as effective fields, such as the dipole field, the external field, and the effective thermal field. The thermal field in flatspin is a novel implementation where we convert a switching probability, based on a Poisson distribution of the Arrhenius-Néel equation[134], to an effective magnetic field.

flatspin is validated against known analytical and micromagnetic results. Additionally, it is compared to non-trivial experimental results such as the formation of Dirac strings in Kagome ASI, the growth of magnetic crystallites in square ASI, and ferromagnetic order in 45°-pinwheel ASI. The latter is shown to reproduce switching characteristics of the system that have previously eluded modeling[135]. Furthermore, a property of the square ASI is investigated: its robustness to dilution defects, i.e., removal of random magnets. As dilution defects are introduced, the relaxed state of the square ASI is surprisingly robust in terms of vertex type prevalences. However, the typical domain sizes are significantly reduced.

flatspin represents an advancement in ASI simulation, offering versatile, efficient, and trustworthy simulations of millions of magnets. It facilitates studies exploring large-scale and emergent behaviors in these nanomagnetic systems.

## Paper II

### On the Antiferromagnetic–Ferromagnetic Phase Transition in Pinwheel Artificial Spin Ice

**in review**

The article explores the phase transition from antiferromagnetic (AF) to ferromagnetic (FM) ordering in square lattice artificial spin ices as the magnetic elements are rotated into a pinwheel configuration. This transition was experimentally observed using x-ray spectromicroscopy, revealing a critical transition angle that depends on the separation between the nanomagnets. This finding contrasts with previous studies that relied on the point-dipole model. We also find significant coexistence of the AF and FM phases through the continuous transition.

Further, the paper demonstrates that a more detailed dumbbell-dipole model, which includes the effects of the nanomagnet's extension, explains the experimental data. Simulations using this model show that the critical angle for the AF–FM transition varies with the separation of the nanomagnets.

The paper presents an intuitive demonstration of ordering phenomena in a nanomagnetic system. Our main findings establish that the AF–FM transition is continuous, supports coexisting phases, exhibits a coupling-dependent transition angle, and requires an important change to theoretical models. We conclude that minute details of the nanomagnet stray fields have important implications for the magnetic ordering of ASI, which is relevant to both fundamental physics and potential technological applications.

## Paper III
### Clocked dynamics in artificial spin ice
### Nature Communications

The article presents *astroid clocking*, a method to control artificial spin ice dynamics. This technique uses the shape and orientation of the nanomagnet's critical switching curves for precise control over local ASI features using global magnetic fields. The paper presents a general principle for field protocols that allow athermal ASI dynamics to evolve with each applied field pulse in a 45°-pinwheel ASI. There is no state change between field pulses — the dynamics are clocked. We explain the mechanism of the method in detail through simulations and show that it relies on the inherent dynamics of the ASI itself.

We show through experiments two different field protocols: unipolar clocking and bipolar clocking. The experiments use a vector magnet in an XMCD-PEEM setup to control the state of the fabricated nanomagnetic systems. The unipolar clock protocol monotonically grows or shrinks domains of a selected type at specific domain boundaries. The bipolar clock protocol does not result in monotonic growth but a combination of selective growth and reversal in each clock cycle. This combination of selective growth and reversal leads to changes in domain morphology and net growth or net shrinking. Contrary to intuition, the pulses of the bipolar clock protocol are symmetric but still result in net growth or net reversal, depending on the order in which they are applied.

Clocking the dynamics of ASIs enhances our ability to control them. Furthermore, the precise manipulation of magnetic domains that depends on the specifics of the domain boundaries represents an unprecedented local control using global fields only. Astroid clocking's practical availability and effectiveness mark a significant step forward in the control and exploration of emergent behaviors in nanomagnetic systems.

## 5.2 Discussion of papers

The work in this thesis starts with the foundational simulator flatspin, which the rest of the research builds on. flatspin is thoroughly validated in the first paper. The simulator itself has been extensively used for the rest of the work and has also been used in other research[89, 136, 137].

The effective thermal field implementation of flatspin is thorough and offers a completely new approach to modeling the thermal dynamics of artificial spins, although it is not where the simulator stands out. Numerous studies of ASI involve Monte Carlo modeling of thermal dynamics and equilibria[70, 75, 78, 138, 139]. These typically express the system energies through the formulation of a Hamiltonian, either using a vertex configuration model or a dipolar coupling model, and standard Monte Carlo updates such as the Metropolis-Hastings method. Monte Carlo modeling of this kind is perfect for thermal equilibrium states or transition rates. This method differs from the flatspin method, which does not accept or reject proposed states based on their energies. Instead, flatspin adds stochastic fields based on a probability distribution and immediately performs any transitions whose energy barriers are surpassed. If several spins are flippable at any simulation step, the transition that presumably occurred first, i.e., the nanomagnet with the state energy furthest above its energy barrier is flipped first, and the total state is reevaluated. In the case of no temperature, flatspin is deterministic, and temperature adds the stochastic thermal field to the deterministic process. We argue that the approach in flatspin reveals real dynamics and state trajectories of a given system in any given state, not statistical averages. Calculating the effective thermal field is computationally costly, and the required fine-tuning of the dynamical time step is, unfortunately, a significant drawback of the simulator. However, the strength of flatspin lies in its athermal deterministic dynamics.

It is worth noting that micromagnetic modeling mumax also suffers a performance loss when simulating thermal effects. We have been unable to simulate even a single thermal spin flip in micromagnetic simulations at any realistic time scale. To the author's knowledge, this has yet to be done, except for small magnets and fields close to the coercive field[140]. It is an example of a rare event in a high-dimensional complex system where

it is notoriously hard to bridge the gaps in time scale when simulating phenomena of vastly different characteristic times[141].

The novelty and usefulness of flatspin lie in the increased fidelity offered by the generalized Stoner-Wohlfarth switching model and its GPU-accelerated efficiency. Because of these two unique properties, it bridges the gap between micromagnetic models like mumax$^3$ and higher abstraction models like point-dipole models.

While the Stoner-Wohlfarth model is widely known, it is less ubiquitously made use of in point-dipole models. Some point-dipole models instead apply a simple projection of the total field onto the long axis of the magnet and compare it to a coercive field strength to decide whether switching occurs. It has previously been assumed that Stoner-Wohlfarth switching does not provide any new dynamics in ASI systems of point dipoles compared to this simple projection criteria[81]. With flatspin, we show that this is false. The exact shape of the switching curve can have a tremendous effect on the resulting emergent dynamics, and we exploit this fact in Paper III with astroid clocking.

The characteristic switching curves implemented in flatspin are informed by micromagnetic simulations and can, in theory, encompass the switching characteristics of almost any magnet shape and size, given that they exhibit a bistable single domain. Switching curves can be obtained by micromagnetic simulations or by magnetic characterization of physically fabricated nanomagnets. The switching field threshold for a nanomagnet is expressed as,

$$\left(\frac{h_{\parallel}}{bh_k}\right)^{2/\gamma} + \left(\frac{h_{\perp}}{ch_k}\right)^{2/\beta} = 1, \tag{5.1}$$

where $h_{\parallel}$ and $h_{\perp}$ are the field components along the nanomagnet's long and short axes, respectively, and $h_k$ is the hard axis threshold. The parameters $b$, $c$, $\beta$, and $\gamma$ are free parameters that are used to fit the curve to the observed critical switching fields for a particular nanomagnet shape. The original Stoner-Wohlfarth model assumes a strict assumption of nanomagnetic switching by coherent rotation. This assumption is unnecessary in the generalized model as other switching mechanisms, such as domain nucleation and propagation, can be included because the model only accounts for the observed switching curve. While a considerable variation of nanomagnet

switching behavior can be described, there are limits to what switching characteristics Equation (5.1) can encompass. This limitation to flatspin could be accommodated by replacing the generalized Stoner-Wohlfarth astroid with any other parametrized curve to fit the bill.

There are other modifications that flatspin might accommodate for better results, as we conclude in Paper II. This paper directly results from the efficient simulations possible with flatspin, which allow quick parametrization and searches for optimal properties. Based on the ferromagnetic properties of the 45°-pinwheel ASI first presented as an emergent spin ratchet by Gliga et al.[142], we performed simulations of intermediate angle pinwheels interpolating between the square ASI and the 45°-pinwheel ASI. While the conclusion in Paper II reflects the necessity of a dumbbell-dipole picture, the unmodified flatspin simulator captured the essence of the phase transition and the coexisting antiferromagnetic and ferromagnetic phases. This study exemplifies how flatspin provides a foundation for further research and identifying new nanomagnetic systems. The second paper was the first attempt to reproduce new phenomena first seen in flatspin in real, fabricated systems, a litmus test of the trustworthiness of the simulator.

The design of masks for EBL is a critical step in the nanofabrication process. Mask design was aided by flatspin simulations, which helped define parameters like inter-island distances and rotation, specifying the geometric configurations of the ASIs. As in the parametrized simulation framework, parametrized mask design enables sweeping vast spaces of geometric configurations and establishes a direct pathway from simulation to fabrication. For fabricating the structures of this thesis, the GDSII-based CAD tool PHIDL has been extensively used[143]. This approach facilitates rapid prototyping, enabling the exploration of nanomagnet element parameters — such as size, spacing, and rotation — that impact the performance of nanomagnetic systems in ways that can be characterized experimentally. One example of such parametrization is the systems used in Paper II, which interpolates the geometry between the square ASI and 45°-pinwheel ASI. Besides this programmatic approach to mask design, the fabrication process has followed the standard procedures for patterning Permalloy with lift-off developed by Digernes[144]. The fabrication process has focused on repeatability and achieving precise minimum dimensions through rigorous lab work. However, novel techniques have not been introduced, and details of the fabrication process will not be discussed further.

In any fabricated system, there will be imperfections that can introduce disorder, i.e., quenched disorder. It can be challenging to implement new material systems for computation when disorder is prevalent, but it can also be beneficial and help reach a more significant number of unique states of the ensembles[81]. In flatspin, disorder is modeled as a perturbation of $h_k$, effectively softening the distribution of the coercive fields of the nanomagnets. While there are many types of disorder, such as disorder in island positions or orientations, they have a similar effect and can be characterized as an effective switching field disorder[145]. The samples in this thesis, fabricated through lift-off, might be improved and contain fewer defects if an etching process was used instead.

The disorder of the fabricated systems in Paper II did not affect the results. flatspin passed its litmus test, and the predicted continuous transition, coexistence, and tunability of the system were reproduced experimentally. This is an example of the power of parametrization of the nanomagnetic system, which allows for the search for unique properties.

While initial simulations of the system in Paper II were promising, we identified a slight change to the stray field representation through micromagnetic simulations that enabled flatspin simulations to capture the full quantitative and qualitative properties of the transition. The stray fields of flatspin are given by the point-dipole model of Equation (3.2). Replacing these fields with a dumbbell-dipole representation, as in Equation (3.3), is a small change to the model, which gives qualitatively similar results and incurs no performance penalty. By comparing the stray fields of the two dipole approximations with a full micromagnetic simulation, it is clear that the dumbbell-dipole matches the micromagnetic simulations more closely, particularly in near-field regions where the point-dipole approximation is known to break down[77]. We conclude in Paper II that the dumbbell-dipole model also provides a closer match to the experimental observations.

Expanding on the dumbbell-dipole model by incorporating higher-order magnetic multipoles, such as quadrupoles or octupoles, can further refine the representation of magnetic interactions. These extensions allow for a more detailed simulation of nanomagnetic systems informed by high-fidelity tools like mumax$^3$ as a benchmark for accuracy. Such higher-order multipoles might be implemented as point multipoles like the point-dipole model, sums of multipole moments with a physical extent like the two

monopoles of the dumbbell-dipole model, or a combination. One example could be a point dipole with two smaller point-dipole moments at the ends, effectively encoding an s-state or a c-state[146]. Some higher multipole representations were explored for Paper II. Although some quadrupole moment contributions were identified, a simple monopole dumbbell-dipole was sufficient to reproduce the necessary details and avoided unnecessary free parameters. Introducing such complexity might benefit simulations of other emergent behaviors of these nanomagnetic systems, but further studies would be needed to map this out. By iteratively comparing simplified models to 'ground truth' simulations, it is possible to incrementally improve the models while maintaining a balance between computational efficiency and physical realism.

Introducing higher-order multipole moments to flatspin might address one of the biggest arguments against the simulator: it ignores the internal microstructure of a nanomagnet. ASI dynamics can be influenced by aberrations at the ends and even thermal fluctuations of the microstructure at the ends[147]. Higher-order multipole moments can be included at almost no extra cost, and can account for this effect. However, the increased complexity required to keep track of all the new states and switching regimes would be a significant disadvantage. As Paper II demonstrates, it can be beneficial to use other models of the stray fields of the nanomagnets for specific experiments.

In conclusion, while models like the point-dipole model offer a foundation for understanding nanomagnetic systems, refinements such as the dumbbell-dipole model (and even the incorporation of higher-order multipoles) can provide a more accurate and nuanced understanding of magnetic interactions through stray fields. These models serve as tools in the simulation and design of nanomagnetic systems, bridging the gap between theoretical exploration and micromagnetic fidelity, bringing the systems one step closer to applications.

The discussion up until this point has focused on designing and modeling artificial spin ice, and fabricating and characterizing new systems as a way to tailor emergent properties, which can be useful for computation. However, other issues, like the system's input and output, must be addressed before practical applications are possible. We show in Paper III that flatspin can also help investigate how to interact with these systems.

Interacting with nanomagnetic systems is essential for their use in applications. Various methods have been proposed to interact with these systems, from highly localized to system-wide, or *global*, interactions. Local interactions refer to the targeted influence on a subset of nanomagnets within a system, allowing precise control. Notable methods for inducing local interactions include using an MFM tip[148, 149] and local Ørsted fields generated by small strip lines[150]. Additionally, spin-orbit torque (SOT) and spin-transfer torque (STT) interactions represent advanced techniques for influencing magnetic states[151, 152]. However, these methods are either impractical or require significant on-sample infrastructure, such as electrical circuits.

In contrast to the precision offered by local interactions, global fields affect the entire nanomagnetic system uniformly — in principle. We demonstrate in Paper III that astroid clocking, relying only on uniform field applications, can achieve local control over nanomagnetic systems. By carefully choosing the strength and orientation of applied field pulses, it is possible to reach more states of the system than by conventional application of magnetic fields. This shows that control at the local scale using a global input is possible. There have been claims that sequences of global fields do not provide access to a meaningful fraction of states and analytical proofs of the inaccessibility of certain states, e.g., the ground state of Kagome or square ASI. We believe these claims overlook the mechanism of the astroid clocking scheme[149, 153]. We show that the local magnetization state, or domain boundary structure, can dominate the switching dynamics when suitable field protocols are used. By exploiting the shape of the characteristic switching curves and their relation to the local dipolar interactions, field-driven dynamics can access a much larger fraction of states. Further, we hypothesize that many types of dynamics are yet to be uncovered for different domain configurations, even just in the 45°-pinwheel ASI. The work of Paper III barely scratches the surface, and more sophisticated clocking protocols should be explored in the future.

One of the main motivations for this thesis is energy efficiency in information processing. However, as presented in Paper III, astroid clocking relies on magnetic fields generated by magnetic coils with significant resistive losses. Other methods of generating these fields, such as non-resistive superconducting coils, might eliminate this energy inefficiency. STT-induced switching, can be envisaged, which will likely eliminate inductive loss as well.

The power of astroid clocking comes from the parallelizability of the method, which does not limit the size of systems or the number of nanomagnets that can be addressed at once. Additionally, the concept of controlling the emergent dynamics of ASI is the real breakthrough of astroid clocking.

Through astroid clocking, we show that athermal dynamics are useful and open up a previously unexplored world of ASI dynamics. With efficient modeling, parametrized design, and verification through experimental setups, this technique can be a foundational step toward useful ASI-based devices.

## 5.3 Conclusion and outlook

This thesis has presented a novel simulator, how the simulator can be used to design and predict properties of artificial spin ices, how these properties can be sensitive to small variations in the nanomagnets' stray fields, and an experimental technique that enables unprecedented control of the athermal dynamics of artificial spin ice systems.

The main goal of this thesis was to expand the framework for designing, controlling, and analyzing metamaterial systems of ASI. Through the papers, the work has provided valuable contributions to all three areas, with a new design process available through flatspin, a new control mechanism with astroid clocking, and the use of machine learning for experimental data extraction. The subgoals of the thesis, listed in Section 1.3, have been properly addressed: With flatspin, large-scale simulations enable the study of material properties, such as the transition properties of the antiferromagnetic–ferromagnetic transition in square lattice ASI (subgoal 1). Integrating flatspin and PHIDL offers a versatile and practical method of designing physical ASIs of any geometrical configuration (subgoal 2). Astroid clocking offers control over the states and dynamics of ASIs, although not complete control (subgoal 3). Using machine learning, we can enhance the extracted data from advanced imaging techniques like XMCD-PEEM (subgoal 4).

This thesis attempts to make the design and control of artificial spin ice-based systems more practically available. It offers valuable insights into

the modeling, sensitivities, and possible control mechanisms of artificial spin ices, especially in the athermal regime. The work provides tools and practices that enable further exploration, research, and applications of ASIs. These applications of ASIs might be helpful in energy-efficient and scalable computation.

While ASI research historically has focused on geometries that are either found in nature, inspired by well-known geometric designs and symmetries, or perturbations on these, the techniques presented in this thesis offer a new strategy: In line with the Bitter lesson, which points out that human attempts at encoding knowledge by design ultimately fail compared to efficient search and learn algorithms, a strategy of property search might be more fruitful. This strategy paves the way for an immense variation of controllable emergent ASI behaviors, some of which will likely be useful for the energy-efficient computing devices of the future.

There are many questions to be addressed before an ASI can be useful in specialized computation hardware. What are the valuable features, and what are their limits? How will these systems be robust to defects in the fabricated materials? How do we read out the states with sufficient spatial and temporal resolution in an energy-efficient manner compatible with a practical device? What are the bottlenecks for energy-efficient computing in ASI devices? How do the functional properties scale?

There is still a long way to go before we see ubiquitous ASI-based devices performing energy-efficient computing and providing the world's need for raw computational power. Fortunately, researchers are eager and excited to work with these systems, and there are many promising paths forward. Who knows what we will learn in the future?

I might even learn how to do a backflip.

# Bibliography


[1] *Definition of MATERIAL*, https://www.merriam-webster.com/dictionary/material (visited on 03/22/2024).

[2] R. M. Walser, "Electromagnetic metamaterials," in Complex Mediums II: Beyond Linear Isotropic Dielectrics, Vol. 4467 (July 9, 2001), pp. 1–15.

[3] *Materials that shaped history | School of Materials Science and Engineering - UNSW Sydney*, UNSW Sites, https://www.unsw.edu.au/science/our-schools/materials/engage-with-us/high-school-students-and-teachers/materials-shaped-history (visited on 03/22/2024).

[4] W. E. Kock, "Metal-Lens Antennas," Proceedings of the IRE **34**, 828–836 (1946).

[5] W. E. Kock, "Metallic Delay Lenses," Bell System Technical Journal **27**, 58–82 (1948).

[6] J. Ruze, "Wide-Angle Metal-Plate Optics," Proceedings of the IRE **38**, 53–59 (1950).

[7] W. Cai and V. Shalaev, *Optical Metamaterials*, 1st ed. (Springer New York, New York, NY, 2010), ISBN: 978-1-4419-1150-6.

[8] S. Bayda, M. Adeel, T. Tuccinardi, M. Cordani, and F. Rizzolio, "The History of Nanoscience and Nanotechnology: From Chemical–Physical Applications to Nanomedicine," Molecules **25**, 112 (2020).

[9] J. Stöhr and H. C. Siegmann, *Magnetism: from fundamentals to nanoscale dynamics*, 1st ed., Springer Series in Solid-State Sciences 152 (Springer, Berlin, 2006), ISBN: 978-3-540-30282-7.

[10] J. Marchant, "AI reads text from ancient Herculaneum scroll for the first time," Nature, 10.1038/d41586-023-03212-1 (2023).

[11] H. C. Ørsted, "Experiments on the effect of a current of electricity on the magnetic needle," Annals of Philosophy **16**, 273–276 (1820).

[12] J. C. Maxwell, "VIII. A dynamical theory of the electromagnetic field," Philosophical transactions of the Royal Society of London **13**, 459–512 (1865).

[13] P. Weiss, "L'hypothèse du champ moléculaire et la propriété ferromagnétique," Journal de Physique Théorique et Appliquée **6**, 661–690 (1907).

[14] F. Pfleumer, "Lautschrifttraeger," German pat. 500900C (Individual, June 26, 1930).

[15] M. N. Baibich, J. M. Broto, A. Fert, F. N. Van Dau, F. Petroff, P. Etienne, G. Creuzet, A. Friederich, and J. Chazelas, "Giant Magnetoresistance of (001)Fe/(001)Cr Magnetic Superlattices," Physical Review Letters **61**, 2472–2475 (1988).

[16] G. Binasch, P. Grünberg, F. Saurenbach, and W. Zinn, "Enhanced magnetoresistance in layered magnetic structures with antiferromagnetic interlayer exchange," Physical Review B **39**, 4828–4830 (1989).

[17] J. S. Moodera, L. R. Kinder, T. M. Wong, and R. Meservey, "Large Magnetoresistance at Room Temperature in Ferromagnetic Thin Film Tunnel Junctions," Physical Review Letters **74**, 3273–3276 (1995).

[18] J. C. Slonczewski, "Current-driven excitation of magnetic multilayers," Journal of Magnetism and Magnetic Materials **159**, L1–L7 (1996).

[19] L. Berger, "Emission of spin waves by a magnetic multilayer traversed by a current," Physical Review B **54**, 9353–9358 (1996).

[20] D. C. Ralph and M. D. Stiles, "Spin transfer torques," Journal of Magnetism and Magnetic Materials **320**, 1190–1216 (2008).

[21] J. E. Hirsch, "Spin Hall Effect," Physical Review Letters **83**, 1834–1837 (1999).

[22] C. L. Kane and E. J. Mele, "Quantum Spin Hall Effect in Graphene," Physical Review Letters **95**, 226801 (2005).

[23] M. König, S. Wiedmann, C. Brüne, A. Roth, H. Buhmann, L. W. Molenkamp, X.-L. Qi, and S.-C. Zhang, "Quantum Spin Hall Insulator State in HgTe Quantum Wells," Science **318**, 766–770 (2007).

[24] P. Wadley, B. Howells, J. Železný, C. Andrews, V. Hills, R. P. Campion, V. Novák, K. Olejník, F. Maccherozzi, S. S. Dhesi, S. Y. Martin, T. Wagner, J. Wunderlich, F. Freimuth, Y. Mokrousov, J. Kuneš, J. S. Chauhan, M. J. Grzybowski, A. W. Rushforth, K. W. Edmonds, B. L. Gallagher, and T. Jungwirth, "Electrical switching of an antiferromagnet," Science **351**, 587–590 (2016).

[25] A. V. Chumak, V. I. Vasyuchka, A. A. Serga, and B. Hillebrands, "Magnon spintronics," Nature Physics **11**, 453–461 (2015).

[26] C. Gong and X. Zhang, "Two-dimensional magnetic crystals and emergent heterostructure devices," Science **363**, eaav4450 (2019).

[27] Y. Deng, Y. Yu, M. Z. Shi, Z. Guo, Z. Xu, J. Wang, X. H. Chen, and Y. Zhang, "Quantum anomalous Hall effect in intrinsic magnetic topological insulator MnBi2Te4," Science **367**, 895–900 (2020).

[28] L. Šmejkal, J. Sinova, and T. Jungwirth, "Emerging Research Landscape of Altermagnetism," Physical Review X **12**, 040501 (2022).

[29] L. Šmejkal, J. Sinova, and T. Jungwirth, "Beyond Conventional Ferromagnetism and Antiferromagnetism: A Phase with Nonrelativistic Spin and Crystal Rotation Symmetry," Physical Review X **12**, 031042 (2022).

[30] R. F. Wang, C. Nisoli, R. S. Freitas, J. Li, W. McConville, B. J. Cooley, M. S. Lund, N. Samarth, C. Leighton, V. H. Crespi, and P. Schiffer, "Artificial 'spin ice' in a geometrically frustrated lattice of nanoscale ferromagnetic islands," Nature **439**, 303–306 (2006).

[31] W. R. Branford, S. Ladak, D. E. Read, K. Zeissler, and L. F. Cohen, "Emerging Chirality in Artificial Spin Ice," Science **335**, 1597–1600 (2012).

[32] S. H. Skjærvø, C. H. Marrows, R. L. Stamps, and L. J. Heyderman, "Advances in artificial spin ice," Nature Reviews Physics **2**, 13–28 (2020).

[33] J. H. Jensen, E. Folven, and G. Tufte, "Computation in artificial spin ice," in ALIFE 2018: The 2018 Conference on Artificial Life (2018), pp. 15–22.

[34] J. C. Gartside, K. D. Stenning, A. Vanstone, H. H. Holder, D. M. Arroo, T. Dion, F. Caravelli, H. Kurebayashi, and W. R. Branford, "Reconfigurable training and reservoir computing in an artificial spin-vortex ice via spin-wave fingerprinting," Nature Nanotechnology **17**, 460–469 (2022).

[35] W. Hu, Z. Zhang, Y. Liao, Q. Li, Y. Shi, H. Zhang, X. Zhang, C. Niu, Y. Wu, W. Yu, X. Zhou, H. Guo, W. Wang, J. Xiao, L. Yin, Q. Liu, and J. Shen, "Distinguishing artificial spin ice states using magnetoresistance effect for neuromorphic computing," Nature Communications **14**, 2562 (2023).

[36] European Commission. Joint Research Centre, *Energy consumption in data centres and broadband communication networks in the EU*. 1st ed. (Publications Office, LU, 2024).

[37] E. Masanet, A. Shehabi, N. Lei, S. Smith, and J. Koomey, "Recalibrating global data center energy-use estimates," Science **367**, 984–986 (2020).

[38] A. S. Luccioni, Y. Jernite, and E. Strubell, *Power Hungry Processing: Watts Driving the Cost of AI Deployment?* (Nov. 28, 2023) arXiv:2311.16863 [cs], http://arxiv.org/abs/2311.16863 (visited on 04/03/2024), preprint.

[39] R. Landauer, "Irreversibility and Heat Generation in the Computing Process," IBM Journal of Research and Development **5**, 183–191 (1961).

[40] T. Sagawa and M. Ueda, "Second Law of Thermodynamics with Discrete Quantum Feedback Control," Physical Review Letters **100**, 080403 (2008).

[41] A. Bérut, A. Arakelyan, A. Petrosyan, S. Ciliberto, R. Dillenschneider, and E. Lutz, "Experimental verification of Landauer's principle linking information and thermodynamics," Nature **483**, 187–189 (2012).

[42] B. Lambson, D. Carlton, and J. Bokor, "Exploring the Thermodynamic Limits of Computation in Integrated Systems: Magnetic Memory, Nanomagnetic Logic, and the Landauer Limit," Physical Review Letters **107**, 010604 (2011).

[43] Epoch, *Parameter, compute and data trends in machine learning*, (Mar. 25, 2024) https://epochai.org/data/epochdb/visualization (visited on 03/25/2024).

[44] C. Giattino, E. Mathieu, V. Samborska, and M. Roser, "Artificial intelligence," Our World in Data (2023).

[45] R. Sutton, *The bitter lesson*, Incomplete Ideas (blog), (Mar. 13, 2019) http://www.incompleteideas.net/IncIdeas/BitterLesson.html (visited on 03/27/2024).

[46] J. H. Jensen, "Reservoir computing in-materio: Emergence and control in unstructured and structured materials," Doctoral thesis (NTNU, 2021), ISBN: 9788232651634.

[47] Y. Sandamirskaya, M. Kaboli, J. Conradt, and T. Celikel, "Neuromorphic computing hardware and neural architectures for robotics," Science Robotics **7**, eabl8419 (2022).

[48] P. E. Ross, "Why CPU Frequency Stalled," IEEE Spectrum **45**, 72–72 (2008).

[49] M. Hobbhahn and T. Besiroglu, *Trends in GPU price-performance*, (June 27, 2022) `https://epochai.org/blog/trends-in-gpu-price-performance` (visited on 03/25/2024).

[50] S. Blundell, *Magnetism in Condensed Matter* (OUP Oxford, Oct. 5, 2001), 251 pp., ISBN: 978-0-19-158664-4.

[51] J. M. D. Coey, *Magnetism and Magnetic Materials* (Cambridge University Press, Mar. 25, 2010), 632 pp., ISBN: 978-1-139-48692-7.

[52] C. Kittel, "Theory of the structure of ferromagnetic domains in films and small particles," Physical Review **70**, 965–971 (1946), pmid: `15003161`.

[53] C. Chappert, H. Bernas, J. Ferre, V. Kottler, J. Jamet, Y. Chen, E. Cambril, T. Devolder, F. Rousseaux, V. Mathet, and H. Launois, "Planar patterned magnetic media obtained by ion irradiation," Science (New York, N.Y.) **280**, 1919–1922 (1998), pmid: `9632386`.

[54] R. P. Cowburn, D. K. Koltsov, A. O. Adeyeye, M. E. Welland, and D. M. Tricker, "Single-Domain Circular Nanomagnets," Physical Review Letters **83**, 1042–1045 (1999).

[55] R. Skomski, "Nanomagnetics," Journal of Physics: Condensed Matter **15**, R841 (2003).

[56] A. Hubert and R. Schäfer, "Domain Theory," in *Magnetic Domains: The Analysis of Magnetic Microstructures*, edited by A. Hubert and R. Schäfer (Springer, Berlin, Heidelberg, 1998), pp. 99–335, ISBN: 978-3-540-85054-0.

[57] J. Gadbois and J.-G. Zhu, "Effect of edge roughness in nano-scale magnetic bar switching," IEEE Transactions on Magnetics **31**, 3802–3804 (1995).

[58] E. C. Stoner and E. P. Wohlfarth, "A mechanism of magnetic hysteresis in heterogeneous alloys," Philosophical Transactions of the Royal Society of London. Series A, Mathematical and Physical Sciences **240**, 599–642 (1948).

[59] A. Thiaville, "Extensions of the geometric solution of the two dimensional coherent magnetization rotation model," Journal of Magnetism and Magnetic Materials **182**, 5–18 (1998).

[60] C. Nisoli, R. Moessner, and P. Schiffer, "*Colloquium* : artificial spin ice: designing and imaging magnetic frustration," Reviews of Modern Physics **85**, 1473–1490 (2013).

[61] L. J. Heyderman and R. L. Stamps, "Artificial ferroic systems: novel functionality from structure, interactions and dynamics," Journal of Physics Condensed Matter **25**, `10.1088/0953-8984/25/36/363201` (2013).

[62] J. Cumings, L. J. Heyderman, C. H. Marrows, and R. L. Stamps, "Focus on artificial frustrated systems," New Journal of Physics **16**, 075016 (2014).

[63] M. J. Harris, S. T. Bramwell, D. F. McMorrow, T. Zeiske, and K. W. Godfrey, "Geometrical Frustration in the Ferromagnetic Pyrochlore Ho2Ti2O7," Physical Review Letters **79**, 2554–2557 (1997).

[64] L. Pauling, "The Structure and Entropy of Ice and of Other Crystals with Some Randomness of Atomic Arrangement," Journal of the American Chemical Society **57**, 2680–2684 (1935).

[65] D. R. Hamann, "H2O hydrogen bonding in density-functional theory," Physical Review B **55**, R10157–R10160 (1997).

[66] A. P. Ramirez, A. Hayashi, R. J. Cava, R. Siddharthan, and B. S. Shastry, "Zero-point entropy in 'spin ice'," Nature **399**, 333–335 (1999).

[67] Y. Qi, T. Brintlinger, and J. Cumings, "Direct observation of the ice rule in an artificial kagome spin ice," Physical Review B **77**, 094418 (2008).

[68] S. Ladak, D. E. Read, G. K. Perkins, L. F. Cohen, and W. R. Branford, "Direct observation of magnetic monopole defects in an artificial spin-ice system," Nature Physics **6**, 359–363 (2010).

[69] S. Ladak, D. E. Read, W. R. Branford, and L. F. Cohen, "Direct observation and control of magnetic monopole defects in an artificial spin-ice material," New Journal of Physics **13**, 063032 (2011).

[70] A. Farhan, P. M. Derlet, A. Kleibert, A. Balan, R. V. Chopdekar, M. Wyss, J. Perron, A. Scholl, F. Nolting, and L. J. Heyderman, "Direct Observation of Thermal Relaxation in Artificial Spin Ice," Physical Review Letters **111**, 057204 (2013).

[71] C. H. Marrows, "Experimental Studies of Artificial Spin Ice," in *Spin Ice*, edited by M. Udagawa and L. Jaubert (Springer International Publishing, Cham, 2021), pp. 455–478, ISBN: 978-3-030-70860-3.

[72] G.-W. Chern, "Artificial Spin Ice: Beyond Pyrochlores and Magnetism," in *Spin Ice*, edited by M. Udagawa and L. Jaubert (Springer International Publishing, Cham, 2021), pp. 419–453, ISBN: 978-3-030-70860-3.

[73] S. Gliga, E. Iacocca, and O. G. Heinonen, "Dynamics of reconfigurable artificial spin ice: Toward magnonic functional materials," APL Materials **8**, 040911 (2020).

[74] E. Mengotti, L. J. Heyderman, A. F. Rodríguez, F. Nolting, R. V. Hügli, and H.-B. Braun, "Real-space observation of emergent magnetic monopoles and associated dirac strings in artificial kagome spin ice," Nature Physics **7**, 68–74 (2011).

[75] S. Zhang, I. Gilbert, C. Nisoli, G. W. Chern, M. J. Erickson, L. O'Brien, C. Leighton, P. E. Lammert, V. H. Crespi, and P. Schiffer, "Crystallites of magnetic charges in artificial spin ice," Nature **500**, 553–557 (2013).

[76] E. Mengotti, L. J. Heyderman, A. Fraile Rodríguez, A. Bisig, L. Le Guyader, F. Nolting, and H. B. Braun, "Building blocks of an artificial kagome spin ice: Photoemission electron microscopy of arrays of ferromagnetic islands," Physical Review B **78**, 144402 (2008).

[77] N. Rougemaille, F. Montaigne, B. Canals, A. Duluard, D. Lacour, M. Hehn, R. Belkhou, O. Fruchart, S. El Moussaoui, A. Bendounan, and F. Maccherozzi, "Artificial Kagome Arrays of Nanomagnets: A Frozen Dipolar Spin Ice," Physical Review Letters **106**, 057209 (2011).

[78] V. Kapaklis, U. B. Arnalds, A. Harman-Clarke, E. T. Papaioannou, M. Karimipour, P. Korelis, A. Taroni, P. C. W. Holdsworth, S. T. Bramwell, and B. Hjörvarsson, "Melting artificial spin ice," New Journal of Physics **14**, 035009 (2012).

[79] G. Möller and R. Moessner, "Artificial square ice and related dipolar nanoarrays," Physical Review Letters **96**, 237202 (2006).

[80] C. Castelnovo, R. Moessner, and S. L. Sondhi, "Magnetic monopoles in spin ice," Nature **451**, 42–45 (2008).

[81] Z. Budrikis, P. Politi, and R. L. Stamps, "A network model for field and quenched disorder effects in artificial spin ice," New Journal of Physics **14**, 045008 (2012).

[82] R. C. Silva, F. S. Nascimento, L. A. S. Mól, W. A. Moura-Melo, and A. R. Pereira, "Thermodynamics of elementary excitations in artificial magnetic square ice," New Journal of Physics **14**, 015008 (2012).

[83] D. Levis, L. F. Cugliandolo, L. Foini, and M. Tarzia, "Thermal Phase Transitions in Artificial Spin Ice," Physical Review Letters **110**, 207206 (2013).

[84] M. Saccone, F. Caravelli, K. Hofhuis, S. Dhuey, A. Scholl, C. Nisoli, and A. Farhan, "Real-space observation of ergodicity transitions in artificial spin ice," Nature Communications **14**, 5674 (2023).

[85] V. S. Bhat, B. Farmer, N. Smith, E. Teipel, J. Woods, J. Sklenar, J. B. Ketterson, J. T. Hastings, and L. E. De Long, "Non-stochastic switching and emergence of magnetic vortices in artificial quasicrystal spin ice," Physica C: Superconductivity and its Applications **503**, 170–174 (2014).

[86] B. Farmer, V. S. Bhat, J. Sklenar, J. Woods, E. Teipel, N. Smith, J. B. Ketterson, J. T. Hastings, and L. E. De Long, "Nonstochastic magnetic reversal in artificial quasicrystalline spin ice," Journal of Applied Physics **115**, 17E133 (2014).

[87] D. Smith, J. S. Myers, C. S. Kaplan, and C. Goodman-Strauss, *An aperiodic monotile*, (May 29, 2023) arXiv:2303.10798 [cs, math], http://arxiv.org/abs/2303.10798 (visited on 04/01/2024), preprint.

[88] A. Penty and G. Tufte, "A Representation of Artificial Spin Ice for Evolutionary Search," in ALIFE 2021: The 2021 Conference on Artificial Life (July 19, 2021).

[89] A. Penty and G. Tufte, "Evolving Artificial Spin Ice for Robust Computation.," International Journal of Unconventional Computing **18** (2023).

[90] K. Hon, Y. Kuwabiraki, M. Goto, R. Nakatani, Y. Suzuki, and H. Nomura, "Numerical simulation of artificial spin ice for reservoir computing," Applied Physics Express **14**, 033001 (2021).

[91] G. Csaba, A. Imre, G. Bernstein, W. Porod, and V. Metlushko, "Nanocomputing by field-coupled nanomagnets," IEEE Transactions on Nanotechnology **1**, 209–213 (2002).

[92] Z. Guo, J. Yin, Y. Bai, D. Zhu, K. Shi, G. Wang, K. Cao, and W. Zhao, "Spintronics for Energy- Efficient Computing: An Overview and Outlook," Proceedings of the IEEE **109**, 1398–1417 (2021).

[93] L. D. Landau and E. M. Lifshitz, *Fluid Mechanics: Landau and Lifshitz: Course of Theoretical Physics, Volume 6* (Elsevier, Sept. 3, 2013), 556 pp., ISBN: 978-1-4831-6104-4.

[94] W. F. Brown (Jr.), *Micromagnetics* (Interscience Publishers, 1963), 143 pp.

[95] J. Fidler and T. Schrefl, "Micromagnetic modelling - the current state of the art," Journal of Physics D: Applied Physics **33**, R135–R156 (2000).

[96] L. D. Landau, E. M. Lifšic, L. P. Pitaevskij, and L. D. Landau, *Statistical physics. 2: Theory of the condensed state / by E. M. Lifshitz and L. P. Pitaevskii*, Repr, Course of Theoretical Physics / L. D. Landau and E. M. Lifshitz 9 (Elsevier Butterworth-Heinemann, Oxford Burlington, MA, 2006), 387 pp., ISBN: 978-0-7506-2636-1.

[97] M. Donahue, *OOMMF user's guide, version 1.0*, - 6376, National Institute of Standards and Technology, Gaithersburg, MD, 1999.

[98] A. Vansteenkiste, J. Leliaert, M. Dvornik, M. Helsen, F. Garcia-Sanchez, and B. Van Waeyenberge, "The design and verification of MuMax3," AIP Advances **4**, 107133 (2014).

[99] J. Leliaert, M. Dvornik, J. Mulkers, J. D. Clercq, M. V. Milošević, and B. V. Waeyenberge, "Fast micromagnetic simulations on GPU—recent advances made with mumax3," Journal of Physics D: Applied Physics **51**, 123002 (2018).

[100] S. Zhang and Z. Li, "Roles of Nonequilibrium Conduction Electrons on the Magnetization Dynamics of Ferromagnets," Physical Review Letters **93**, 127204 (2004).

[101] A. N. Bogdanov and U. K. Rößler, "Chiral Symmetry Breaking in Magnetic Thin Films and Multilayers," Physical Review Letters **87**, 037203 (2001).

[102] M. Darby and E. Isaac, "Magnetocrystalline anisotropy of ferro- and ferrimagnetics," IEEE Transactions on Magnetics **10**, 259–304 (1974).

[103] W. F. Brown Jr., "Thermal Fluctuations of a Single-Domain Particle," Journal of Applied Physics **34**, 1319–1320 (1963).

[104] L. D. Landau and E. M. Lifshitz, "On the theory of the dispersion of magnetic permeability in ferromagnetic bodies. reproduced in collected papers of ld landau," Pergamon, New York (1935).

[105] T. L. Gilbert, "A Lagrangian formulation of the gyromagnetic equation of the magnetization field," Physical Review **100**, 1243 (1955).

[106] A. M. Mathai and T. A. Davis, "Constructing the sunflower head," Mathematical Biosciences **20**, 117–133 (1974).

[107] Z. Budrikis, "Athermal dynamics of artificial spin ice: disorder, edge and field protocol effects," Doctoral Thesis (2012).

[108] X. Ke, J. Li, C. Nisoli, P. E. Lammert, W. McConville, R. F. Wang, V. H. Crespi, and P. Schiffer, "Energy Minimization and ac Demagnetization in a Nanomagnet Array," Physical Review Letters **101**, 037205 (2008).

[109] A. B. Bortz, M. H. Kalos, and J. L. Lebowitz, "A new algorithm for Monte Carlo simulation of Ising spin systems," Journal of Computational Physics **17**, 10–18 (1975).

[110] P. E. Lammert, V. H. Crespi, and C. Nisoli, "Gibbsianizing nonequilibrium dynamics of artificial spin ice and other spin systems," New Journal of Physics **14**, 045009 (2012).

[111] A. F. Voter, F. Montalenti, and T. C. Germann, "Extending the Time Scale in Atomistic Simulation of Materials," Annual Review of Materials Research **32**, 321–346 (2002).

[112] A. Farhan, P. M. Derlet, A. Kleibert, A. Balan, R. V. Chopdekar, M. Wyss, L. Anghinolfi, F. Nolting, and L. J. Heyderman, "Exploring hyper-cubic energy landscapes in thermally active finite artificial spin-ice systems," Nature Physics **9**, 375–382 (2013).

[113] D. Thonig, S. Reißaus, I. Mertig, and J. Henk, "Thermal string excitations in artificial spin-ice square dipolar arrays," Journal of Physics: Condensed Matter **26**, 266006 (2014).

[114] Y. Bar-Yam, *The dynamics of complex systems* (1997), ISBN: 0-201-55748-7.

[115] K. Yamazaki and H. Namatsu, "5-nm-Order Electron-Beam Lithography for Nanodevice Fabrication," Japanese Journal of Applied Physics **43**, 3767 (2004).

[116] Z. Cui, "Nanofabrication by Charged Beams," in *Nanofabrication: Principles, Capabilities and Limits*, edited by Z. Cui (Springer US, Boston, MA, 2008), pp. 77–127, ISBN: 978-0-387-75577-9.

[117] K. Murata, T. Matsukawa, and R. Shimizu, "Monte Carlo Calculations on Electron Scattering in a Solid Target," Japanese Journal of Applied Physics **10**, 678 (1971).

[118] S. Okazaki, "High resolution optical lithography or high throughput electron beam lithography: The technical struggle from the micro to the nano-fabrication evolution," Microelectronic Engineering **133**, 23–35 (2015).

[119] B. Thole, G. Van Der Laan, and G. Sawatzky, "Strong Magnetic Dichroism Predicted in the M4,5 X-Ray Absorption Spectra of Magnetic Rare-Earth Materials," Physical Review Letters **55**, 2086–2088 (1985).

[120] G. van der Laan, B. Thole, G. Sawatzky, J. Goedkoop, J. Fuggle, J.-M. Esteva, R. Karnatak, J. Remeika, and H. Dabkowska, "Experimental proof of magnetic x-ray dichroism," Physical Review B **34**, 6529–6531 (1986).

[121] G. van der Laan and A. I. Figueroa, "X-ray magnetic circular dichroism—A versatile tool to study magnetism," Coordination Chemistry Reviews, Following Chemical Structures Using Synchrotron Radiation **277–278**, 95–129 (2014).

[122] A. Balerna and S. Mobilio, "Introduction to Synchrotron Radiation," in *Synchrotron Radiation: Basics, Methods and Applications*, edited by S. Mobilio, F. Boscherini, and C. Meneghini (Springer, Berlin, Heidelberg, 2015), pp. 3–28, ISBN: 978-3-642-55315-8.

[123] P. Sedigh Rahimabadi, M. Khodaei, and K. R. Koswattage, "Review on applications of synchrotron-based X-ray techniques in materials characterization," X-Ray Spectrometry **49**, 348–373 (2020).

[124] S. Mobilio, F. Boscherini, and C. Meneghini, *Synchrotron radiation: basics, methods and applications* (Springer, Heidelberg, 2015), ISBN: 978-3-642-55315-8.

[125] D. Nolle, M. Weigand, G. Schütz, and E. Goering, "High Contrast Magnetic and Nonmagnetic Sample Current Microscopy for Bulk and Transparent Samples Using Soft X-Rays," Microscopy and Microanalysis **17**, 834–842 (2011).

[126] J. Gräfe, F. Haering, T. Tietze, P. Audehm, M. Weigand, U. Wiedwald, P. Ziemann, P. Gawroński, G. Schütz, and E. J. Goering, "Perpendicular magnetisation from in-plane fields in nano-scaled antidot lattices," Nanotechnology **26**, 225203 (2015).

[127] S. A. Morley, A. Stein, M. C. Rosamond, D. A. Venero, A. Hrabec, P. M. Shepley, M.-Y. Im, P. Fischer, M. T. Bryan, D. A. Allwood, P. Steadman, S. Langridge, and C. H. Marrows, "Temperature and magnetic-field driven dynamics in artificial magnetic square ice," in Spintronics VIII, Vol. 9551 (Sept. 8, 2015), pp. 69–80.

[128] E. Digernes, J. Leliaert, M. Weigand, E. Folven, and B. Van Waeyenberge, "Direct observation of temperature dependent vortex dynamics in a La0.7Sr0.3MnO3 micromagnet," Physical Review Research **2**, 043429 (2020).

[129] P. Pip, S. Treves, J. R. Massey, S. Finizio, Z. Luo, A. Hrabec, V. Scagnoli, J. Raabe, L. Philippe, L. J. Heyderman, and C. Donnelly, "X-ray imaging of the magnetic configuration of a three-dimensional artificial spin ice building block," APL Materials **10**, 101101 (2022).

[130] P. Schattschneider, S. Rubino, and C. Hébert, "Circular Dichroism in the Transmission Electron Microscope," in *Reference Module in Materials Science and Materials Engineering* (Elsevier, Jan. 1, 2016), ISBN: 978-0-12-803581-8.

[131] A. Einstein, "On a heuristic point of view about the creation and conversion of light," Annalen der Physik **17**, 132–148 (1905).

[132] J. Feng and A. Scholl, "Photoemission Electron Microscopy," in *Springer Handbook of Microscopy*, edited by P. W. Hawkes and J. C. H. Spence (Springer International Publishing, Cham, 2019), pp. 537–564, ISBN: 978-3-030-00069-1.

[133] S. Berg, D. Kutra, T. Kroeger, C. N. Straehle, B. X. Kausler, C. Haubold, M. Schiegg, J. Ales, T. Beier, M. Rudy, K. Eren, J. I. Cervantes, B. Xu, F. Beuttenmueller, A. Wolny, C. Zhang, U. Koethe, F. A. Hamprecht, and A. Kreshuk, "Ilastik: interactive machine learning for (bio)image analysis," Nature Methods **16**, 1226–1232 (2019).

[134] L. Néel, "Théorie du traînage magnétique des ferromagnétiques en grains fins avec application aux terres cuites," Annales de géophysique **5**, 99–136 (1949).

[135] Y. Li, G. W. Paterson, G. M. Macauley, F. S. Nascimento, C. Ferguson, S. A. Morley, M. C. Rosamond, E. H. Linfield, D. A. MacLaren, R. Macêdo, C. H. Marrows, S. McVitie, and R. L. Stamps, "Superferromagnetism and domain-wall topologies in artificial "Pinwheel" spin ice," ACS Nano **13**, 2213–2222 (2019).

[136] G. W. Paterson, G. M. Macauley, and R. Macêdo, "Field-driven reversal models in artificial spin ice," Mar. 26, 2021, arXiv:2103.14643.

[137] A. Penty and G. Tufte, "Evolving Music from a Self-Organising Nanomagnetic Orchestra," in ALIFE 2023: Ghost in the Machine: Proceedings of the 2023 Artificial Life Conference (July 24, 2023).

[138] I. A. Chioar, B. Canals, D. Lacour, M. Hehn, B. Santos Burgos, T. O. Menteş, A. Locatelli, F. Montaigne, and N. Rougemaille, "Kinetic pathways to the magnetic charge crystal in artificial dipolar spin ice," Physical Review B **90**, 220407 (2014).

[139] J. M. Porro, S. A. Morley, D. A. Venero, R. Macêdo, M. C. Rosamond, E. H. Linfield, R. L. Stamps, C. H. Marrows, and S. Langridge, "Magnetization dynamics of weakly interacting sub-100 nm square artificial spin ices," Scientific Reports **9**, 19967 (2019).

[140] G. Brown, M. A. Novotny, and P. A. Rikvold, "Micromagnetic simulations of thermally activated magnetization reversal of nanoscale magnets," Journal of Applied Physics **87**, 4792–4794 (2000).

[141] T. S. van Erp and P. G. Bolhuis, "Elaborating transition interface sampling methods," Journal of Computational Physics **205**, 157–181 (2005).

[142] S. Gliga, G. Hrkac, C. Donnelly, J. Büchi, A. Kleibert, J. Cui, A. Farhan, E. Kirk, R. V. Chopdekar, Y. Masaki, N. S. Bingham, A. Scholl, R. L. Stamps, and L. J. Heyderman, "Emergent dynamic chirality in a thermally driven artificial spin ratchet," Nature Materials **16**, 1106–1111 (2017).

[143] A. N. McCaughan, A. N. Tait, S. M. Buckley, D. M. Oh, J. T. Chiles, J. M. Shainline, and S. W. Nam, "PHIDL: Python-based layout and geometry creation for nanolithography," Journal of Vacuum Science & Technology B **39**, 062601 (2021).

[144] E. S. Digernes, "Patterned nanomagnets - magnetic metamaterials and vortex dynamics," Doctoral thesis (NTNU, 2021), ISBN: 9788232660650.

[145] Z. Budrikis, P. Politi, and R. L. Stamps, "Disorder regimes and equivalence of disorder types in artificial spin ice," Journal of Applied Physics **111**, 07E109 (2012).

[146] G. W. Paterson, G. M. Macauley, Y. Li, R. Macêdo, C. Ferguson, S. A. Morley, M. C. Rosamond, E. H. Linfield, C. H. Marrows, R. L. Stamps, and S. McVitie, "Heisenberg pseudo-exchange and emergent anisotropies in field-driven pinwheel artificial spin ice," Physical Review B **100**, 174410 (2019).

[147] S. D. Slöetjes, B. Hjörvarsson, and V. Kapaklis, "Texture fluctuations and emergent dynamics in coupled nanomagnets," Physical Review B **106**, 104405 (2022).

[148] Y.-L. Wang, Z.-L. Xiao, A. Snezhko, J. Xu, L. E. Ocola, R. Divan, J. E. Pearson, G. W. Crabtree, and W.-K. Kwok, "Rewritable artificial magnetic charge ice," Science **352**, 962–966 (2016).

[149] J. C. Gartside, D. M. Arroo, D. M. Burn, V. L. Bemmer, A. Moskalenko, L. F. Cohen, and W. R. Branford, "Realization of ground state in artificial kagome spin ice via topological defect-driven magnetic writing," Nature Nanotechnology **13**, 53–58 (2018).

[150] D. M. Burn, M. Chadha, and W. R. Branford, "Dynamic dependence to domain wall propagation through artificial spin ice," Physical Review B **95**, 104417 (2017).

[151] Z. Luo, T. P. Dao, A. Hrabec, J. Vijayakumar, A. Kleibert, M. Baumgartner, E. Kirk, J. Cui, T. Savchenko, G. Krishnaswamy, L. J. Heyderman, and P. Gambardella, "Chirally coupled nanomagnets.," Science (New York, N.Y.) **363**, 1435–1439 (2019), pmid: 30923219.

[152] M. T. Kaffash, S. Lendinez, and M. B. Jungfleisch, "Nanomagnonics with artificial spin ice," Physics Letters A **402**, 127364 (2021).

[153] Z. Budrikis, J. P. Morgan, J. Akerman, A. Stein, P. Politi, S. Langridge, C. H. Marrows, and R. L. Stamps, "Disorder Strength and Field-Driven Ground State Domain Formation in Artificial Spin Ice: Experiment, Simulation, and Theory," Physical Review Letters **109**, 037203 (2012).

# Papers

# flatspin: A large-scale artificial spin ice simulator

Johannes H. Jensen [1,*,†] Anders Strømberg [1,*] Odd Rune Lykkebø [1] Arthur Penty [1] Jonathan Leliaert [2] Magnus Själander [1] Erik Folven [1] and Gunnar Tufte [1]

[1]*Norwegian University of Science and Technology, 7034 Trondheim, Norway*

[2]*Department of Solid State Sciences, Ghent University, 9000 Ghent, Belgium*

(Received 17 February 2020; revised 24 June 2022; accepted 24 June 2022; published 4 August 2022)

We present flatspin, a novel simulator for systems of interacting mesoscopic spins on a lattice, also known as artificial spin ice (ASI). A generalization of the Stoner-Wohlfarth model is introduced, and combined with a well-defined switching protocol to capture realistic ASI dynamics using a point-dipole approximation. Temperature is modelled as an effective thermal field, based on the Arrhenius-Néel equation. Through GPU acceleration, flatspin can simulate the dynamics of millions of magnets within practical time frames, enabling exploration of large-scale emergent phenomena at unprecedented speeds. We demonstrate flatspin's versatility through the reproduction of a diverse set of established experimental results from literature. In particular, the field-driven magnetization reversal of "pinwheel" ASI is reproduced, for the first time, in a dipole model. Finally, we use flatspin to explore aspects of "square" ASI by introducing dilution defects and measuring the effect on the vertex population.

DOI: 10.1103/PhysRevB.106.064408

## I. INTRODUCTION

An artificial spin ice (ASI) is an ensemble of nanomagnets arranged on a lattice, coupled through magnetic dipole-dipole interactions. The vast variety of emergent collective behaviors found in these systems have generated considerable research interest over the last decade [1,2]. Using modern nanofabrication techniques, emergent phenomena can be facilitated through direct control of the ASI geometry, e.g., collective ferromagnetic/antiferromagnetic ordering [3], Dirac strings [4], and phase transitions [5,6]. ASIs offer a unique model system for exploring fundamental physics, since magnetic microscopy enables direct observation of their internal state. There is also a growing interest in ASIs as building blocks for novel devices [7,8]. Computer simulations have proven invaluable to gain insight into the rich behavior of these coupled systems.

Micromagnetic simulations of ASI have been limited to a handful of nanomagnets due to excessive computational cost. Although physically accurate, such high fidelity simulations are unable to capture large-scale emergent phenomena, such as the size of magnetically ordered domains and long-range order. To simulate large ASI systems, an established approach is to sacrifice fidelity for speed by employing a dipole model, i.e., treating each nanomagnet as a single macrospin approximated by a point dipole [9]. Conventionally, Monte Carlo methods have been used in conjunction with the dipole approximation to search for low energy configurations [10,11] or to study statistical measures such as vertex populations [9]. However, Monte Carlo methods do not model the dynamical pathway taking the system from an initial configuration to the final low-energy configuration. They are inherently stochastic and better suited for ensemble statistics rather than dynamics [12].

Here we present flatspin, a point-dipole simulator for large ASI systems that is capable of capturing realistic dynamics, at long time scales. We introduce a generalization of the Stoner-Wohlfarth model, that describes the switching characteristics of numerous nanomagnet shapes. This generalized model is combined with a novel, well-defined, switching protocol, to capture the dynamics of large ASI systems. All influences on the magnets are represented by magnetic fields, including a stochastic thermal field derived from the Arrhenius-Néel equation. These crucial aspects of flatspin, combined with GPU acceleration, extends the possibilities of ASI simulation. Using flatspin in place of micromagnetic simulations increases the possible simulation sizes from hundreds to millions of magnets, enabling exploration of large-scale, emergent phenomena in these intriguing systems.

In this paper, we present the motivation and design of flatspin. The thermal model is verified against established analytical and numerical models. We demonstrate good agreement between flatspin and a variety of published experimental results. We show that flatspin can capture dynamic behaviors observed experimentally, which have previously eluded modeling [13]. Finally, we explore new aspects of square ASI by removing individual elements of the lattice, and measuring the effects on the type population under an applied field.

*These authors contributed equally to this work.

†Corresponding author: johannes.jensen@ntnu.no

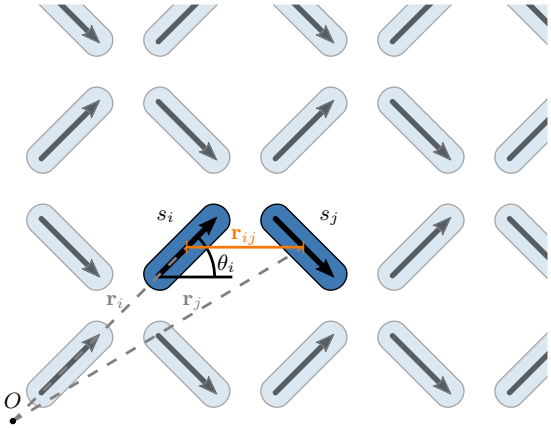


FIG. 1. The representation of nanomagnets as spins $s_i$ and associated quantities: position $\mathbf{r}_i$, angle $\theta_i$, and distance to neighbor $j$, $\mathbf{r}_{ij}$. Note that the magnetization of spin $i$ is given by its spin $s_i$, and orientation $\theta_i$.

## II. THE FLATSPIN MAGNETIC MODEL

In this section, we describe the dipole model and the underlying physical assumptions of flatspin. The model is designed to simulate the ensemble state-by-state evolution, i.e., *dynamics*, of two-dimensional ASI. In short, magnets are modeled as point dipoles (Sec. II A), and each dipole can be affected by three types of external influence: magnetic dipole-dipole coupling (Sec. II C), an applied external magnetic field (Sec. II D), and thermal fluctuations (Sec. II E). The switching of spins is determined using a generalized Stoner-Wohlfarth model, which takes the shape anisotropy of the simulated nanoislands into account (Sec. II F). Imperfections in the ASI are introduced as different coercive fields, set per spin (Sec. II G). Dynamics are modeled using a deterministic single spin flip strategy (Sec. II H).

### A. Magnets as dipoles

ASI systems are physically realized as elongated islands of a ferromagnetic material, arranged on a two-dimensional lattice. The magnets are made small enough to exhibit a single ferromagnetic domain, i.e., coherent magnetization throughout the magnet. The single domain state is stable as the energy cost associated with domain walls exceeds the cost associated with the demagnetization energy [14,15]. Since a magnet has coherent magnetization, it can be approximated by a single mesoscopic spin and the magnetic state can be represented by a single vector $\mathbf{m}$.

The shape anisotropy of the thin elongated islands will restrict their magnetization to two possible in-plane directions. Hence, individual magnets can be approximated by classical macrospins with a twofold degenerate ground state defined by the elongated shape of the individual elements. Due to the two degenerate ground-state configurations, we approximate each magnet as a magnetic dipole with *binary* magnetization, i.e., a binary macrospin, $s_i \in \{-1, +1\}$.

As illustrated in Fig. 1, each magnetic dipole is modelled with a position $\mathbf{r}_i$ and rotation $\theta_i$, which together define the ASI geometry. Furthermore, each magnet is assigned a coercive field, $h_c^{(i)}$, describing its resistance to switching (see Sec. II F). Using reduced units, the magnetization vector of a single magnet can be expressed as

$$\mathbf{m}_i = s_i \hat{\mathbf{m}}_i \tag{1}$$

where $\hat{\mathbf{m}}_i = [\cos\theta_i, \sin\theta_i]$ is the unit vector along $\mathbf{m}_i$.

### B. Magnetic fields and temperature

External fields and temperature are modeled as a combination of effective magnetic fields. The total field $\mathbf{h}_i$ affecting each magnet $i$ is the sum of three components:

$$\mathbf{h}_i = \mathbf{h}_{\text{dip}}^{(i)} + \mathbf{h}_{\text{ext}}^{(i)} + \mathbf{h}_{\text{th}}^{(i)}, \tag{2}$$

where $\mathbf{h}_{\text{dip}}^{(i)}$ is the local magnetic field from neighboring magnets (magnetic dipole-dipole interactions), $\mathbf{h}_{\text{ext}}^{(i)}$ is a global or local external field, and $\mathbf{h}_{\text{th}}^{(i)}$ is a stochastic magnetic field representing thermal fluctuations in each magnetic element. Each of these field contributions are described in the following sections.

### C. Magnetic dipole-dipole interactions

The individual magnets, or spins, are coupled solely through dipole-dipole interactions. Each spin $i$ is subject to a magnetic field from all neighboring spins, $j \neq i$, given by

$$\mathbf{h}_{\text{dip}}^{(i)} = \alpha \sum_{j \neq i} \frac{3\mathbf{r}_{ij}(\mathbf{m}_j \cdot \mathbf{r}_{ij})}{|\mathbf{r}_{ij}|^5} - \frac{\mathbf{m}_j}{|\mathbf{r}_{ij}|^3}, \tag{3}$$

where $\mathbf{r}_{ij} = \mathbf{r}_i - \mathbf{r}_j$ is the distance vector from spin $i$ to $j$, and $\alpha$ scales the dipolar coupling strength between spins. The coupling strength $\alpha$ is given by $\alpha = \frac{\mu_0 M}{4\pi a^3}$, where $a$ is the lattice spacing, $M$ is the net magnetic moment of a single magnet, and $\mu_0$ is the vacuum permeability. The distance $\mathbf{r}_{ij}$ is thus given in reduced units of the lattice spacing.

The dipole field present at each spin's location is calculated by summing the dipole field contributions from spins in its neighborhood. The size of the neighborhood is user configurable and defined in units of the lattice spacing. The required neighborhood distance varies, subject to the system of study. Care must be taken to include enough spins in the neighborhood such that the observed behavior converges, especially when considering systems exhibiting long-range effects. In some geometries, such as square ASI, short range interactions dominate the contributions to $\mathbf{h}_{\text{dip}}$ [16,17], in which case the neighborhood size can be relatively small, for a benefit of increased efficiency. For geometries where long range interactions are significant, a larger neighborhood is required, e.g., pinwheel ASI [18]. The flatspin documentation [19] provides an example of how to choose an appropriate neighborhood distance.

### D. External field

Applying an external magnetic field is the primary mechanism for altering the state of an ASI in a controlled manner. The external field can either be set locally on a per-spin basis

($\mathbf{h}_{\text{ext}}^{(i)}$), globally for the entire system ($\mathbf{h}_{\text{ext}}$), or as a spatial vector field ($\mathbf{h}_{\text{ext}}(\mathbf{r})$).

Time-dependent external fields are supported, i.e., $\mathbf{h}_{\text{ext}}$ is a discrete time series of either local, global, or spatial fields. A variety of time-dependent external fields come predefined with flatspin, including sinusoidal, sawtooth, and rotational fields. More complex field protocols can be generated, e.g., for annealing purposes or probing dynamic response.

### E. Thermal field

In flatspin, the thermal energy fluctuations of individual magnets $E_{\text{th}}^{(i)}$ are represented by a corresponding stochastic magnetic field $\mathbf{h}_{\text{th}}^{(i)}$. The following section describes how the thermal field magnitude is derived.

In a physical ensemble of particles, there is a thermal energy budget, on the scale of $k_{\text{B}}T$, where $k_{\text{B}}$ and $T$ denote the Boltzmann constant and the temperature, respectively. For bistable magnetic particles, the thermal energy causes random switching events, at a characteristic rate given by the Arrhenius-Néel equation [20],

$$f = f_0 \exp\left(-\frac{\Delta E}{k_{\text{B}}T}\right), \tag{4}$$

where $f_0$ is the attempt frequency and $\Delta E$ is the particle's energy barrier for switching.

The energy barrier $\Delta E$ corresponds to the *additional* Zeeman energy required for magnetization reversal. This additional energy is a function of the smallest additional field needed for switching $\Delta h$. The Zeeman energy from $\Delta h$ is given by $\Delta E = \Delta h M_{\text{th}}$, where $M_{\text{th}}$ is the thermal nucleation moment. Note that $M_{\text{th}}$ is typically smaller than the entire magnetic moment $M$, since thermal nanomagnetic switching is generally mediated by a smaller nucleation volume. The relevant criterion for switching is the magnitude of the stochastic thermal field compared to the minimum energy barrier.

The probability of thermal switching follows a Poisson distribution $P_r(k, \Delta t, f)$, where $k$ is the number of switching events in a time interval $\Delta t$, and $f$ is the characteristic switching rate given by Eq. (4). The probability of switching at least once $P_{\text{switch}}$ is given by

$$\begin{aligned} P_{\text{switch}} &= P_r(k > 0), \\ &= 1 - P_r(k = 0), \\ &= 1 - \exp(-f\Delta t), \\ &= 1 - \exp\left(\Delta t f_0 \exp\left(-\frac{\Delta h M_{\text{th}}}{k_{\text{B}}T}\right)\right). \end{aligned} \tag{5}$$

In our model, we use this expression to approximate the probability that a magnet will switch *once*. For this to be valid, $\Delta t$ must be sufficiently small so that multiple switching events are unlikely. In other words, it is assumed that $P_r(k > 1) \ll P_r(k = 1)$, so that magnets do not have time to "switch back" during the time $\Delta t$. This is relevant only for weak bias fields, where the probability of switching is nearly symmetrical. With any significant bias field, the probability of "switching back" will be negligible.

It is important to note that flatspin does not account for the temperature dependence of the material parameters. If these parameters are expected to vary significantly in the temperature range of interest, e.g., $M_{\text{th}}$, this has to be explicitly accounted for by the user.

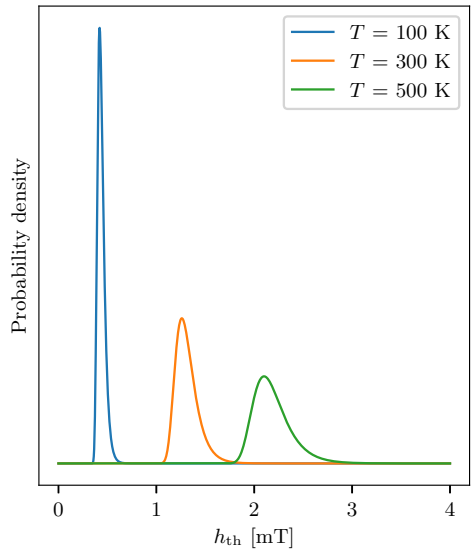


FIG. 2. Probability density functions (PDF) for $h_{\text{th}}$ at different temperatures $T$. The example plots are for a magnetic particle with saturation magnetization $M_{\text{S}} = 860\,\text{kA m}^{-1}$ and volume $V = 220\,\text{nm} \times 80\,\text{nm} \times 3\,\text{nm}$, for a time interval $\Delta t = 1\,\text{ms}$.

As discussed in Sec. II B, all magnetic influences are included as magnetic fields, and their sum is compared to the switching condition to determine whether a magnet switches. Within this framework, we now derive an expression for the thermal field based on $P_{\text{switch}}$.

Consider a stochastic field variable $X$ from which a thermal field $h_{\text{th}}$ is sampled. The probability of drawing a thermal field $h_{\text{th}}$ larger than the minimum switching field $\Delta h$ equals the switching probability for the same minimum switching field,

$$P(X > \Delta h) = P_{\text{switch}}(\Delta h), \tag{6}$$

$$1 - P(X \leqslant \Delta h) = 1 - \exp(-f\Delta t), \tag{7}$$

$$P(X \leqslant \Delta h) = \exp(-f\Delta t). \tag{8}$$

$P(X \leqslant \Delta h)$ is the cumulative density function (CDF) of the distribution for $h_{\text{th}}$ that matches the Poisson distribution in Eq. (5). Using inverse transform sampling, we use the expression for the CDF to transform a uniformly distributed random number $u$ to a thermal magnetic field magnitude $h_{\text{th}}$,

$$h_{\text{th}} = \frac{-k_{\text{B}}T}{M_{\text{th}}} \ln\left(\frac{\ln(u)}{-\Delta t f_0}\right). \tag{9}$$

Figure 2 illustrates how temperature influences the probability density function for the stochastic thermal field. As can be seen, both the expected value and the variance of $h_{\text{th}}$ increases with temperature. In other words, the magnitude and spread of the stochastic field $h_{\text{th}}$ increases, effectively increasing the probability of thermal flips.

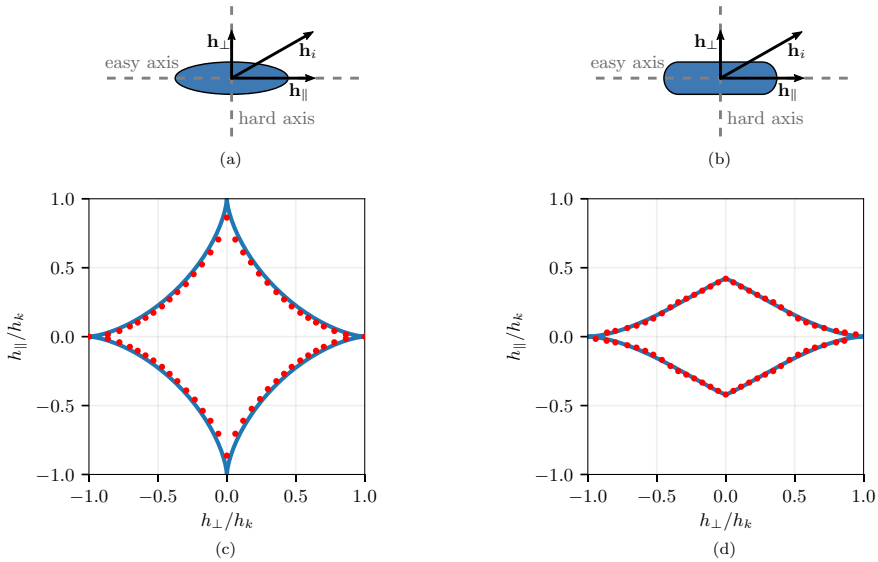


FIG. 3. Top: Schematic showing hard and easy axes of (a) an elliptical magnet and (b) a rectangular stadium-shaped magnet, as well as the total field acting on the magnet $\mathbf{h}_i$ with its parallel and perpendicular components, $\mathbf{h}_\parallel$ and $\mathbf{h}_\perp$, respectively. Bottom: Switching astroid for (c) an elliptical magnet and (d) a rectangular stadium-shaped magnet. Red dots show the coercive field obtained from micromagnetic simulations. The blue line in (c) shows the Stoner-Wohlfarth astroid. The blue line in (d) shows the generalized Stoner-Wohlfarth astroid with parameters $b = 0.42$, $c = 1$, $\beta = 1.7$, and $\gamma = 3.4$ in Eq. (11). The astroids have been normalized with respect to $h_k$.

A stochastic thermal field magnitude drawn from $h_{\text{th}}$ is converted to a vector field $\mathbf{h}_{\text{th}}$ parallel to $\Delta\mathbf{h}$ (the smallest additional field for switching). When the thermal field is added to the sum of fields for each magnet, the probability of switching will follow the Poisson distribution in Eq. (5). In this way, thermal fluctuations are modeled as an additional local field $\mathbf{h}_{\text{th}}^{(i)}$ applied to each magnet individually.

### F. Switching

Magnetization reversal, or *switching*, may take place when a magnet is subjected to a magnetic field or as a result of thermal fluctuations. If the field is sufficiently strong and directed against the magnetization $\mathbf{m}_i$, the magnetization will switch direction.

The critical field strength for switching is referred to as the coercive field $h_c$. For elongated magnets, $h_c$ depends on the angle between the applied field $\mathbf{h}_i$ and $\mathbf{m}_i$. As illustrated in Fig. 3(a), the *easy axis*, where the magnetization favors alignment, lies along the long axis of the magnet, whereas the *hard axis* is perpendicular to the long axis. The external field can be decomposed into two components, $\mathbf{h}_\parallel$ and $\mathbf{h}_\perp$, corresponding to the field component parallel and perpendicular to the easy axis, respectively. We denote the coercive field strength along the hard axis as $h_k$.

A *switching astroid* is a polar plot of $h_c$ at different angles, with $h_\perp$ on the horizontal axis and $h_\parallel$ on the vertical axis. For any applied field $\mathbf{h}_i$ that is outside the switching astroid, the magnet will switch as long as the field is directed against the current magnetization.

Figure 3(c) shows the normalized switching astroid for an elliptical magnet [Fig. 3(a)] as obtained from micromagnetic simulations using MuMax3 [21]. Notice how $h_c$ is the smallest at a 45° angle, indicating that a field directed at 45° to a magnet's principal axes will require the least field strength in order to switch its magnetization.

The Stoner-Wohlfarth (SW) model captures the angle dependent switching characteristic of single-domain elliptical magnets [22]. The characteristic SW astroid is shown in Fig. 3(c) (blue line) and is described by the equation

$$\left(\frac{h_\parallel}{h_k}\right)^{2/3} + \left(\frac{h_\perp}{h_k}\right)^{2/3} = 1. \tag{10}$$

In the SW model, switching may occur when the left-hand side of Eq. (10) is greater than one.

The astroid obtained from micromagnetic simulations and the SW astroid [Fig. 3(c)] are nearly identical. Despite its simplicity, the SW model clearly captures the switching behavior of elliptical nanomagnets.

However, the SW model is only accurate for elliptical magnets. Other magnet shapes typically have quite different switching characteristics. Figure 3(d) shows the switching astroid for rectangular stadium-shaped magnets (red dots), which is the shape commonly used in most fabricated ASIs [Fig. 3(b)]. Notice how the astroid is *asymmetric*: Rectangular magnets switch more easily with a field applied along the easy axis than the hard axis.

To capture the asymmetric switching characteristics of nonelliptical magnets, we have generalized the SW switching model to allow an asymmetry between easy and hard axes. Additionally, the model has been extended to allow for tuning of the curvature of the extrema. In the generalized model, the

switching threshold is given by

$$\left(\frac{h_\parallel}{bh_k}\right)^{2/\gamma} + \left(\frac{h_\perp}{ch_k}\right)^{2/\beta} = 1, \tag{11}$$

where $b$, $c$, $\beta$, and $\gamma$ are parameters, which adjust the shape of the astroid: $b$ and $c$ define the height and width, respectively, while $\beta$ and $\gamma$ adjust the curvature of the astroid at the easy and hard axis, respectively. Introducing these new parameters allows for tuning of the switching astroid to fit with the shape of nanomagnets used in ASIs. With $b = c = 1$ and $\beta = \gamma = 3$, Eq. (11) reduces to Eq. (10), i.e., the classical Stoner-Wohlfarth astroid is obtained (valid for elliptical magnets).

By tuning the parameters of the generalized SW model, we can obtain the asymmetric switching astroid shown in Fig. 3(d) (blue line). The astroid is in good agreement with results obtained from micromagnetic simulations (red dots).

In flatspin, the generalized SW model is used as the switching criteria, i.e., a spin may flip if the left-hand side of Eq. (11) is greater than one. Additionally, the projection of $\mathbf{h}_\mathrm{i}$ onto $\mathbf{m}_i$ must be in the opposite direction of $\mathbf{m}_i$,

$$\mathbf{h}_i \cdot \mathbf{m}_i < 0. \tag{12}$$

### G. Imperfections and disorder

Due to manufacturing imperfections, there will always be a degree of variation in the shape and edge roughness of nanomagnets. This variation can be thought of as a disorder in the magnets' inherent properties. Rough edges and a slightly distorted geometry can affect the magnets' switching mechanisms, with defects pinning magnetization and altering the coercive field for each magnet.

In flatspin we model this variation as disorder in the coercive fields. The coercive field is defined individually for each magnet, and a distribution of values can be used to introduce variation. A user-defined parameter $k_\mathrm{disorder}$ defines the distribution of coercive fields, i.e., $h_k^{(i)}$ is sampled from a normal distribution $\mathcal{N}(h_k, \sigma)$, where $\sigma = k_\mathrm{disorder} \cdot h_k$. Negative $h_k^{(i)}$ values are disallowed.

### H. Dynamics

Given the total magnetic field acting on each spin, $\mathbf{h}_i$, flatspin employs deterministic single spin flip dynamics. At each simulation step, we calculate $\mathbf{h}_i$, which will contain a stochastic term in the case of nonzero temperature. Next, we determine which spins *may* flip according to the switching criteria Eqs. (11) and (12). Finally, we flip the spin where $\mathbf{h}_i$ is the *furthest outside its switching astroid*, i.e., where the left-hand side of Eq. (11) is the greatest. Ties are broken in a deterministic, arbitrary manner, although with nonzero disorder such occurrences are rare. The dipolar fields are recalculated after every spin flip, and the above process is repeated until there are no more flippable spins.

This relaxation process is performed with constant external and thermal fields. To advance the simulation, the fields are updated and relaxation is performed again. Hence, a simulation run consists of a sequence of field updates and relaxation processes.

The dynamical process makes three main assumptions:

(1) The external field is quasistatic compared to the timescale of magnet switching.
(2) Magnet switching is sequential.
(3) The magnet experiencing the highest effective field compared to its switching threshold is the first to switch.

*Assumption 1* means the model holds for low frequency external fields, i.e., where switching settles under a static field. The switching mechanics of nanomagnets are typically in the subnanosecond range [23,24], and experimental setups often employ external magnetic fields, which can be considered static at this timescale. At high applied field frequencies, more complex physical phenomena such as spin waves will have a non-negligible effect on switching dynamics. Such high-frequency phenomena are not considered in flatspin.

*Assumption 2* holds if the coercive fields $h_\mathrm{c}^{(i)}$, and total field $\mathbf{h}_i$, of the magnets are sufficiently nonuniform, so that there will always be a single magnet that will flip first. It is assumed to be unlikely that two magnets will have a $h_\mathrm{c}^{(i)}$ and $\mathbf{h}_i$ that bring them equally far outside the switching astroid. However, in those rare cases where two magnets are equally far outside, overlapping switching events may occur in a physical system.

*Assumption 3* relies on the fact that all changes in the magnetic fields are effectively continuous, and the change is unidirectional within a simulated time step, i.e., a *quasistatic field*. Since evaluation happens in discrete time, there will be cases where several magnets are above their corresponding switching thresholds simultaneously. In those cases, the magnet furthest above its switching threshold will have been the first to have crossed the threshold under a quasistatic field. Furthermore, if the angle of the external field is constant, the switching order is invariant to the time resolution of the external field.

### I. Geometries

The particular spatial arrangement of the magnets is referred to as the *geometry*. A wide range of ASI geometries have been proposed in the literature. Figure 4 depicts the geometries included in flatspin, which are the most commonly used ASI geometries: square [16], kagome [25,26], pinwheel [13,18], and Ising [27]. Note that when we refer to "pinwheel ASI" in this paper, we are referring explicitly to the 45 ° variant.

Geometries are often decomposed into two or more "sublattices", where the magnets within one sublattice are all aligned, i.e., have the same rotation. In Fig. 4, the sublattice a magnet belongs to is indicated by its color. As can be seen, both square and pinwheel ASIs have two perpendicular sublattices, whereas kagome has three sublattices.

flatspin can be used to model any two-dimensional ASI comprised of identical elements. New geometries can easily be added by extending the model with a new set of positions $\mathbf{r}_i$ and rotations $\theta_i$.

### J. Limitations of the model

The flatspin model makes several assumptions and approximations, which means there are inherent limitations to what

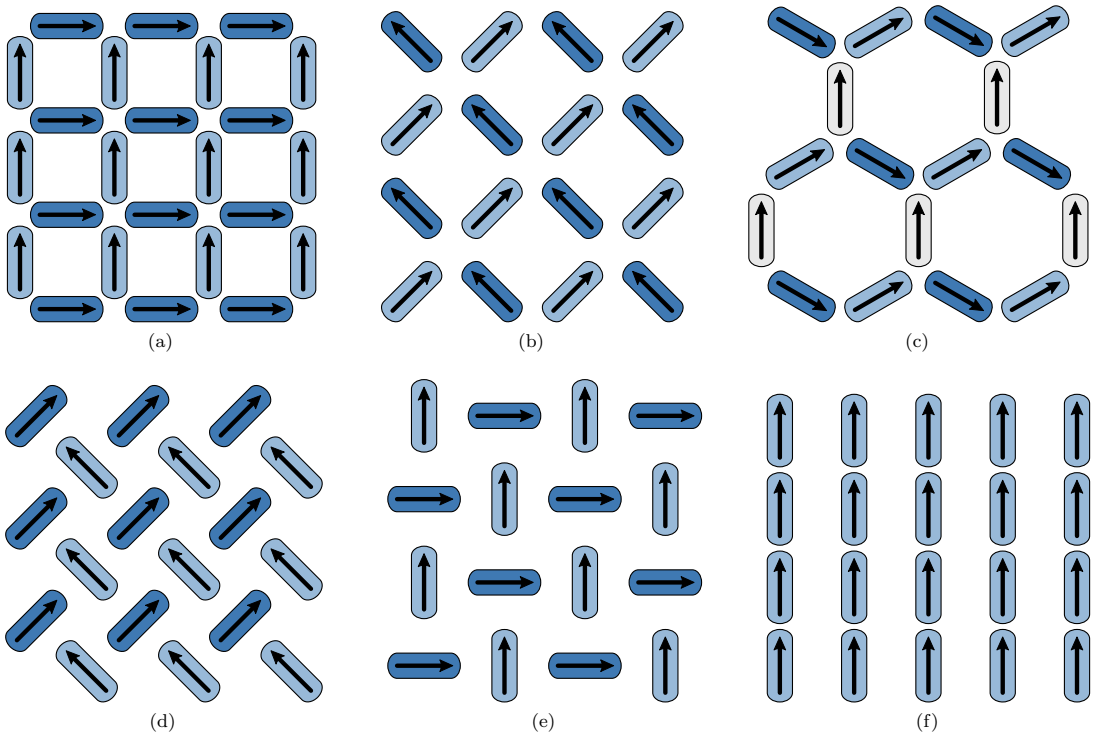


FIG. 4. flatspin includes the most common ASI geometries: (a) Square (closed edges), (b) square (open edges), (c) kagome, (d) pinwheel "diamond", (e) pinwheel "lucky-knot", and (f) Ising.

physics flatspin can capture. In this section, we outline the main limitations of the model.

All magnets in the model are approximated as binary mesoscopic spins, i.e., the magnetization direction of a single magnet is always parallel to the easy axis of the magnet. In reality, the magnetization of nanomagnet islands may deviate somewhat from the easy axis, which in turn would influence the dipolar fields.

It is assumed that the size and shape of all magnets is identical, as all magnets have the same net magnetic moment $M$, and the same switching astroid. Magnet imperfections are modelled solely as a disorder in the coercive fields, i.e., without any effect on the magnetic moment. Hybrid systems with magnets of different size and shape are therefore not supported.

The point dipole approximation underestimates the coupling coefficients for small lattice spacings. As the lateral dimensions of the magnets are not taken into account, the physical proximity of the magnets is underestimated. This can be remedied by artificially increasing the coupling strength $\alpha$ for highly coupled systems.

The dynamical model assumes switching to be instantaneous. In reality, magnetic switching takes finite time, mediated by a rotation of the internal magnetization state. Such transient states may affect ensemble dynamics in subtle ways, which will not be captured in the instantaneous model.

Another limitation of the dynamical model is that switching is assumed to be sequential. While simultaneous switching is possible in reality, it is not modeled in flatspin.

In spite of these limitations, the flatspin model is able to capture a range of real-world phenomena, as we will see in Sec. V.

While flatspin is specifically designed for artificial spin ice consisting of ferromagnetic macrospins, the model could be modified to accommodate other forms of artificial spin systems with bi-stable elements. Some examples include colloidal spin ice [28,29], macroscopic magnets [30], interacting skyrmions [31], and superconducting vortices [32]. Simulating such systems would require three main changes to the flatspin magnetic model. First, the magnetic dipole-dipole interactions (Sec. II C) would need to be replaced with a suitable interaction field along with the interaction modifier $\alpha$. Second, the thermal field (Sec. II E) should be modified to include any other effects of temperature in the relevant system. Finally, a suitable switching mechanism (Sec. II F) must be devised to capture the switching barriers as a function of the total fields.

### K. A note on units

The physical unit of the **h** field in flatspin is Tesla [**T**]. While the **H** field is typically described in units of [$\mathrm{A\,m^{-1}}$], the fields in flatspin are exclusively external to the magnets. In

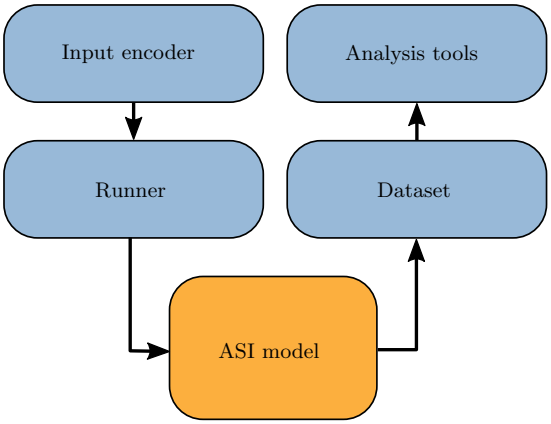


FIG. 5. Overview of the flatspin architecture, with arrows indicating data flow.

other words, the **h** field is equivalent to a **B** field in the absence of material magnetization, i.e., $\mathbf{h} = \mu_0\mathbf{H}$. Correspondingly, the magnetic moments $M$ and $M_{\text{th}}$ have units [A m$^2$].

## III. SIMULATION FRAMEWORK

In addition to a magnetic model, flatspin provides a flexible framework for running simulations, storing results, and performing analysis.

Figure 5 illustrates the overall architecture of flatspin. The *ASI model* has been described in detail in Sec. II. Conceptually, the ASI model describes the physical system under study. The rest of the components are tools used by the researcher to interact with the ASI and observe the results. In this section, we briefly describe each of these components.

The *input encoder* translates a set of input values to a series of external fields. Encoders provide a flexible way to define field protocols. A range of encoders are included, e.g., sinusoidal, sawtooth, and rotational fields.

The responsibility of the *runner* component is to perturb the ASI model according to the field protocol, and save the results. The model, which is fully parametric, receives parameters from the runner, enabling automated parameter sweeps. In addition, there is support for distributed running of simulations on a computing cluster.

Results are stored in a well-defined *dataset* format, which makes the analysis of a large number of simulations straightforward. A suite of *analysis tools* are included, e.g., for plotting results, visualizing ensemble dynamics, and analysis of vertex populations.

flatspin is written in Python and utilizes OpenCL to accelerate calculations on the GPU. OpenCL is supported by most GPU vendors, hence flatspin can run accelerated on a wide variety of platforms. The simulator may also run entirely on CPUs in case GPUs are not available, albeit at a reduced speed.

flatspin is open-source software and released under a GNU GPL license. For more information, see the website [19].

## IV. VERIFICATION OF FLATSPIN

The flatspin software has been verified through an extensive suite of unit tests, where computed results are compared to theoretical values. We do not go into detail about the unit tests here, but the test suite is packaged with the flatspin software, and available from the website [19].

While the unit tests verify the software implementation, a verification of the temperature model itself (Sec. II E) is necessary. In the next section, we compare flatspin simulations to experiments where the results are known analytically.

### Stochastic thermal field

To verify the temperature model in flatspin, we consider the effect of temperature on a system of noninteracting spins at equilibrium. In particular, we investigate the relationship between the temperature scale and the thermal fields, described in Sec. II E. In the following, the magnetization behavior of magnets subjected to an external field and temperature, $M(H,T)$, is simulated and compared to results of other established techniques, both analytical and numerical.

Two different scenarios are considered:

(1) The coercive fields are small compared to the external field, and switching is mostly an effect of the external field competing with temperature.
(2) The switching threshold is comparable to the external field and switching is also influenced by the energy landscape of the magnet, as captured by the shape of the switching astroid.

For scenario (1) we use a switching threshold of $h_k = 1\,\text{mT}$, and for scenario (2) we use $h_k = 20\,\text{mT}$. For both scenarios, we use the unaltered Stoner-Wohlfarth astroid ($b = c = 1$, $\beta = \gamma = 3$).

Ensembles of noninteracting spins ($\alpha = 0$ in flatspin) are subjected to a rising, quasistatic magnetic field aligned with their easy axis, which is held at each field value until equilibrium. Here, equilibrium is defined by the convergence of the mean magnetization over time.

The time intervals were set short enough to avoid a significant probability of multiple flips of one magnet within one interval, and long enough to reach equilibrium within reasonable simulation time. For the low coercivity scenario (1), $\Delta t = 1 \times 10^{-10}\,\text{s}$, and for the high coercivity scenario (2), $\Delta t = 1 \times 10^{-9}\,\text{s}$. Other parameters include the attempt frequency, $f_0 = 1 \times 10^9\,\text{Hz}$ and no disorder.

For the low coercivity scenario, the $M(H)$ curve should match the analytical two-state model described by the Brillouin function for spin-$\frac{1}{2}$ systems [33]. The average magnetization of such a system under an applied field $\mu_0 H$ is described by the analytical expression

$$\langle m_x \rangle = \tanh(A\mu_0 H), \tag{13}$$

where $A = M_S V / k_B T$, i.e., $A\mu_0 H$ is the ratio of the Zeeman energy to thermal energy.

For the high coercivity scenario, the energy barriers and the shape of the astroid becomes significant, and the analytical model breaks down. In this case, we compare results with micromagnetic simulations using MuMax3 [21]. The micromagnetic simulations are set up to capture the $M(H)$ curves

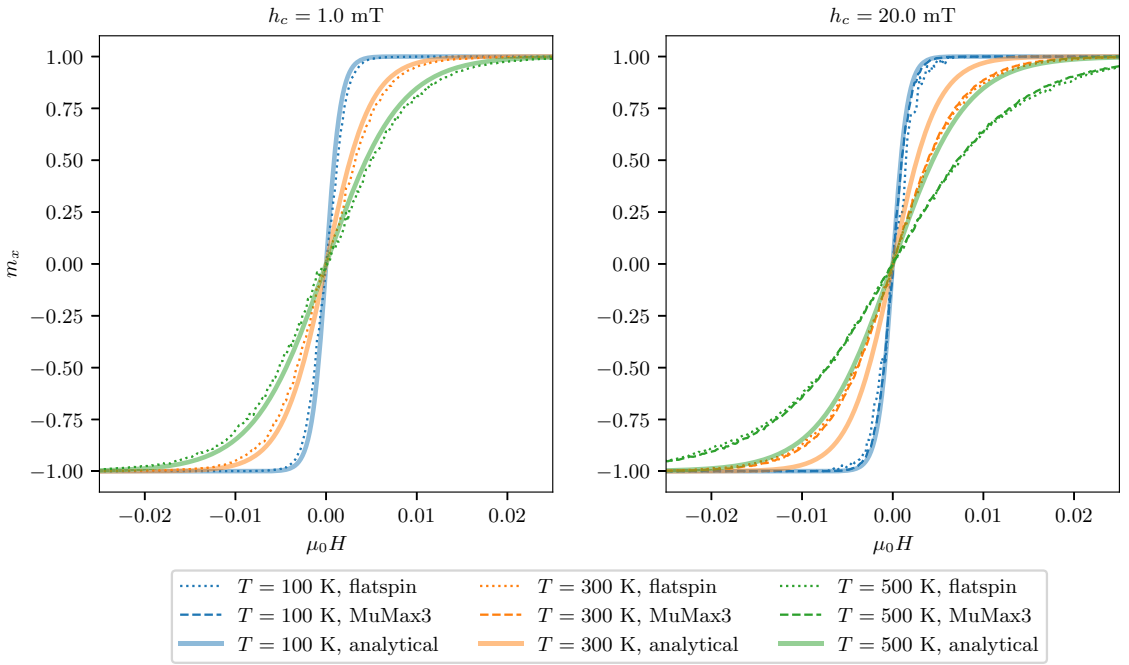


FIG. 6. M(H) curves of ensembles of noninteracting magnets at different temperatures, simulated with different approaches, and for different coercivities. Also indicated is the analytical $\tanh(A\mu_0 H)$ where $A = M_S V/k_B T$. Note that the MuMax3 results are for binned cell magnetization.

of single cell magnets in a rising magnetic field. To isolate the cells in the MuMax3 simulation, the `EnableDemag` property is set to `False` and the exchange stiffness to zero ($A_{ex} = 0\,\mathrm{J\,m^{-1}}$). One period of a 500 Hz stepped ramping field is applied, starting at $\mu_0 H_{ext} = -100$ mT and ending at $\mu_0 H_{ext} = 100$ mT. This field protocol subjects the magnets to a constant field value for 2 $\mu$s before increasing the field by an additional 0.2 mT, which is sufficient to reach thermal equilibrium. The coercivity of $h_c = 20$ mT was reproduced with a material uniaxial anisotropy and $K_{u1} = h_c \cdot M_S/2 = 8600\,\mathrm{J\,m^{-3}}$. Other parameters include a world size of $16 \times 16$ cells and a cell size of $V = 10\,\mathrm{nm}^3 \times 10\,\mathrm{nm}^3 \times 10\,\mathrm{nm}^3$.

Unlike in flatspin, where spins are binary, the cells in the micromagnetic simulations are allowed to exhibit any magnetization direction. To compare the results from flatspin and micromagnetic simulations, the magnetization of micromagnetic cells is binned into spin states of $s_i = \pm 1$, before they are averaged. Note that this binning only approximates the same average magnetization as a system with significant anisotropy, such as in the high coercivity scenario.

For all simulations, we use the parameters $M_S = 860\,\mathrm{kA\,m^{-1}}$, and $V = 10\,\mathrm{nm} \times 10\,\mathrm{nm} \times 10\,\mathrm{nm}$.

Figure 6 presents the results of the flatspin simulations, the micromagnetic simulations, as well as the analytical two-state model of Eq. (13). For the low coercivity scenario ($h_c = 1.0$ mT), the $M(H)$ curves produced by flatspin agree well with the analytical two-state model. For the high coercivity scenario ($h_c = 20.0$ mT), there is a significant deviation between flatspin and the two-state model, but excellent agreement between flatspin and micromagnetic simulations.

For the low coercivity scenario, the agreement between flatspin and the analytical two-state model shows that flatspin's thermal field scales correctly compared to the absolute temperature.

As mentioned, for the high coercivity scenario, the analytical model breaks down, and both flatspin and micromagnetic results deviate significantly from the analytical two-state model. However, there is excellent agreement between the results from flatspin and micromagnetic simulations. Both of these models take the effects of a significant coercivity (significant uniaxial anisotropy) into account. Thus, flatspin is shown to reproduce correct thermal activity also with significant coercivity.

The results presented here are all from systems of noninteracting magnets, where the only influences are the external field and the thermal field. However, since interactions between magnets are mediated by dipolar magnetic fields, the results are also valid for systems of dipolar coupled magnets. The additional dipolar fields can be seen as simple additions to the total field at each magnet, and thus does not alter the validity of the temperature model.

In conclusion, our results show excellent agreement between flatspin and the expected thermal activity for both high and low coercivity scenarios, at equilibrium. For the low coercitvity scenario, the influence of the switching astroid is negligible and flatspin matches the analytical two-state model. For the high coercivity scenario, where the energy barriers are significant, flatspin shows excellent agreement with micromagnetic simulations. These results thereby validate the scaling of temperature in the thermal model of flatspin (Sec. II E).

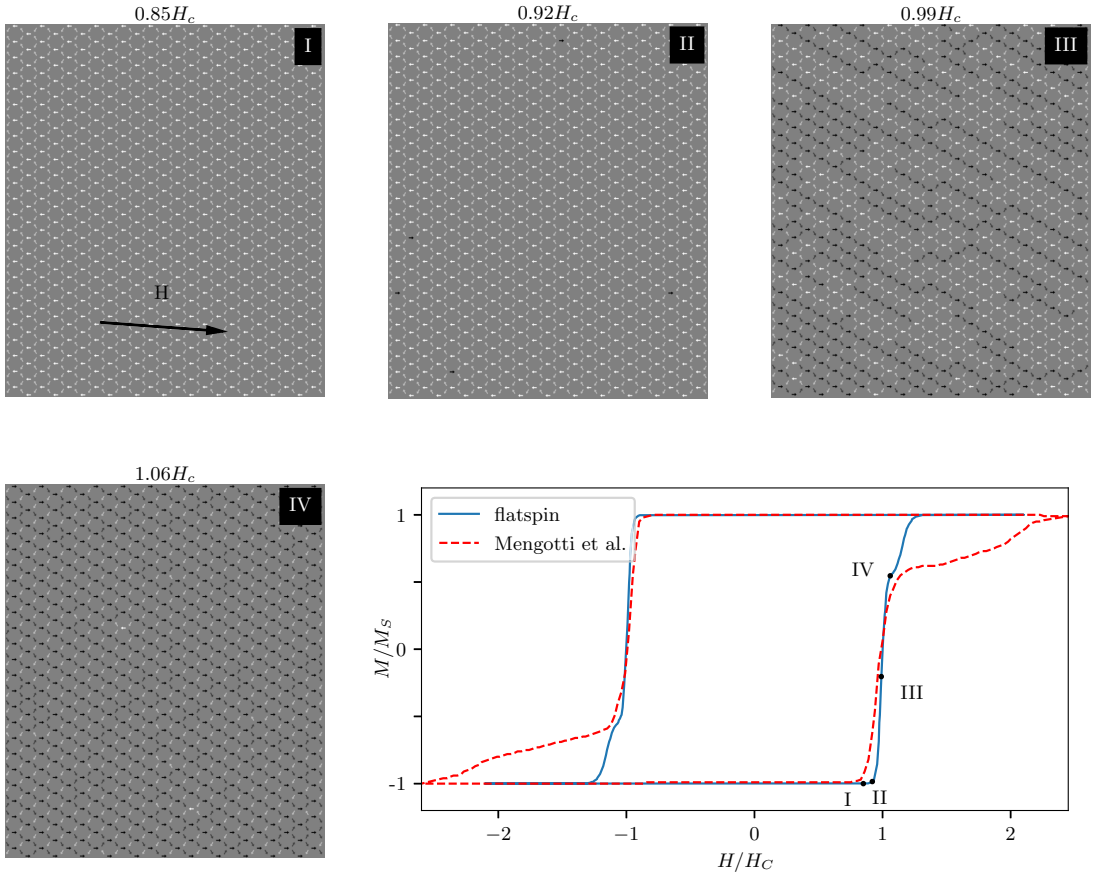


FIG. 7. Left: Snapshots of the evolution of a kagome ASI at selected field values. the images have been cropped to show the middle 80% of the total ASI to improve clarity. Right: Comparison of the hysteresis curve of the simulated ensemble (blue line) against a sketch of the hysteresis curve from the experimental results of Mengotti *et al.* [34] (red-dashed line). The labeled points indicate the points at which the snapshots are sampled from.

## V. VALIDATION OF FLATSPIN

To evaluate the suitability of the simulator, flatspin simulations were compared to established experimental results from literature, as well as micromagnetic simulations. In particular, we investigate phenomena such as Dirac strings in kagome ASI [34], the size of crystallite domains in square ASI [10], and superferromagnetism in pinwheel ASI [13]. Finally, we compare the switching order from flatspin simulations with that of micromagnetic simulations, and investigate the effect of varying lattice spacings.

### A. Dirac strings in kagome ASI

To assess the ability of flatspin to reproduce fine-scale patterns, we consider the emergence of Dirac strings in a kagome ASI [Fig. 4(c)]. Applying a reversal field to a polarized kagome ASI results in the formation of monopole-antimonopole pairs [34]. These pairs are joined by a "string" of nanomagnets, which have flipped due to the reversal field. As the strength of the reversal field increases, the strings elongate until they fill the array.

We closely follow the methodology set out in an experimental study of Dirac strings in kagome ASI [34], in which a room temperature kagome ASI undergoes magnetization reversal. We start with an array of 2638 magnets ($29 \times 29$ hexagons) polarized to the left and apply a reversal field **H** to the right with a slight, downward offset of 3.6°. This offset breaks the symmetry, such that one of the sublattices is now least aligned with the field, resulting in an increased coercive field on this "unfavored" sublattice.

Micromagnetic simulations of magnets of size 470 nm × 160 nm × 20 nm yield the following estimation of flatspin parameters: $\alpha = 0.00103$, $h_k = 0.216$, $\beta = 2.5$, $\gamma = 3$, $b = 0.212$, $c = 1$. The ensemble was simulated at constant room temperature (300 K) with time interval $\Delta t = 1$ s, and with 5% disorder.

The time evolution snapshots of Fig. 7 demonstrate a strong, qualitative similarity to the results of Mengotti *et al.* [34]. We see Dirac strings developing with a preference

to lie along the two sublattices most aligned with the field angle. Furthermore, in the final image, we see the vast majority of unflipped magnets are on the unfavored sublattice, in accordance with both experimental and simulated results from the literature.

Also in Fig. 7, we see the hysteresis of the simulated ensemble (solid line) is similar to that of Mengotti *et al.* [34] (dashed line) in some sections, but differs near the extrema. The hysteresis can be understood in two stages. The first stage, at roughly $M/M_S \in [-0.6, 0.6]$, is dominated by the lengthening of the Dirac strings, with almost no activity occurring on the unfavored sublattice. At $M/M_S < -0.6$ and $M/M_S > 0.6$, the ensemble enters a second stage in which the Dirac strings have fully covered the array, and the change in magnetization is dominated by switching on the unfavored sublattice. Clearly we see good agreement, within stage one, between our simulated hysteresis and the experimental results. Furthermore, there is a clear transition (characterized by a sharp decrease in gradient) in our hysteresis very close to the transition in the experimental hysteresis. Notably, however, although the transitions occur at similar field values, the change in gradient is less pronounced in our simulated hysteresis. This disparity indicates that, in the second stage, the magnets on the unfavored sublattice flip more easily in our simulation than in the experimental data.

As discussed in Sec. II J, the accuracy of the point dipole approximation is known to suffer when considering kagome ASI. Specifically, it has been shown to underestimate the coupling coefficient of the nearest neighbors by approximately a factor of 5 [35], which may contribute to the disparity noted above. Despite this, we observe flatspin accurately reproduces snapshots of the time evolution behavior, while also capturing salient features of the ensemble hysteresis curve.

### B. Domain size in square ASI

In order to demonstrate simulation of large-scale behavior, we have reproduced the emergence of large domains of magnetic order in square ASI, similar to experimental results of Zhang *et al.* [10]. One of the main advantages of flatspin over typical alternatives is the scalability and high throughput of large systems with many magnets. Some emergent ASI phenomena require large systems in order to be fully quantified and studied with high fidelity, such as the domain size of magnetic charge crystallites. For ASIs with strongly coupled magnets, typical domain sizes can become too large for direct experimental observation. Thus, an accurate estimate of the domain size for ASIs with a small lattice spacing is, in part, limited by the number of directly observable magnets.

For a given range of lattice spacings covering both strongly coupled ASIs and weakly coupled ASIs, a corresponding range of large to small magnetic order coherence lengths is expected. In this study, we consider square ASI [closed edges, Fig. 4(a)] with different lattice spacings, $a$, ranging from 320 nm to 880 nm.

Square ASIs of size $50 \times 50$ were annealed in flatspin with a linearly decreasing temperature, starting at $T = 800$ K and decreasing by 1 K until no magnets were active. Each temperature was simulated over 50 simulation steps. The time interval $\Delta t$ of each simulation step was chosen so that the probability of multiple switching events in any single magnet was small, $P_r(k > 1) < 0.001$, or until the total time per temperature value reached 1 min. At high temperatures ($T \gtrsim 720$ K), the requirement $P_r < 0.001$ causes the total time per temperature value to be less than 1 min. This is a trade off between the number of simulation steps allowed and the likelihood of multiple switching events.

The nucleation moment $M_{\text{th}}$ was chosen to match the blocking temperature of the 25-nm-thick magnets reported by Zhang *et al.* [36], where moments are stable below ~670 K. A switching astroid for 220 nm × 80 nm × 25 nm was obtained through micromagnetic simulations, described by generalized astroid parameters $b = 0.38$, $c = 1.0$, $\beta = 1.3$, and $\gamma = 3.6$. Additionally, $h_k = 0.20$, $k_{\text{disorder}} = 0.05$, and a neighbor distance of $10a$ were used. The temperature dependence of the saturation magnetization was accounted for by adjusting $M_{\text{th}}$ according to data reported by Zhang *et al.* [36]. The temperature dependence of $h_k$ was scaled by the same factor. Details of the specific time intervals, temperature and temperature dependent parameter values can be found in flatspin's documentation [19].

In the annealed state, the spin-spin correlation as a function of their lateral separation was calculated across the ensembles. Analysis of the average correlation of annealed states provides insight about the typical coherence length of magnetic order, i.e., magnetic charge crystallite size, or domain size. Here, the correlation of two spins is defined as +1 (–1) if their dipole interaction is minimized (maximized). Averaging correlation across distinct types of spin pairs, in the annealed ASI, gives a measure of how coherent the ASI is at that particular neighbor separation. How quickly the average correlation decreases as a function of separation can be used to estimate the characteristic domain size. In particular, it can be argued that the separation where the correlation falls below $1/e$ is the characteristic domain radius [10,37].

Typical domain structures and correlation results can be seen in Fig. 8. The domains shown in Fig. 8(a) and the correlation curves in Fig. 8(b) are in good agreement with experimental results [10]. A qualitative comparison of the domain sizes and structures in Fig. 8 shows that the domains tend to be larger, with smoother domain boundaries, for smaller $a$. The analysis of coherence as a function of separation also shows similar trends and values, where an increase in $a$ leads to low correlation, even between nearest neighbors.

The discrepancy for $a = 320$ nm is not completely unexpected, as the point-dipole approximation is known to underestimate nearest-neighbor interaction for magnets placed very close together [35]. In strongly coupled systems, each spin flip results in a greater change in dipole energy, compared to systems that are less coupled. This makes a gradual descent towards the ground state by random spin flips (the thermal fluctuations as modeled by flatspin) harder to achieve. These issues may be addressed by increasing the coupling parameter $\alpha$ for nearest neighbor spins, and by a longer and slower annealing protocol. A longer and slower annealing protocol will inevitably come at the cost of longer computation times.

These results show that flatspin provides sufficient flexibility, fidelity and performance required to reproduce experimentally observed large-scale emergent behavior in ASIs.

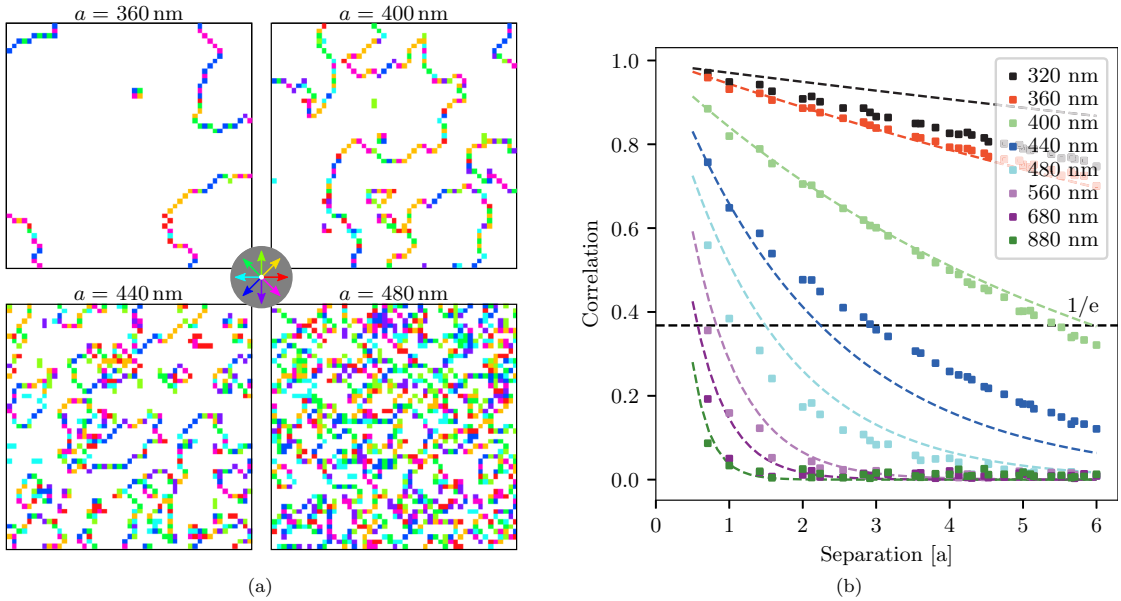


FIG. 8. (a) Maps showing the net magnetization of the ASI vertices, for an annealed 50 × 50 square ASI with the given lattice spacing $a$. The white regions have zero net magnetization, and thus correspond to a coherent domain of type I vertices. Colored regions have a nonzero net magnetization, direction indicated by the color wheel, and correspond to type II or III vertices. (b) The absolute value of spin-spin correlation at a given separation for square ASIs of different lattice spacings, $a$. Dashed curves show exponential best fits for data from the original paper [10]. Also indicated is a $1/e$ threshold of correlation.

### C. Superferromagnetism in pinwheel ASI

In this section, we use flatspin to reproduce the dynamic behavior of pinwheel ASI, which had yet to be demonstrated with a dipole model [13]. We find that our switching criteria plays a key role in replicating magnetization details during the field-driven array reversal.

Pinwheel ASI is obtained by rotating each island in square ASI some angle about its center. A rotation of 45 degrees results in a transition from antiferromagnetic to ferromagnetic order [18]. The dynamics of pinwheel ASI in many ways resemble continuous ferromagnetic thin films, with mesoscopic domain growth originating from nucleation sites, followed by coherent domain propagation and complete magnetization reversal [13].

Here, we demonstrate that flatspin is able to replicate the experimental reversal processes presented in Li *et al.* [13], where pinwheel "diamond" ASI [Fig. 4(d)] is subject to an external field at different angles. A key result is that the angle $\theta$ of the external field controls the nature of the reversal process. When $\theta$ is small (equally aligned to both sublattices), reversal happens in a single avalanche, whereas when $\theta$ is large (more aligned to one sublattice), reversal happens in a two-step process where one sublattice switches completely before the other. Previous attempts at capturing this behavior in a dipole model have proven difficult [13].

To replicate this process in flatspin, an asymmetric switching astroid is required, i.e., the threshold along the parallel component is reduced by setting $b < 1$ in Eq. (11). From micromagnetic simulations of a single $470 \times 170 \times 10\,\mathrm{nm}$ magnet, we obtain the following characteristic switching parameters: $b = 0.28$, $c = 1.0$, $\beta = 4.8$, and $\gamma = 3.0$. Other simulation parameters include $\alpha \approx 0.00033$, $h_k = 0.098$, $k_{\mathrm{disorder}} = 0.05$, and a neighbor distance of $10a$. Full simulation details are available in the flatspin documentation [19].

Figures 9(a)–9(d) show hysteresis loops and array snapshots when the field is aligned with the array ($\theta = 0^\circ$ and $\theta = -6^\circ$). As can be seen, the results from flatspin [Figs. 9(b) and 9(d)] are qualitatively very similar to experimental results [Figs. 9(a) and 9(c)]. In all cases, the ASI undergoes reversal in a single avalanche. Reversal begins at a few nucleation points close to the edge, followed by domain growth and domain wall movement perpendicular to the direction of the field. The simulated system appears to have an anisotropy axis of $0^\circ$ as opposed to $-6^\circ$ observed experimentally. Hence, Fig. 9(b) is most similar to Fig. 9(c) and Fig. 9(d) is most similar to Fig. 9(a). It should be noted that the tilted anisotropy axis found experimentally has not yet been explained.

Figures 9(e) and 9(f) show the hysteresis loops and array snapshots when the field is misaligned with the array ($\theta = 30^\circ$). Again, flatspin simulations [Fig. 9(f)] replicate key features observed experimentally [Fig. 9(e)]. Reversal now happens in two steps: the sublattice whose magnets have their easy axis most aligned with the field will switch first, followed later by the other sublattice. This two-step reversal process results in an emergent rotation of the collective magnetization. The magnetization is constrained to follow the orientation of the magnets, resulting in reversal via stripe patterns at $45^\circ$.

Li *et al.* [13] report they were unable to replicate the magnetization details using a point-dipole Monte Carlo model.

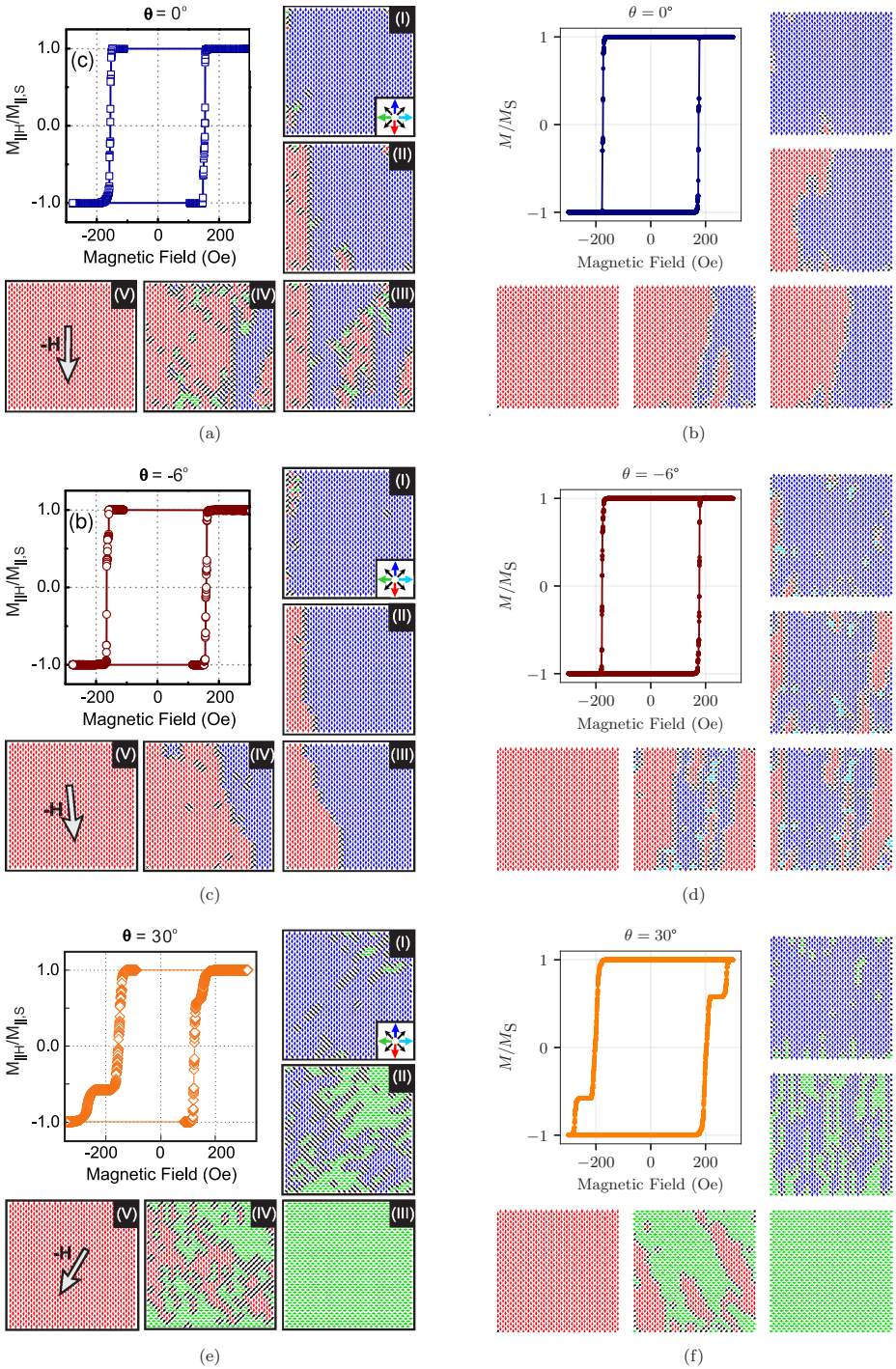


FIG. 9. Hysteresis loop and snapshots of the pinwheel units for various angles $\theta$ of the applied field. Figures (a), (c), and (e) show experimental results, adapted from Li *et al.* [13], Copyright ©2018 American Chemical Society, CC-BY-4.0 . Figures (b), (d), and (f) show results from flatspin simulation.

One crucial difference between flatspin and their dipole model is the switching criteria. They use the simpler criteria $\mathbf{h}_i \cdot \mathbf{m}_i < h_k^{(i)}$, which considers only the parallel field component and will be largely inaccurate for fields that are not aligned with the magnet's easy axis. Indeed, we find that the generalized Stoner-Wohlfarth model (Sec. II F) is crucial to reproduce the reversal process and magnetization details.

### D. Comparison to micromagnetic single-spin switching order

Micromagnetic simulations, e.g., MuMax3 [21,38], are taken as the gold standard and generally agree with experimental results, due to the high simulation fidelity of the micromagnetic model. In this section, we compare how well flatspin agrees with MuMax3 at the level of detail expressed in flatspin.

Here we evaluate the switching strategy outlined in Sec. II H, by comparing the switching orders obtained in flatspin and MuMax3, of a square ASI as it undergoes reversal by an external field. Switching order refers to the sequence in which individual magnets switch their magnetization state. As a similarity measure, Spearman's rank correlation coefficient $\rho$ [39] is used, where a value of 1 indicates perfect correlation and 0 indicates no correlation between switching orders.

In the weakly coupled regime, the switching order is dominated by the coercivity of each individual magnet, i.e., low coercivity magnets switch first, and high coercivity magnets switch last. In flatspin, the coercive field can be set directly by modifying $h_k^{(i)}$. In MuMax3, we control the coercive field implicitly, by varying the first-order, uniaxial, magnetocrystalline anisotropy, $K_{U1}^{(i)}$ of each magnet. Given a set of randomly drawn $K_{U1}^{(i)}$ values, the corresponding $h_k^{(i)}$ values were obtained by a linear map. In this way, the distribution of magnet coercivities in the two models match.

The system we considered was a $4 \times 4$ square (closed) ASI, each magnet measuring $220\,\text{nm} \times 80\,\text{nm} \times 25\,\text{nm}$. flatspin was run with parameters $b = 0.38$, $c = 1$, $\beta = 1.5$, and $\gamma = 3.2$. In both simulators, we applied a gradually increasing reversal field at $\theta = 44^\circ$.

As the lattice spacing is decreased, the dipolar interactions begin contributing to the switching order. To verify that flatspin captures switching dynamics, we perform a comparison of the switching orders for all pairs of lattice spacings in both simulators.

Figure 10(a) shows the correlations for each pair of lattice spacings as an average over 32 different square ASIs. We observe a clear linear relationship between the two simulators, with higher lattice spacings exhibiting higher correlation. The nonzero y-intercept in the heatmap indicates that, as expected, the coupling strength is slightly underestimated by the dipole approximation employed in flatspin, in particular for lower lattice spacings. For example, flatspin with 300 nm lattice spacing is most similar to MuMax3 with 380 nm.

The red line in Fig. 10(b) traces the ridge in the heatmap, i.e., the highest $\rho$, for each flatspin lattice spacing. As can be seen, a near-perfect agreement between the simulators is found in the weakly coupled regime (high lattice spacing). As lattice spacings decrease, the magnets start to interact through dipolar coupling. Below 450 nm, the correlation drops. Since

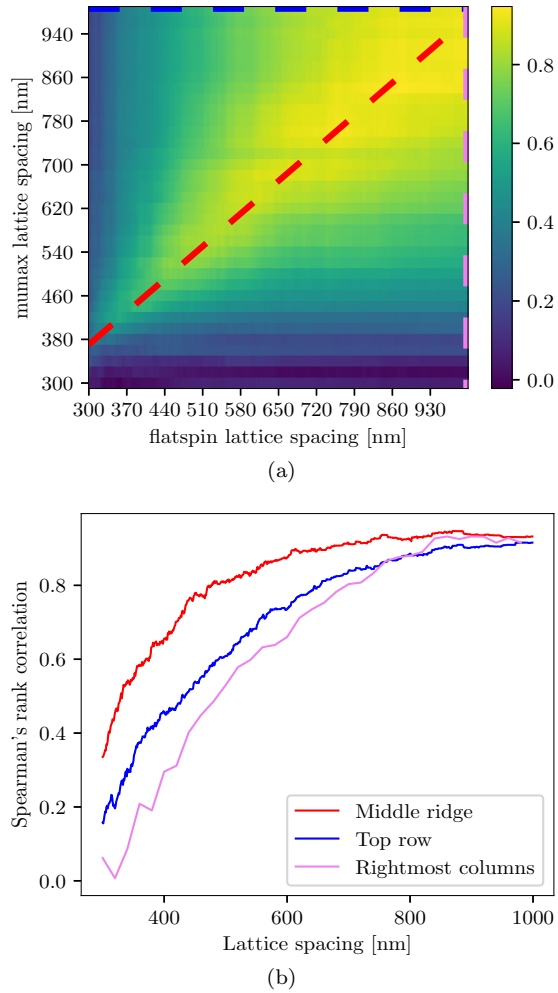


FIG. 10. (a) Spearman's rank correlation coefficients $\rho$ averaged over 32 different square ASIs, evaluated for different lattice spacings in flatspin and MuMax3. The red line shows the approximate maximum ridge line through the heatmap. (b) The red line shows the true maximum $\rho$ for the lattice spacing pairs. The blue and violet lines show projections of the top row and rightmost column of (a), respectively.

flatspin does not account for the micromagnetic state, complete correlation is not expected.

The particular selection of $h_k^{(i)}$ values of flatspin, and the corresponding $K_{U1}$ values of MuMax3, introduces an *inherent* bias in the switching order. One might expect that this quenched disorder dominates the switching order, leading to an inflated correlation between flatspin and MuMax3, regardless of dipole interactions.

The violet line of Fig. 10(b) [plotting the rightmost column from Fig. 10(a)], shows the correlation between MuMax3 and the uncoupled flatspin system (lattice spacing of 1000 nm). If the quenched disorder completely dominated the

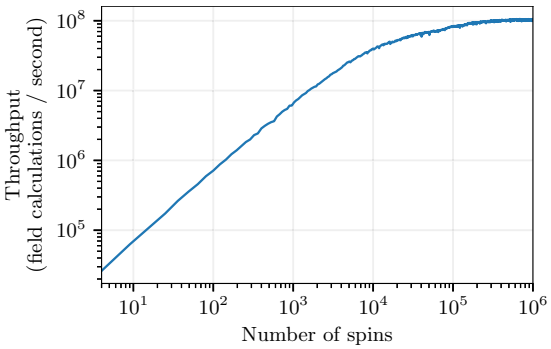


FIG. 11. The throughput (number of field calculations per second) as a function of number of spins. Throughput is averaged over 100 simulations of each size. The test was performed on an NVIDIA Tesla V100 GPU with 32 GB of RAM. Note the logarithmic scale of the axes.

switching order, one would expect this to be a flat line, as increasing the dipole coupling (by reducing lattice spacing) would have no effect. The blue line of Fig. 10(b) [top row from Fig. 10(a)] show the corresponding curve comparing flatspin to the uncoupled MuMax3 system. In both cases, the correlation rapidly declines with lattice spacing, confirming that the switching order is not dominated by the inherent bias for highly coupled systems. Furthermore, the red line clearly shows a stronger agreement when the lattice spacing of MuMax3 and flatspin are both varied proportionally. We conclude that flatspin and MuMax3 capture similar switching dynamics.

## VI. PERFORMANCE

Although the total simulation time will depend on many factors, it is of interest to measure how simulation time scales with the number of spins. As the number of spins are increased, simulation time will be largely dominated by the calculation of the effective field, $\mathbf{h}_i$, acting on each of the $N$ spins in the lattice. Computing time for $\mathbf{h}_{\text{dip}}^{(i)}$ depends on the number of neighbors around spin $i$, which is typically constant for all spins except the ones at the edges of the geometry. For large $N$, the number of edge magnets is negligible (in the common ASI geometries). Computing $\mathbf{h}_i$ for all spins will take $\mathcal{O}(N)$ time, i.e., computation time grows no faster than linear in $N$.

Figure 11 shows the throughput (number of field calculations per second) as a function of the number of spins. Here a field calculation is defined as the computation of $\mathbf{h}_i$ for a single spin $i$, hence for $N$ spins there will be $N$ such field calculations. The geometry used was square ASI (open edges) using a standard 8 spin neighborhood for calculating $\mathbf{h}_{\text{dip}}^{(i)}$. The throughput was averaged over 100 simulations of each size. The test was performed on an NVIDIA Tesla V100 GPU with 32 GB of RAM.

At around 200 000 spins, the throughput saturates at $10^8$ field calculations per second. On our test setup, computing $\mathbf{h}_i$ for one million spins takes approximately 10 ms. Above 200 000 spins, we are able to fully utilize the GPU resources.

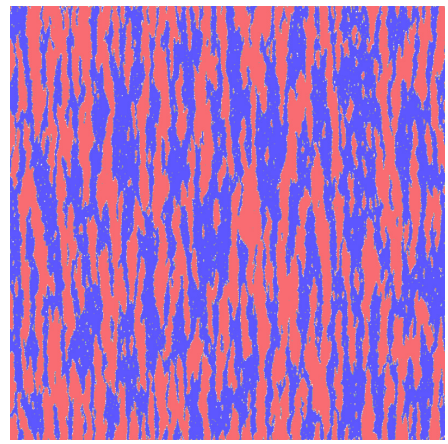

FIG. 12. A snapshot from flatspin simulations of a pinwheel ASI system with more than one million magnets, as it undergoes reversal by an external field. The angle of the external field is $\theta = 0°$.

To simulate the reversal of an ASI by a gradually increasing external field, at least one field calculation per spin flip is required, i.e., at least $N$ field calculations. If the external field gradually changes with a resolution of $K$ values, the worst case will be when all spins flip during a single field value. In this case the number of field calculations required will be $N + K - 1$ since there will be $K - 1$ field calculations that results in no spin flips.

The total simulation time depends largely on the particular experimental setup, parameters and other system characteristics. Time will be spent on things other than field calculations, e.g., organizing and writing results to storage. Hence, the total simulation time will be longer than predicted by field calculations alone. As an example, the simulations from Sec. V C of $25 \times 25$ pinwheel ASI with 1250 magnets took approximately 6 seconds with $K = 2500$, for one reversal.

Figure 12 shows a snapshot from flatspin simulations of a large pinwheel ASI system as it undergoes reversal by an external field. With more than one million magnets, the simulation of array reversal took several days to complete. A video of the full reversal is available as Supplemental Material [40].

The ability to simulate such large systems allows a researcher to explore phenomena at much larger scales than can be directly observed experimentally. The imaging window of experimental techniques with single spin resolution, such as magnetic force microscopy (MFM), is typically limited to about $50\,\mu\text{m} \times 50\,\mu\text{m}$. However, much smaller imaging windows are frequently used due to other practical considerations. For instance, the square ASI investigated by [10] is a typical example, where 5000 magnets are imaged.

## VII. SQUARE ASI ROBUSTNESS TO DILUTION DEFECTS

In the following, we will make use of the unique framework provided by flatspin to explore new aspects of ASI behavior.

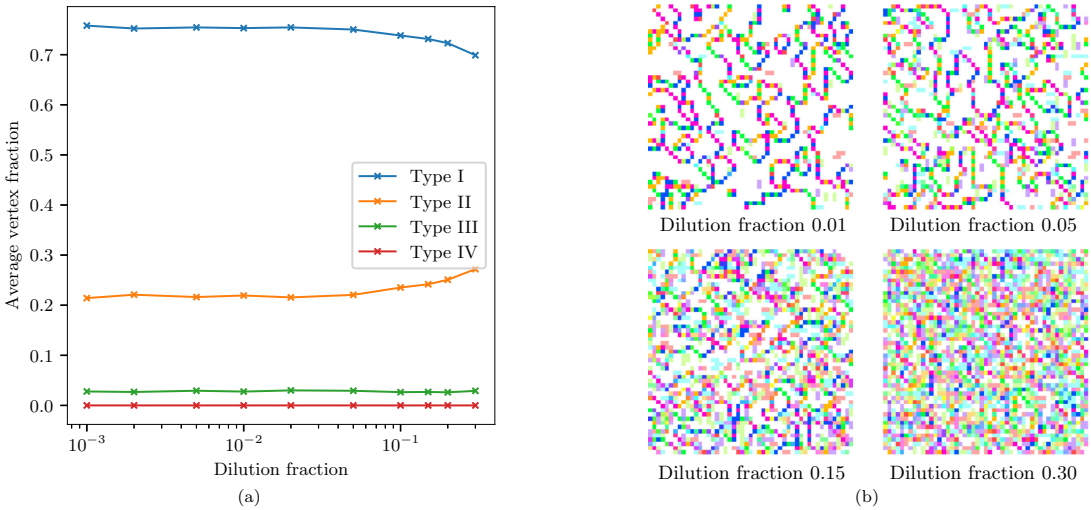


FIG. 13. (a) Average complete vertex fraction, by type, as a function of dilution by removal of spins in a $50 \times 50$ square ASI. Only complete vertices are included. The averages are taken over 10 different instances for each dilution fraction. (b) Example end states of square ASI of different dilutions. Each pixel correspond to the net magnetization of 4 spins (vertices), as in Fig. 8(a). Note that white pixels correspond to vertices of no net magnetization (type I vertices *if* the vertices are complete, as there are no type IV vertices).

While square ASI is perhaps one of the most investigated ASI systems, mainly due to its display of magnetically charged defects with associated Coulombic interactions and string tension [1,41], the robustness of this system with respect to lattice defects is largely unexplored. For the kagome ASI it has, however, been recognized that significant removal of elements in the lattice will cause the phase transition of the system (from spin ice I state to the ordered spin ice II state) to disappear [42]. Related work on particle-based ice of the square geometry has revealed an apparent ice rule fragility with respect to similar dilution [43,44]. Here, we use flatspin to investigate the effect of dilution defects, i.e., random removal of lattice elements, on square vertex population and domain size in the ASI after a field demagnetization protocol.

Large ASI systems are needed to observe large-scale phenomena such as domain formation and the effects of sparse random dilution. Random defects result in stochastic behavior, as the results will depend on the exact configuration of the defects. Hence, to provide sufficient statistics of these phenomena, the experiments must be repeated for different random configurations. Furthermore, this is combined with long field protocols, which are required to relax each system to a lower energy configuration.

The two-fold degenerate ground state configurations in square ASI consist of antiferromagnetic ordering on the vertical and horizontal sublattices [10]. Reaching this ground-state configuration experimentally has proven difficult. Relaxation through thermal annealing or field protocols will typically result in domains of charge neutral type I vertices separated by domain walls comprised of mostly type II vertices with a net magnetization (and no net magnetic charge). These domain walls, strings of type II vertices, are necessarily terminated by type III (or less frequently: type IV) vertices of opposite net magnetic charge, or at incomplete vertices, such as at the edges of the ensemble.

Diluting the ASI lattice by removal of elements introduces more vertices with uncompensated magnetic charge. Here, we use flatspin to explore how such doping with fixed magnetic charges affects the magnetic vertex population of a square ASI.

A $50 \times 50$ square ASI is initialized uniformly and subjected to a rotating magnetic field with decreasing amplitude. The initial amplitude is slightly larger than a saturating field, and is decreased linearly over 1000 periods. The final periods do not alter the state of the ASI. Individual spins are assigned a $h_k = 0.2$ with 5% disorder, and the field amplitude, directed at $45^\circ$, starts at $h = 0.080$ and ends at $h = 0.072$. Each spin is again modeled as a rectangular magnet, with astroid parameters $b = 0.38$, $c = 1.0$, $\beta = 1.3$, $\gamma = 3.6$, and $\alpha = 30272$, with a lattice spacing $a = 300\,\text{nm}$. A neighbor distance of $3a$ is used in the simulations. Larger neighbor distances (up to $50a$) were sampled for the undiluted system and revealed no discrepancy from a neighbor distance of $3a$. Spins in the lattice are removed randomly, until the desired dilution fraction is achieved. Ten different instances of this random removal were performed for each level of dilution.

After the field protocol described above, the *complete* (undiluted) vertices of the final state were counted and classified according to their vertex type. The resulting vertex fraction count of complete vertices can be seen in Fig. 13(a).

Somewhat surprisingly, the fraction of each vertex type at the end of the field protocol is almost constant through dilution. We also note that a large fraction of the complete vertices ($>0.70$) obey the ice rules (type I or type II), indicating that the system is strongly coupled.

Another apparent effect of dilution is a dramatic reduction in domain size, see Fig. 13(b). It is interesting to note that,

despite the change of domain size, which should include more domain boundaries and more magnetized vertices, the type population fraction stays constant through dilution. Our findings indicate that the fixed magnetic charges introduced through dilution comes in addition to the mobile magnetic charges. While the domain walls in systems with low dilution are comprised of ordinary type II vertices, the fixed incomplete vertices add up with complete type II vertices to form more domain walls for the systems with higher dilution and, thus, smaller domains.

The presented simulation study demonstrates that the type population in square ASI is robust towards dilution. However, the sizes of ground-state domains reduce considerably as an increasing number of magnetic islands are removed at random, as seen in [10]. This preliminary study into the effect of dilution defects in square ASI demonstrates how flatspin can be used as an efficient tool to explore new physical phenomena in ASI systems, which in turn can be verified by experiments.

## VIII. CONCLUSION

flatspin is a highly effective simulator for ASI systems. At its heart lies a robust magnetic model based on dipole-dipole interactions, with a switching criteria based on a generalized Stoner-Wohlfarth model, and thermal fluctuations based on the Arrhenius-Néel equation. Accompanying the model is a toolbox of useful input encoders and analysis tools. The model includes several common ASI geometries, and there are no inherent limits to the range of possible geometries.

The flatspin ASI model has been verified against established theory and micromagnetic simulations, and validated against experimental results from the literature. Emergent fine-scale patterns in kagome ASI were replicated successfully, where the formation of Dirac strings matched experimental results. Large-scale domain sizes in square ASI were reproduced, and good agreement was found between flatspin and experimental results. Using flatspin, the experimental magnetization reversal of pinwheel ASI was reproduced for the first time in a dipole model. On a detailed level, we found good agreement between micromagnetic simulations and flatspin in terms of magnet switching order.

Finally, we shed light on the effects of dilution defects in square ASI. Our investigation revealed a surprisingly robust vertex type population, as random magnets were removed from the lattice.

Through GPU acceleration, flatspin scales to large ASI systems with millions of magnets. High speed, parallel computation allows for many ASI simulations to be executed, enabling quick exploration of parameters and novel geometries. The flexibility and performance offered by flatspin open for exciting new possibilities in ASI research.

## ACKNOWLEDGMENTS

We thank Bartel Van Waeyenberge for fruitful discussions. This work was funded in part by the Norwegian Research Council by the IKTPLUSS project SOCRATES (Grant No. 270961), and in part by the EU FET-Open RIA project SpinENGINE (Grant No. 861618). Simulations were executed on the NTNU EPIC compute cluster [45]. J.L. is supported by the Research Foundation - Flanders (FWO) through a senior postdoctoral research fellowship (12W7622N).

[1] S. H. Skjærvø, C. H. Marrows, R. L. Stamps, and L. J. Heyderman, Advances in artificial spin ice, Nat. Rev. Phys. **2**, 13 (2020).

[2] L. J. Heyderman and R. L. Stamps, Artificial ferroic systems: novel functionality from structure, interactions and dynamics, J. Phys.: Condens. Matter **25**, 363201 (2013).

[3] J. Sklenar, Y. Lao, A. Albrecht, J. D. Watts, C. Nisoli, G.-W. Chern, and P. Schiffer, Field-induced phase coexistence in an artificial spin ice, Nat. Phys. **15**, 191 (2019).

[4] D. J. P. Morris, D. A. Tennant, S. A. Grigera, B. Klemke, C. Castelnovo, R. Moessner, C. Czternasty, M. Meissner, K. C. Rule, J.-U. Hoffmann, K. Kiefer, S. Gerischer, D. Slobinsky, and R. S. Perry, Dirac strings and magnetic monopoles in the spin ice $Dy_2Ti_2O_7$, Science **326**, 411 (2009).

[5] D. Levis, L. F. Cugliandolo, L. Foini, and M. Tarzia, Thermal Phase Transitions in Artificial Spin Ice, Phys. Rev. Lett. **110**, 207206 (2013).

[6] L. Anghinolfi, H. Luetkens, J. Perron, M. G. Flokstra, O. Sendetskyi, A. Suter, T. Prokscha, P. M. Derlet, S. L. Lee, and L. J. Heyderman, Thermodynamic phase transitions in a frustrated magnetic metamaterial, Nat. Commun. **6**, 8278 (2015).

[7] J. H. Jensen, E. Folven, and G. Tufte, Computation in artificial spin ice, in *The 2018 Conference on Artificial Life* (MIT Press, Cambridge, MA, 2018), pp. 15–22

[8] J. H. Jensen and G. Tufte, Reservoir computing in artificial spin ice, in *The 2020 Conference on Artificial Life* (MIT Press, Cambridge, MA, 2020), pp. 376–383.

[9] Z. Budrikis, Athermal dynamics of artificial spin ice: disorder, edge and field protocol effects, Ph.D. thesis, The University of Western Australia, 2012.

[10] S. Zhang, I. Gilbert, C. Nisoli, G. W. Chern, M. J. Erickson, L. O'Brien, C. Leighton, P. E. Lammert, V. H. Crespi, and P. Schiffer, Crystallites of magnetic charges in artificial spin ice, Nature (London) **500**, 553 (2013).

[11] X. Ke, J. Li, C. Nisoli, P. E. Lammert, W. McConville, R. F. Wang, V. H. Crespi, and P. Schiffer, Energy Minimization and ac Demagnetization in a Nanomagnet Array, Phys. Rev. Lett. **101**, 037205 (2008).

[12] Y. Bar-Yam, *Dynamics of Complex Systems* (Addison-Wesley, Reading, MA, 1997).

[13] Y. Li, G. W. Paterson, G. M. Macauley, F. S. Nascimento, C. Ferguson, S. A. Morley, M. C. Rosamond, E. H. Linfield, D. A. MacLaren, R. Macêdo *et al.*, Superferromagnetism and domain-wall topologies in artificial "pinwheel" spin ice, ACS Nano **13**, 2213 (2019).

[14] J. Frenkel and J. Dorfman, Spontaneous and induced magnetisation in ferromagnetic bodies, Nature (London) **126**, 274 (1930).

[15] C. Kittel, Theory of the structure of ferromagnetic domains in films and small particles, Phys. Rev. **70**, 965 (1946).

[16] R. F. Wang, C. Nisoli, R. S. Freitas, J. Li, W. McConville, B. J. Cooley, M. S. Lund, N. Samarth, C. Leighton, V. H. Crespi, and P. Schiffer, Artificial 'spin ice' in a geometrically frustrated lattice of nanoscale ferromagnetic islands, Nature (London) **439**, 303 (2006).

[17] C. Fan and F. Y. Wu, Ising model with second-neighbor interaction. I. Some exact results and an approximate solution, Phys. Rev. **179**, 560 (1969).

[18] R. Macêdo, G. M. Macauley, F. S. Nascimento, and R. L. Stamps, Apparent ferromagnetism in the pinwheel artificial spin ice, Phys. Rev. B **98**, 014437 (2018).

[19] flatspin contributors, flatspin website, https://flatspin.gitlab.io (2020).

[20] L. Néel, Théorie du traînage magnétique des ferromagnétiques en grains fins avec applications aux terres cuites, Ann. Geophys. **5**, 99 (1949).

[21] A. Vansteenkiste, J. Leliaert, M. Dvornik, M. Helsen, F. Garcia-Sanchez, and B. Van Waeyenberge, The design and verification of MuMax3, AIP Adv. **4**, 107133 (2014).

[22] C. Tannous and J. Gieraltowski, The stoner–wohlfarth model of ferromagnetism, Eur. J. Phys. **29**, 475 (2008).

[23] R. Kikuchi, On the minimum of magnetization reversal time, J. Appl. Phys. **27**, 1352 (1956).

[24] P. R. Gillette and K. Oshima, Magnetization reversal by rotation, J. Appl. Phys. **29**, 529 (1958).

[25] M. Tanaka, E. Saitoh, H. Miyajima, T. Yamaoka, and Y. Iye, Magnetic interactions in a ferromagnetic honeycomb nanoscale network, Phys. Rev. B **73**, 052411 (2006).

[26] Y. Qi, T. Brintlinger, and J. Cumings, Direct observation of the ice rule in an artificial kagome spin ice, Phys. Rev. B **77**, 094418 (2008).

[27] M. Saccone, A. Scholl, S. Velten, S. Dhuey, K. Hofhuis, C. Wuth, Y.-L. Huang, Z. Chen, R. V. Chopdekar, and A. Farhan, Towards artificial Ising spin glasses: Thermal ordering in randomized arrays of Ising-type nanomagnets, Phys. Rev. B **99**, 224403 (2019).

[28] A. Libál, C. Reichhardt, and C. J. Olson Reichhardt, Realizing Colloidal Artificial Ice on Arrays of Optical Traps, Phys. Rev. Lett. **97**, 228302 (2006).

[29] A. Ortiz-Ambriz and P. Tierno, Engineering of frustration in colloidal artificial ices realized on microfeatured grooved lattices, Nat. Commun. **7**, 10575 (2016).

[30] P. Mellado, A. Concha, and L. Mahadevan, Macroscopic Magnetic Frustration, Phys. Rev. Lett. **109**, 257203 (2012).

[31] F. Ma, C. Reichhardt, W. Gan, C. J. Olson Reichhardt, and W. S. Lew, Emergent geometric frustration of artificial magnetic skyrmion crystals, Phys. Rev. B **94**, 144405 (2016).

[32] A. Libál, C. J. Olson Reichhardt, and C. Reichhardt, Creating Artificial Ice States Using Vortices in Nanostructured Superconductors, Phys. Rev. Lett. **102**, 237004 (2009).

[33] C. Kittel, *Introduction to Solid State Physics*, 8th ed. (John Wiley, Hoboken, NJ, 2004), pp. 303–304.

[34] E. Mengotti, L. J. Heyderman, A. F. Rodríguez, F. Nolting, R. V. Hügli, and H.-B. Braun, Real-space observation of emergent magnetic monopoles and associated dirac strings in artificial kagome spin ice, Nat. Phys. **7**, 68 (2011).

[35] N. Rougemaille, F. Montaigne, B. Canals, A. Duluard, D. Lacour, M. Hehn, R. Belkhou, O. Fruchart, S. El Moussaoui, A. Bendounan, and F. Maccherozzi, Artificial Kagome Arrays of Nanomagnets: A Frozen Dipolar Spin Ice, Phys. Rev. Lett. **106**, 057209 (2011).

[36] X. Zhang, Y. Lao, J. Sklenar, N. S. Bingham, J. T. Batley, J. D. Watts, C. Nisoli, C. Leighton, and P. Schiffer, Understanding thermal annealing of artificial spin ice, APL Mater. **7**, 111112 (2019).

[37] M. E. J. Newman and G. T. Barkema, *Monte Carlo Methods in Statistical Physics* (Clarendon Press, Oxford, 1999).

[38] J. Leliaert, M. Dvornik, J. Mulkers, J. De Clercq, M. V. Milošević, and B. Van Waeyenberge, Fast micromagnetic simulations on GPU - Recent advances made with mumax3, J. Phys. D **51**, 123002 (2018).

[39] J. D. Gibbons and S. Chakraborti, *Nonparametric Statistical Inference: Revised and Expanded* (CRC Press, Boca Raton, FL, 2014).

[40] See Supplemental Material at http://link.aps.org/supplemental/10.1103/PhysRevB.106.064408 for a video of the reversal of 708x708 pinwheel ASI.

[41] L. A. Mól, R. L. Silva, R. C. Silva, A. R. Pereira, W. A. Moura-Melo, B. V. Costa, and M. Carlo, Magnetic monopole and string excitations in two-dimensional spin ice, J. Appl. Phys. **106**, 063913 (2009).

[42] P. Andriushchenko, Influence of cutoff dipole interaction radius and dilution on phase transition in kagome artificial spin ice, J. Magn. Magn. Mater. **476**, 284 (2019).

[43] A. Libál, D. Y. Lee, A. Ortiz-Ambriz, C. Reichhardt, C. J. O. Reichhardt, P. Tierno, and C. Nisoli, Ice rule fragility via topological charge transfer in artificial colloidal ice, Nat. Commun. **9**, 4146 (2018).

[44] C. Nisoli, Unexpected Phenomenology in Particle-Based Ice Absent in Magnetic Spin Ice, Phys. Rev. Lett. **120**, 167205 (2018).

[45] M. Själander, M. Jahre, G. Tufte, and N. Reissmann, EPIC: An energy-efficient, high-performance GPGPU computing research infrastructure, arXiv:1912.05848.

# On the Antiferromagnetic-Ferromagnetic Phase Transition in Pinwheel Artificial Spin Ice

Anders Strømberg,[1,*] Einar Digernes,[1] Rajesh Vilas Chopdekar,[2] Jostein Grepstad,[1] and Erik Folven[1]

[1] *Department of Electronic Systems, Norwegian University of Science and Technology, Trondheim, Norway.*
[2] *Advanced Light Source, Lawrence Berkeley National Laboratory, Berkeley 94720, California, USA*

(Dated: April 5, 2024)

Nanopatterned magnetic thin films offer a platform for exploration of tailored magnetic properties such as emergent long-range order. A prominent example is artificial spin ice (ASI), where an arrangement of nanoscale magnetic elements, acting as macrospins, interact via their dipolar fields. In this study, we discuss the transition from antiferromagnetic (AF) to ferromagnetic (FM) long-range order in a square lattice ASI, as the magnetic elements are gradually rotated through 45° to a "pinwheel" configuration. The AF–FM transition is observed experimentally using synchrotron radiation x-ray spectromicroscopy and occurs for a critical rotation angle of the nanomagnets, contingent upon the dipolar coupling determined by their separation in the lattice. Large-scale magnetic dipole simulations show that the point-dipole approximation fails to capture the correct AF–FM transition angle. However, excellent agreement with experimental data is obtained using a dumbbell-dipole model which better reflects the actual dipolar fields of the magnets. This model explains the coupling-dependence of the transition angle, another feature not captured by the point-dipole model. Our findings resolve a discrepancy between measurement and theory in previous work on "pinwheel" ASIs. Control of the AF–FM transition and this revised model open for improved design of magnetic order in nanostructured systems.

Artificial spin ice (ASI) systems[1] composed of single-domain nanomagnets, acting as macrospins, exhibit a wide range of exotic behaviors[2–5]. Recent work suggests that these systems are key to emergent device technologies such as physical reservoir computing[6, 7]. The interaction between the macrospins in an ASI is mediated by the stray fields of the individual magnets, creating a complex energy landscape sensitive to the exact shape of the elements and the geometric arrangement of the ensemble[3, 8]. With precise nanofabrication, this sensitivity enables effective tuning of magnetic order. Accurate modeling of the magnetic interactions in these dipolar-coupled metamaterials is essential to the analysis of emergent behavior, such as long-range magnetic order.

Previous research has established the predominance of long-range ferromagnetic (FM) order in a 45° "pinwheel" ASI[9], in contrast to the antiferromagnetically (AF) ordered ground state of the square ASI [1]. The FM-ordered pinwheel ASI is a metamaterial with several exotic emergent properties such as dynamic chirality[10], unique domain-wall topologies[11], and Heisenberg pseudo-exchange[12].

In this Letter, we investigate the AF to FM ordering transition we observe when going from a square to a pinwheel ASI. Specifically, we examine modifications of the square ASI by gradually rotating each nanomagnet on the square lattice from $\theta = 0°$ to $\theta = 45°$, see fig. 1. We observe the long-range magnetic order of these metamaterials using x-ray magnetic circular dichroism (XMCD) spectromicroscopy at the Advanced Light Source (ALS). A predominance of FM order is seen for the ASIs with a $\theta$ close to the 45° pinwheel configuration. We find a critical angle for the AF–FM transition dependent on the separation of the nanomagnetic elements, at odds with previous reports relying on a simple point-dipole model[9, 13]. For a more accurate representation of the stray fields, we invoke a dumbbell-dipole model, which is found to accurately capture the dependence of the AF–FM transition angle on the nanomagnet separation.

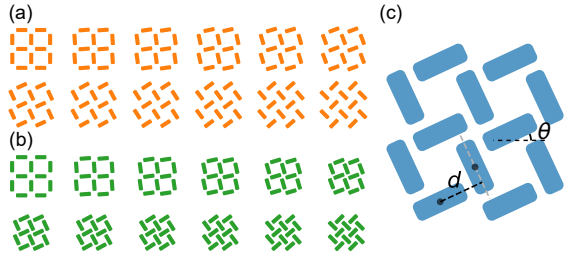


Figure 1. Geometric configuration of square-to-pinwheel structures. (a) Rotation of elements from the square $\theta = 0°$ ASI (top left) to the typical $\theta = 45°$ pinwheel ASI (bottom right). (b) The same series as in (a), but with the lattice compressed to compensate for decoupling. (c) Schematic showing the geometric parameters of the systems.

For this study, ensembles of $25 \times 25$ nanomagnets with lateral dimensions $l \times w = 220\,\text{nm} \times 80\,\text{nm}$ and thickness $t = 3\,\text{nm}$ were patterned using electron beam lithography (EBL) and lift-off. Each sample featured arrays with a range of different element rotations, $\theta$, corresponding to the schematics in fig. 1. The magnetic material was deposited by e-beam evaporation of permalloy ($Ni_{80}Fe_{20}$), followed by a 2 nm Al layer serving as an oxidation bar-

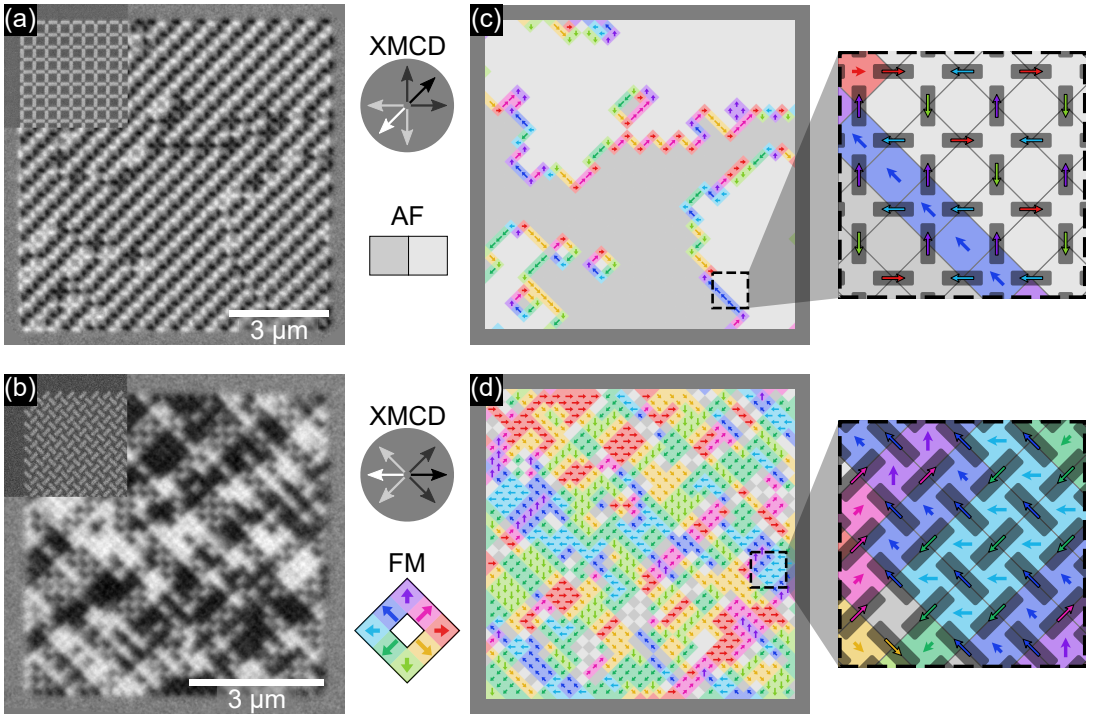


Figure 2. Relaxed states of a square ($\theta = 0°$) and pinwheel ($\theta = 45°$) ASI. (a) and (b) XMCD-PEEM images, with top left corner insets of a SEM image showing the rotation and shape of the nanomagnets. (c) and (d) Analyzed magnetization maps. Gray areas indicate the two possible phases of antiferromagnetically ordered regions. Colored regions are ferromagnetically ordered with a net magnetization as depicted in the legend. On the right, the relation between nanomagnet states and cell magnetization is illustrated. The length of the cell arrows correspond to the magnitude of the cell magnetization.

rier. The thickness of the magnetic film was chosen so that the ensembles could be easily thermalized *in situ*.

Rotation of the elements in this ASI system (see fig. 1(a)) alters the effective coupling between the nanomagnets due to the concentrated stray fields at their ends. Increasing the rotation angle $\theta$ on a fixed lattice will effectively decouple the elements. In this study, we reduce the lattice constant with increasing rotation angle $\theta$, in order to retain a strong interisland coupling, see fig. 1(b). We keep the parameter $d$, shown in fig. 1(c), fixed for all element rotations.

Modeling the AF–FM transition of a full array presents a computational challenge because of the large differences in scale between the internal magnetization of a single nanomagnet to the macroscopic scale of the nanomagnet array. In order to establish an accurate analytical stray-field model, the stray field of an isolated single nanomagnet is calculated using a micromagnetic simulator[14–16]. However, this micromagnetic approach is not feasible for the interactions of the full ensemble, due to the high computational cost, and an analytical representation of the stray field for a single nanomagnet is required. We use the micromagnetic framework mumax$^3$[14, 15] for the micromagnetic calculations and the Ubermag package[16] for comparison with analytically expressed fields. The relaxed magnetization in the absence of an external field was computed using micromagnetic simulation, and the stray field was calculated from the resulting magnetization texture. Each nanomagnet was modeled as a 220 nm × 80 nm rectangle with rounded corners and a thickness of 3 nm. The saturation magnetization was set at $M_S = 860\,\mathrm{kA\,m^{-1}}$ and the exchange stiffness at $A_{ex} = 1.3 \times 10^{-11}\,\mathrm{J\,m^{-1}}$[17]. A simulation mesh of 512 × 512 cells was adopted, where each cell had a side length of 2 nm, well below the exchange length $l_{ex} = \sqrt{2A_{ex}/\mu_0 M_S^2} \approx 5\,\mathrm{nm}$.

X-ray magnetic circular dichroism photoemission electron microscopy (XMCD-PEEM) was carried out on the PEEM3 beamline at ALS and was used to image the magnetic state of the ensembles. Prior to imaging at room temperature, the samples were brought to $T = 385\,\mathrm{K}$ to thermalize the system, so as to avoid quenched, meta-

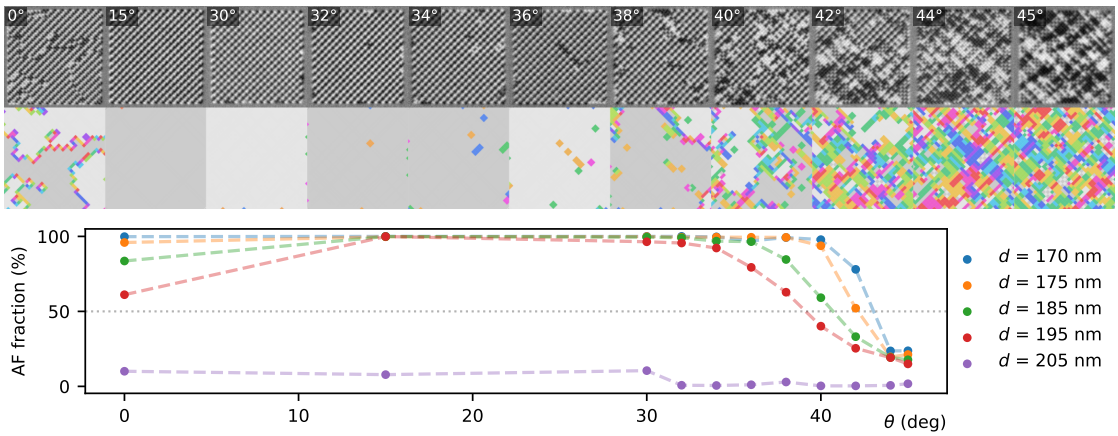


Figure 3. Measured fraction of antiferromagnetic Voronoi cells for the experimental ensembles. Five different separations $d$, kept constant across the rotation series from 0° to 45°, were investiaged. XMCD-PEEM images (top panel) show the PEEM images and graphical representation of the relaxed states for the $d = 185$ nm series.

stable, high-energy states. Complete thermalization was confirmed from the XMCD-PEEM images, showing no magnetic contrast, thus indicating full superparamagnetic behavior on the time scale of imaging. After thermalization, the sample was gradually cooled to room temperature, resulting in a relaxed state governed by the intrinsic dipolar interactions

Magnetic contrast images of the $\theta = 0°$ and $\theta = 45°$ ASIs are shown in fig. 2(a) and (b) with the typical AF and FM order, respectively. The magnetization of each nanomagnet is identified from the XMCD-PEEM images, with the help of machine learning, to create a graphical representation of the ensemble state. In fig. 2(c) and (d), we divide the ASI into so-called Voronoi cells (VCs), where each cell is assigned the net magnetization of four nearest neigbor nanomagnets. The $\theta = 0°$ ASI in fig. 2(c) shows extended regions with zero net magnetic moment, AF-ordered domains divided by domain walls of finite magnetic moment. In contrast, the $\theta = 45°$ ASI in fig. 2(d) displays numerous smaller FM-ordered regions with a net magnetic moment, mimicking the domains of a conventional ferromagnetic material. As these square and pinwheel ASI ensembles show distinct AF and FM order, respectively, this finding suggests successful relaxation of the arrays and sufficient dipolar magnetic coupling, to study their long-range order.

The main results of the measurement series, where the element rotation $\theta$ is gradually increased while $d$ is kept constant, are shown in fig. 3. (A complete overview of the XMCD-PEEM images discussed in this study is shown in the Supplemental Material[18].) The AF-ordered VCs dominate for all rotation angles below 30° irrespective of separation $d$, except for the decoupled $d > 200$ nm system. The transition to FM ordering starts at around $\theta = 39°$ for the ASI with $d = 195$ nm. The strongest coupled system, with $d = 170$ nm, exhibits the transition at $\theta = 43°$. The transition angle, $\theta_t$, is seen to decrease monotonically with reduced magnetic coupling. We note that the observed transition angles differ significantly from the $\theta_t \approx 35°$ reported in previous work[9, 13] where a simple point-dipole model was used.

An aberration from the expected complete AF ordering is found for $\theta = 0°$. For this element rotation, we find a multidomain AF ordering with FM ordered domain walls, which may be explained by reduced coupling across the nanomagnet corners.

In the AF-ordered square ASI, the next nearest parallel oriented nanomagnets feature antiparallel spin alignment. The change in long-range order from AF to FM with $\theta$ increasing from $0° \rightarrow 45°$, implies that for $\theta > \theta_t$ no neighbors align antiparallel. Specifically, the antiparallel magnetization alignment of the next nearest neighbors (a defining feature of AF order in the square ASI) will flip when their stray-field interaction energy favors parallel spin alignment. With this assumption, we can estimate the transition angle of an ensemble $\theta_t$ based on an analytical expression for the stray field.

With the ASI nanomagnets represented by point dipoles, the stray field is described by,

$$\vec{H}_{\text{point dipole}}(\vec{r}) = \frac{1}{4\pi}\left[\frac{3(\vec{m}_{\text{dip}} \cdot \vec{r})\vec{r}}{r^5} - \frac{\vec{m}_{\text{dip}}}{r^3}\right]. \quad (1)$$

where $\vec{m}_{\text{dip}}$ is the magnetic moment of a single nanomagnet and $\vec{r}$ is the distance vector from the point dipole. By calculating the angle at which the point-dipole interaction energy for the parallel neighbors changes sign, favoring parallel alignment, we determine a transition at

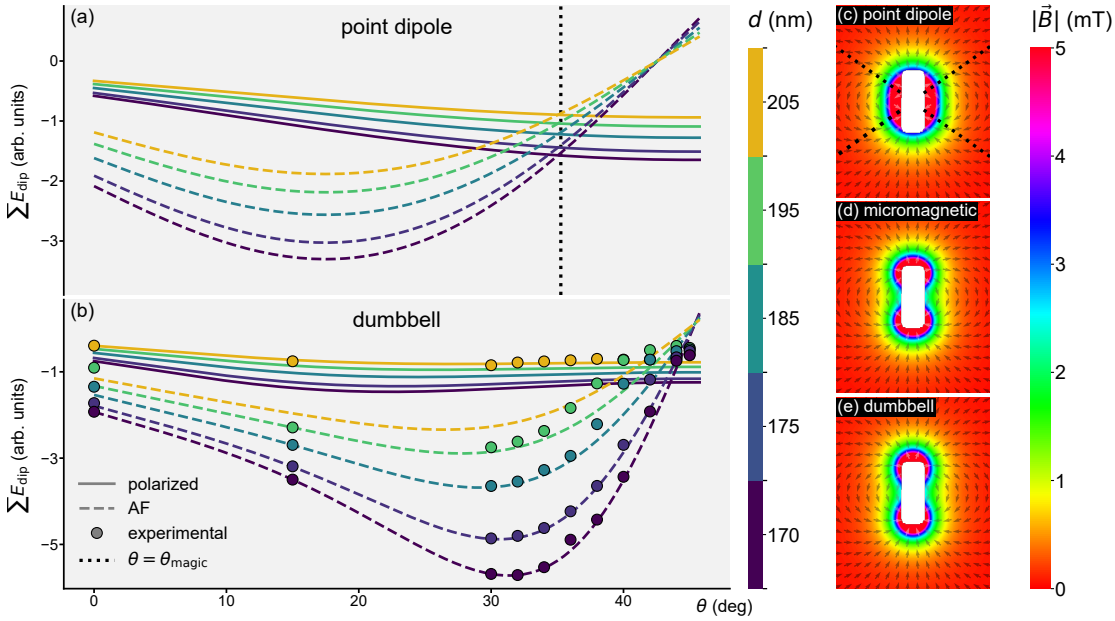


Figure 4. Ensemble state energies and nanomagnet stray-fields. Two example states are chosen when calculating the energies, a 100% AF-ordered state and a polarized state, i.e., a 100% FM-ordered state. (a) energies for the polarized and AF states, as calculated by the point-dipole model. (b) energies for the polarized, AF, and experimental states, as calculated by the dumbbell-dipole model. (c), (d), and (e) show the calculated stray fields for a single 220 nm × 80 nm × 3 nm nanomagnet (white rectangle), for the point-dipole model, the micromagnetic simulation, and the dumbbell-dipole model, respectively. The field strength color bar is truncated at 5 mT.

$\theta_t = \arctan(1/\sqrt{2}) \approx 35.3°$, commonly referred to as the 'magic angle', $\theta_{magic}$[19, 20].

When modeling the full ensembles in the point-dipole approximation, the AF–FM transition takes place at $\theta \approx 35.1°$, coinciding with $\theta_{magic}$, independent of the interisland coupling distance $d$. At this angle, the nature of the interaction energy for parallel neighbors changes. The minimum energy state shifts from "two aligned–two anti-aligned" to "all aligned" macrospins, as a result of the asymmetry between the $x$ and $y$ components of the point-dipole field (eq. (1)). This angle was cast as the critical angle for the transition between AF and FM order in previous work relying on Monte-Carlo simulations within the point-dipole model[9, 13]. However, the point-dipole approximation misses key features of the actual stray-field coupling as it fails to capture the observed variation in transition angle $\theta_t$ with nanomagnet separation.

The stray-fields of the point-dipole model and the micromagnetic simulation are shown in fig. 4(c) and (d), respectively. By comparison with the micromagnetic stray field, we find that a dumbbell-dipole model[21] captures the characteristics of the nanomagnet stray field better than the point-dipole model (see fig. 4(e)).

The dumbbell model emulates two magnetic charges, $\pm q_m$, separated by a distance $d_{dip}$ on the long-axis of the magnet. The magnitude of the total magnetic moment of a nanomagnet, $|\vec{m}_{dip}|$, is given by $M_S \cdot V$, where $M_S$ represents the saturation magnetization of the magnetic material comprising the nanomagnet and $V$ is the nanomagnet volume. The effective stray field of the single magnet at a position $\vec{r}$ relative to its center in this model is given by

$$\vec{H}_{dumbbell}(\vec{r}) = \vec{H}_{monopole}(\vec{r} - \vec{a}) - \vec{H}_{monopole}(\vec{r} + \vec{a}),$$
$$= \frac{q_m}{4\pi}\left[\frac{\vec{r} - \vec{a}}{|\vec{r} - \vec{a}|^3} - \frac{\vec{r} + \vec{a}}{|\vec{r} + \vec{a}|^3}\right], \quad (2)$$

where $\vec{a} = d_{dip} \cdot \hat{d}_{dip}/2$ is the distance vector separating the center of the magnet from its positive end. For the systems considered in this letter, we find that a naive, unoptimized dumbbell model of monopoles with $d_{dip} = l$ and $q_m \cdot d_{dip} = |\vec{m}_{dip}|$ is sufficient to match the experimental data.

The magnetic long-range order is evaluated by considering the total energies for the investigated ASI rotation angles $\theta = 0° \rightarrow 45°$ within the scope of the dumbbell-dipole model. We find AF and FM long-range

| $d$ (nm) | $E_{\mathrm{AF}} = E_{\mathrm{pol}}$ | | 50% AF |
|---|---|---|---|
| | point dipole | dumbbell | measured |
| 170 | 35.1° | 43.5° | 43.0° |
| 175 | 35.1° | 43.3° | 42.1° |
| 185 | 35.1° | 42.7° | 40.7° |
| 195 | 35.1° | 42.0° | 39.1° |
| 205 | 35.1° | 41.4° | N/A |

Table I. Transition angles $\theta_{\mathrm{t}}$, where the calculated energies of the antiferromagnetic state ($E_{\mathrm{AF}}$) is equal to the energy of the polarized state ($E_{\mathrm{pol}}$), for point-dipole and dumbbell-dipole models at different $d$ values. Also included: experimental transition angle taken to be the angle where the measured fraction of AF Voronoi cells is 50% (by interpolation).

order for angles close to 0° and 45°, respectively. Taking the transition angle $\theta_{\mathrm{t}}$ as the pinwheel rotation angle where the total energy of a FM state drops below the energy of the AF state, the energies of the ensemble for the point-dipole and dumbbell-dipole stray-field models, respectively, are shown in fig. 4a-b. The state energy is calculated by summation over all interactions for each of the experimentally observed states (circular data points), as well as for the fully polarized and AF-ordered states. The estimated transition angles from simulations and experimental results are compared in table I, with the simulated transition angles based on the FM and AF energy calculations. The measured angles are those where the AF fraction is interpolated at 50%.

From the stray-field maps in fig. 4(c-e), it is clear that the dumbbell model better captures the characteristic anisotropy and magnitude of the calculated stray fields of the micromagnetically modeled nanomagnet, in particular in the near-field region depicted here. Moreover, dumbbell-dipole model accurately captures the experimental observations with a transition angle $\theta_{\mathrm{t}}$ dependent on the intermagnet coupling. The AF–FM transition is observed for angles ranging from 39° to 43°, while simulations using this model indicate an AF–FM energy crossover for angles from 41.5° to 43.3°. This close correspondence underscores the advantage of using the dumbbell-dipole model for an accurate representation of the physical behavior of the system.

A notable exception to the AF order, observed at small angles $\theta$, is found for the $d = 205$ nm-series in fig. 3, where no experimental transition is found. The ensembles with this nanomagnet separation are all nearly polarized in the same direction. This finding suggests that dipolar coupling in this particular ensemble is too small to drive long-range order. The observed polarization may be due to a small stray field present during annealing inside the PEEM-3 microscope.

In conclusion, this study shows a transition from distinct AF order to pronounced FM order in a square-to-pinwheel artificial spin ice system. We find that the critical transition angle is dependent on the interisland coupling, a behavior not captured by the conventional point-dipole approximation. By introducing a dumbbell-dipole model, we achieve excellent agreement with experimental observations and micromagnetic simulations of the near-field interactions. We maintain that this model offers a suitable framework for simulation of a variety of nanomagnet shapes and textures. Our approach improves modeling of magnetic ordering in ASIs, which is key to fundamental research as well as technological applications.

This research used resources of the Advanced Light Source, which is a DOE Office of Science User Facilities under contract no. DE-AC02-05CH11231.

The Research Council of Norway is acknowledged for the support to the Norwegian Micro- and Nanofabrication Facility, NorFab, project no. 295864. The samples were fabricated at NTNU NanoLab.

This work was funded by the Norwegian Research Council through the IKTPLUSS project SOCRATES (Grant no. 270961) and by the EU FET-Open RIA project SpinENGINE (Grant no. 861618).

* anders.stromberg@ntnu.no

[1] R. F. Wang, C. Nisoli, R. S. Freitas, J. Li, W. McConville, B. J. Cooley, M. S. Lund, N. Samarth, C. Leighton, V. H. Crespi, and P. Schiffer, Nature **439**, 303 (2006).

[2] E. Mengotti, L. J. Heyderman, A. F. Rodríguez, F. Nolting, R. V. Hügli, and H.-B. Braun, Nature Physics **7**, 68 (2011).

[3] S. H. Skjærvø, C. H. Marrows, R. L. Stamps, and L. J. Heyderman, Nature Reviews Physics **2**, 13 (2020).

[4] A. May, M. Saccone, A. van den Berg, J. Askey, M. Hunt, and S. Ladak, Nature Communications **12**, 3217 (2021).

[5] E. Digernes, A. Strømberg, C. A. F. Vaz, A. Kleibert, J. K. Grepstad, and E. Folven, Applied Physics Letters **118**, 202404 (2021).

[6] J. H. Jensen, E. Folven, and G. Tufte, in *ALIFE 2018: The 2018 Conference on Artificial Life* (MIT Press, Tokyo, Japan, 2018) pp. 15–22.

[7] J. C. Gartside, K. D. Stenning, A. Vanstone, H. H. Holder, D. M. Arroo, T. Dion, F. Caravelli, H. Kurebayashi, and W. R. Branford, Nature Nanotechnology **17**, 460 (2022).

[8] E. Digernes, S. D. Slöetjes, A. Strømberg, A. D. Bang, F. K. Olsen, E. Arenholz, R. V. Chopdekar, J. K. Grepstad, and E. Folven, Physical Review Research **2**, 013222 (2020).

[9] R. Macêdo, G. M. Macauley, F. S. Nascimento, and R. L. Stamps, Physical Review B **98**, 014437 (2018).

[10] S. Gliga, G. Hrkac, C. Donnelly, J. Büchi, A. Kleibert, J. Cui, A. Farhan, E. Kirk, R. V. Chopdekar, Y. Masaki, N. S. Bingham, A. Scholl, R. L. Stamps, and L. J. Heyderman, Nature Materials **16**, 1106 (2017).

[11] Y. Li, G. W. Paterson, G. M. Macauley, F. S. Nascimento, C. Ferguson, S. A. Morley, M. C. Rosamond, E. H. Linfield, D. A. MacLaren, R. Macêdo, C. H. Marrows, S. McVitie, and R. L. Stamps, ACS Nano **13**, 2213

(2019).
[12] G. W. Paterson, G. M. Macauley, Y. Li, R. Macêdo, C. Ferguson, S. A. Morley, M. C. Rosamond, E. H. Linfield, C. H. Marrows, R. L. Stamps, and S. McVitie, Physical Review B **100**, 174410 (2019).
[13] G. M. Macauley, G. W. Paterson, Y. Li, R. Macêdo, S. McVitie, and R. L. Stamps, Physical Review B **101**, 144403 (2020).
[14] A. Vansteenkiste, J. Leliaert, M. Dvornik, M. Helsen, F. Garcia-Sanchez, and B. Van Waeyenberge, AIP Advances **4**, 107133 (2014).
[15] J. Leliaert, M. Dvornik, J. Mulkers, J. D. Clercq, M. V. Milošević, and B. V. Waeyenberge, Journal of Physics D: Applied Physics **51**, 123002 (2018).
[16] M. Beg, M. Lang, and H. Fangohr, IEEE Transactions on Magnetics **58**, 1 (2022).
[17] M. Maicas, R. Ranchal, C. Aroca, P. Sánchez, and E. López, The European Physical Journal B **62**, 267 (2008).
[18] See Supplemental Material at [URL will be inserted by publisher] for all XMCD-PEEM images with their graphical representation.
[19] S. J. Erickson, R. W. Prost, and M. E. Timins, Radiology **188**, 23 (1993).
[20] R. de Sousa, J. D. Delgado, and S. Das Sarma, Physical Review A **70**, 052304 (2004).
[21] C. Castelnovo, R. Moessner, and S. L. Sondhi, Nature **451**, 42 (2008).

# Supplemental Material: On the Antiferromagnetic-Ferromagnetic Phase Transition in Pinwheel Artificial Spin Ice

Anders Strømberg,[1,*] Einar Digernes,[1] Rajesh Vilas Chopdekar,[2] Jostein Grepstad,[1] and Erik Folven[1]

[1] *Department of Electronic Systems, Norwegian University of Science and Technology, Trondheim, Norway.*
[2] *Advanced Light Source, Lawrence Berkeley National Laboratory, Berkeley, CA, USA*

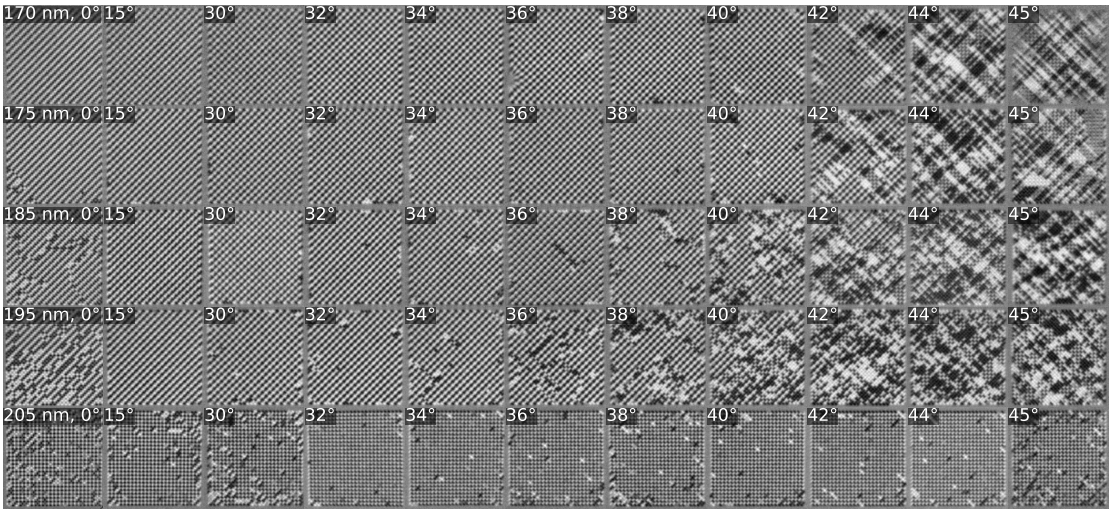


FIG. S1. XMCD-PEEM images of the ASI systems in their relaxed state. All separations $d$ and rotation angles $\theta$ included in this paper are displayed.

* anders.stromberg@ntnu.no

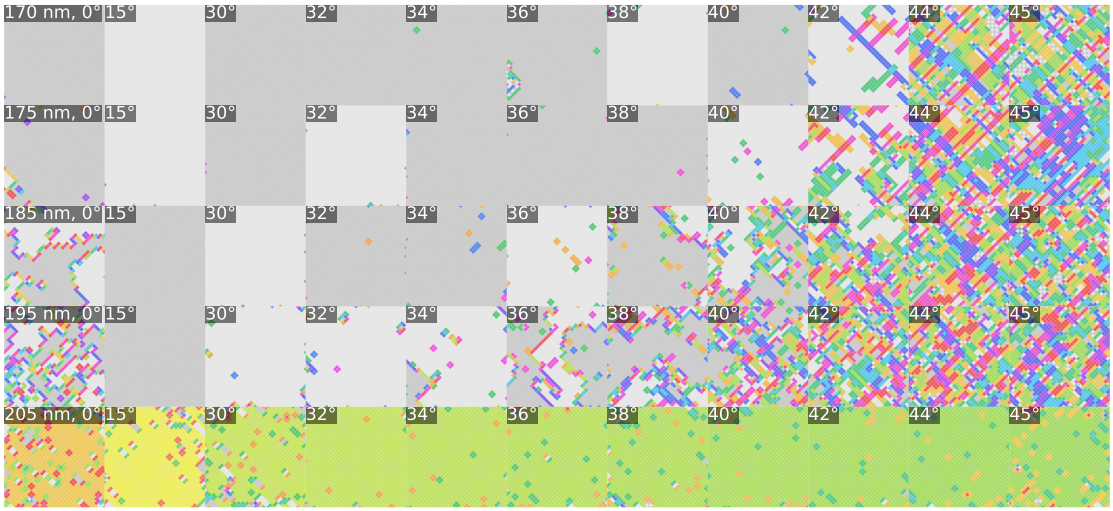


FIG. S2. Analyzed magnetization maps of the ASI systems in their relaxed state. All separations $d$ and rotation angles $\theta$ included in this paper are displayed. Gray domains indicate antiferromagnetically ordered regions, where each shade of gray indicates one of two possible antiferromagnetic phases. Colored regions are ferromagnetically ordered with a net magnetization as in the main paper.

nature communications

Article

https://doi.org/10.1038/s41467-024-45319-7

# Clocked dynamics in artificial spin ice

Received: 10 August 2023

Accepted: 19 January 2024

Published online: 01 February 2024

Check for updates

Johannes H. Jensen[1,4] ✉, Anders Strømberg[2,4] ✉, Ida Breivik[2], Arthur Penty[1], Miguel Angel Niño[3], Muhammad Waqas Khaliq[3], Michael Foerster[3], Gunnar Tufte[1] & Erik Folven[2]

Artificial spin ice (ASI) are nanomagnetic metamaterials with a wide range of emergent properties. Through local interactions, the magnetization of the nanomagnets self-organize into extended magnetic domains. However, controlling when, where and how domains change has proven difficult, yet is crucial for technological applications. Here, we introduce astroid clocking, which offers significant control of ASI dynamics in both time and space. Astroid clocking unlocks a discrete, step-wise and gradual dynamical process within the metamaterial. Notably, our method employs global fields to selectively manipulate local features within the ASI. Sequences of these clock fields drive domain dynamics. We demonstrate, experimentally and in simulations, how astroid clocking of pinwheel ASI enables ferromagnetic domains to be gradually grown or reversed at will. Richer dynamics arise when the clock protocol allows both growth and reversal to occur simultaneously. With astroid clocking, complex spatio-temporal behaviors of magnetic metamaterials become easily controllable with high fidelity.

Artificial spin ice (ASI) are systems of coupled nanomagnets arranged on a two-dimensional lattice. The nanomagnets are elongated, giving them two stable magnetization directions, thus behaving as artificial spins. Dipolar interactions give rise to a rich variety of emergent behavior, as determined by the ASI geometry[1–3], such as domains of long-range order. As this behavior can be probed directly, ASIs have attracted considerable interest as model systems for the study of fundamental physics[4,5]. More recently, ASIs have shown promise for device applications, such as substrates for computation[6–12].

Controlling when, where and how ASIs change state is instrumental to both fundamental research and applications. Control of the state evolution would enable an experimenter to access a richer variety of emergent ASI phenomena. Furthermore, such control will be key in applications such as neuromorphic computing, where the functionality is derived directly from the evolving magnetic state of the ASI. However, external control of emergent ASI dynamics has so far proven difficult.

External fields are the primary method used to perturb ASIs in a controlled manner. Various global field protocols have been employed. For example, a cycled in-plane field is often used to characterize magnetization reversal[1,13–21]. Another approach is to use a rotating field with slowly decreasing amplitude to effectively anneal the ASI to a low energy state[22–29]. While there are variations of these simple field protocols, more complex protocols are largely unexplored.

These approaches use field strength to modulate ASI behavior, which will typically result in uncontrolled avalanches of activity[30]. An in-plane field will advance ASI state primarily when the strength of the field is increased beyond the coercivity of the array, and is highly dependent on field resolution[19,25,29]. Consequently, the discrete spin flip dynamics in the ASI are sudden and hard to control.

In this work, we introduce a field protocol scheme called astroid clocking, which produces fundamentally different spin flip dynamics. In contrast to previous approaches, astroid clocking unlocks a discrete, step-wise and gradual evolution of spin states. The method offers significant control and understanding of the dynamical process in both time and space. Key to the method is exploiting the shape and orientation of the nanomagnet switching astroids, together with their dipolar coupling. Specific field angles can then be established to

[1]Department of Computer Science, Norwegian University of Science and Technology, Trondheim, Norway. [2]Department of Electronic Systems, Norwegian University of Science and Technology, Trondheim, Norway. [3]ALBA Synchrotron Light Facility, Carrer de la Llum 2 – 26, Cerdanyola del Vallés 08290 Barcelona, Spain. [4]These authors contributed equally: Johannes H. Jensen, Anders Strømberg. ✉e-mail: johannes.jensen@ntnu.no; anders.stromberg@ntnu.no

selectively address emergent local features within the ensemble, such as domain boundaries. A clock protocol which pulses fields in an alternate fashion at these angles, is then used for driving the intrinsic dynamics of the ASI. Distinctively, the clock pulses maintain a constant field amplitude.

In the context of nanomagnetic logic, Nomura et al.[31] demonstrated how the shape of two overlapping Stoner-Wohlfarth astroids can be exploited to preferentially switch nanomagnets in a 1D shift register. Astroid clocking extends and generalizes this concept to 2D nanomagnet arrays, and non-elliptical nanomagnets with different astroid shapes. We show how astroid clocking reveals the intrinsic dynamics of coupled nanomagnetic systems.

In this study we consider the pinwheel ASI system, but stress that astroid clocking is readily applicable to other coupled nanomagnetic systems as well. We have, for instance, obtained promising results with both square and kagome ASI in simulations. Here, we demonstrate and analyse how ferromagnetic domains in pinwheel ASI can be gradually grown and reversed at will using astroid clocking. Different clock protocols are explored, giving rise to distinct properties of the spin flip dynamics.

## Results

### Astroid clocking

Pinwheel ASI[2,19,32] consists of nanomagnets arranged on two interleaved square sublattices, as shown in Fig. 1a. In this study, the magnets in the two sublattices $L_a$ and $L_b$ are rotated +45° and −45° with respect to the array edges. The sublattice and magnetization of the magnets are indicated by their color: magnets in sublattice $L_a$ are orange or blue, while magnets in sublattice $L_b$ are pink or green. For brevity, we will refer to magnet state by these four colors.

Pinwheel ASI favors a ferromagnetic ordering, with emergent domains of coherent magnetization. Figure 1a shows the four possible domain directions: rightwards (orange/pink), leftwards (blue/green) and so on. The ferromagnetic domains are separated by domain walls, which are slightly less energetically favorable[32].

The switching threshold of a nanomagnet depends on the field angle, and can be approximated by the Stoner-Wohlfarth astroid. Figure 1b shows the switching astroids for the two orientations of stadium-shaped magnets in pinwheel ASI[33]. A magnet will switch state if the total field acting on it lies outside the astroid boundary, and the field is directed against the current magnetization. Note that we use the term *switching astroid* to refer to any angle-dependent threshold curve, also when its shape deviates significantly from the ideal geometric astroid shape. The compound shape in Fig. 1b resembles an ideal astroid, but is in fact two overlapping, highly distorted astroids (solid and dashed outlines).

Nanomagnet shape largely determines the shape of the astroid. Stadium-shaped nanomagnets, commonly used in ASI, have a switching astroid with 2-fold rotational symmetry[33]. This is in contrast to classical Stoner-Wohlfarth astroids that display 4-fold rotational symmetry derived for elliptical nanomagnets[34].

Switching astroids that break the 4-fold rotational symmetry, can be exploited to selectively address nanomagnets that are rotated 90° with respect to each other. If the total field lies within the shaded regions in Fig. 1b, only the nanomagnets in the corresponding sublattice will be able to switch. A field in the orange/blue shaded regions will address only the magnets in sublattice $L_a$, while a field in the pink/green regions will address only magnets in $L_b$. Furthermore, each region promotes a specific magnet state within each sublattice, e.g., a field in the blue shaded region promotes blue magnets by switching orange magnets.

In this study, we define two *bipolar clocks* A and B along the +22° and −22° axes, respectively. As shown in Fig. 1b, each clock consists of a positive and negative *clock field* of magnitude $H$ along the clock axis. The four arrows in Fig. 1b are colored according to the magnet states they promote, e.g., the $\mathbf{H}_A$ field only promotes orange magnets.

The dipolar fields $\mathbf{h}_{\mathrm{dip}}$ from neighboring magnets may either promote or prevent switching. If the dipolar fields are directed out of (into) the astroid, they effectively promote (prevent) switching. A clock field can thus selectively address a subset of a sublattice,

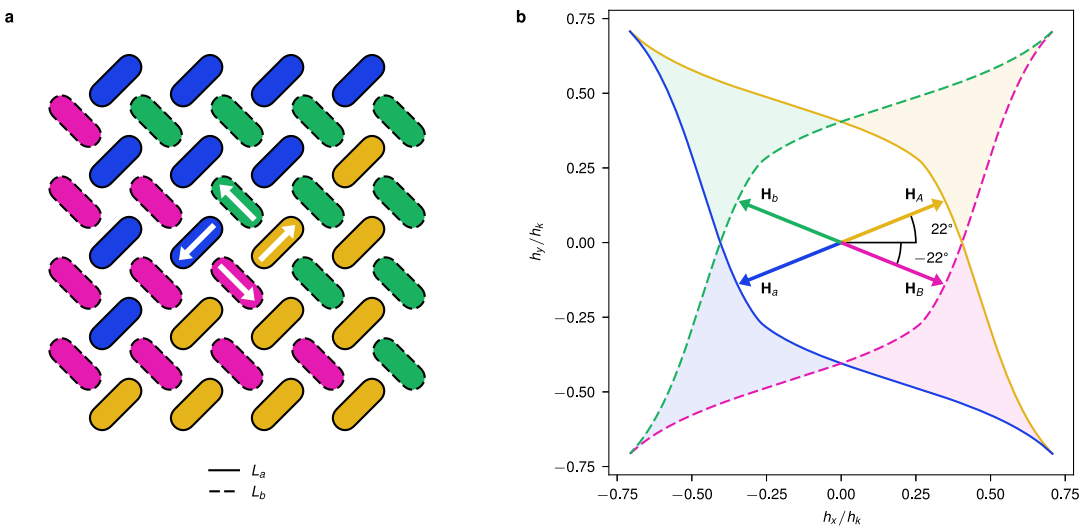


**Fig. 1 | Astroid clocking of pinwheel ASI. a** a small 4 × 4 pinwheel ASI, formed by two interleaved sublattices $L_a$ (solid outline) and $L_b$ (dashed outline) with magnets oriented at +45° and −45°, respectively. Colors correspond to magnetization direction as indicated by the white center arrows. The magnetic state shows the four possible ferromagnetic domains of pinwheel ASI, where the net magnetization forms a counter-clockwise magnetic flux closure pattern. **b** The two switching astroids for the magnets in sublattice $L_a$ (solid lines) and $L_b$ (dashed lines), along with the four clock fields, $\mathbf{H}_A$, $\mathbf{H}_B$, $\mathbf{H}_a$, and $\mathbf{H}_b$. The astroid edges are colored according to the magnet state which is promoted when fields cross the edge. Similarly, the colored regions correspond to fields that exclusively promote a magnet state within a sublattice. Astroid axes are normalized with respect to the hard axis switching threshold, $h_k$.

https://doi.org/10.1038/s41467-024-45319-7

depending on the state of the ensemble. The clock angles ±22° are selected to allow the dipolar fields to have a large influence on switching, using a field strength $H$ close to the switching threshold. However, a precise angle is not crucial and the method tolerates a wide range of clock angles. Our system tolerates clock angles in the range 10° to 35°, and field strengths accurate to within 3 mT to 4 mT. Other clock angles, such as ±45°, would appear to allow for similar switching selectivity. However, as we shall see later, the influence of dipolar fields renders these angles unsuitable.

Figure 2 illustrates astroid clocking, where a *clock pulse* is defined as ramping a clock field from zero to $H$ and down to zero again. The ramping speed is much slower than the timescale of nanomagnetic switching. A *clock protocol* is a specific sequence of clock pulses. For example, *AB* clocking consists of repeated alternating clock pulses of *A* and *B*. We define a *clock cycle* as a single sequence of the clock pulses in a protocol, e.g., an *aAbB* clock cycle is the sequence of four pulses (*a*, *A*, *b*, *B*). A *unipolar* clock protocol exclusively employs one polarity of each clock, while a *bipolar* clock protocol employs both polarities.

## Unipolar clocking

First, we explore the spin flip dynamics of pinwheel ASI when subject to the unipolar clock protocols *AB* and *ab*. The 50 × 50 pinwheel ASI (5100 magnets) is initialized with a small rightwards (orange/pink) domain in the center of an otherwise leftwards polarized (blue/green) array. Figure 3 (1) shows a closeup of the initial state.

Figure 3 (2–8) shows the state evolution of the array subject to *AB* clocking, obtained from flatspin simulations (see Methods). As expected, the *A* pulse selectively switches magnets in sublattice $L_a$ from blue to orange, while the *B* pulse selectively switches magnets in sublattice $L_b$ from green to pink.

Interestingly, the particular magnets that switch are the ones along the domain wall. As a result, the inner (leftwards) domain grows

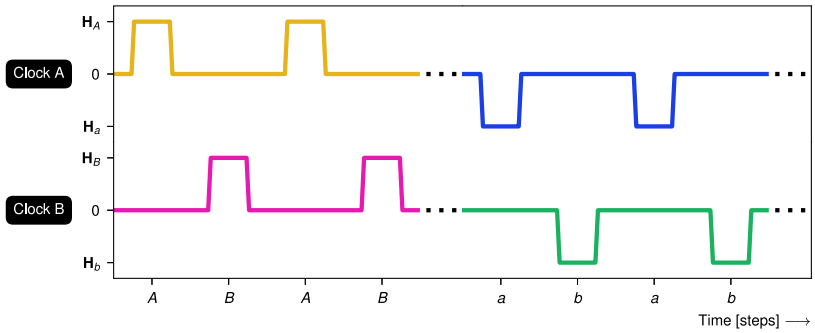


**Fig. 2 | Clock diagram of astroid clocking.** Clock protocols are defined by sequences of clock pulses. The clock diagram shows *AB* clocking (alternating pulses of the positive clock fields $\mathbf{H}_A$ and $\mathbf{H}_B$) followed by *ab* clocking (alternating pulses of the negative clock fields $\mathbf{H}_a$ and $\mathbf{H}_b$).

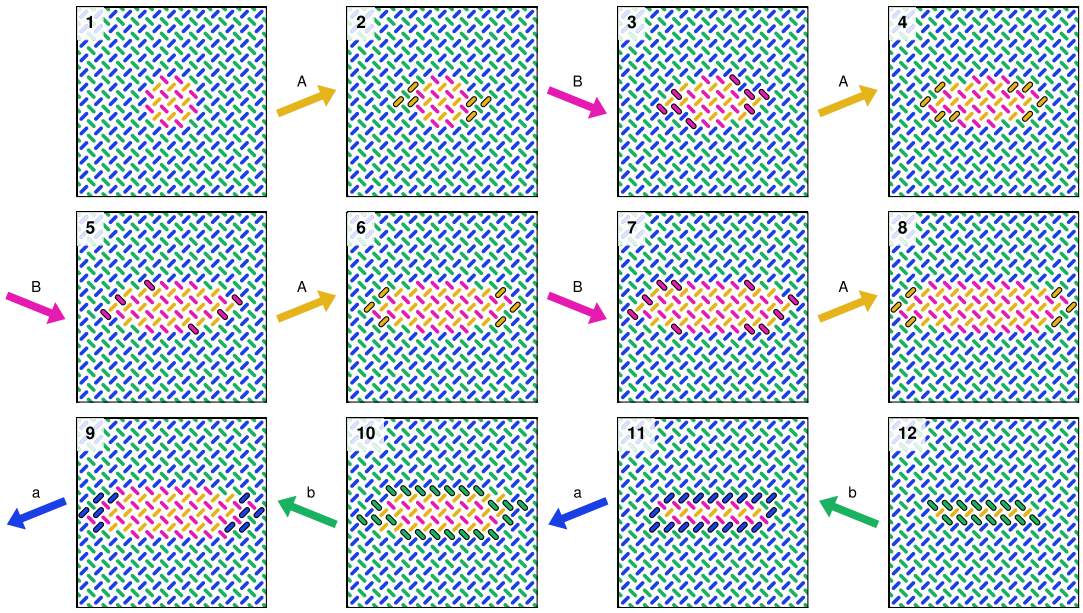


**Fig. 3 | Simulation of unipolar astroid clocking of pinwheel ASI in flatspin.** Each snapshot shows a zoomed-in view of the 50 × 50 nanomagnet system, at different points during a clock protocol. (1) shows the initial state, a small orange/pink (rightwards) domain in the center of an otherwise polarized blue/green (leftwards) array. (2–8) show the state during *AB* clocking, resulting in gradual domain growth. (9–12) show the subsequent states during *ab* clocking, resulting in gradual domain reversal. Magnets that change state between snapshots are highlighted with a solid black outline.

https://doi.org/10.1038/s41467-024-45319-7

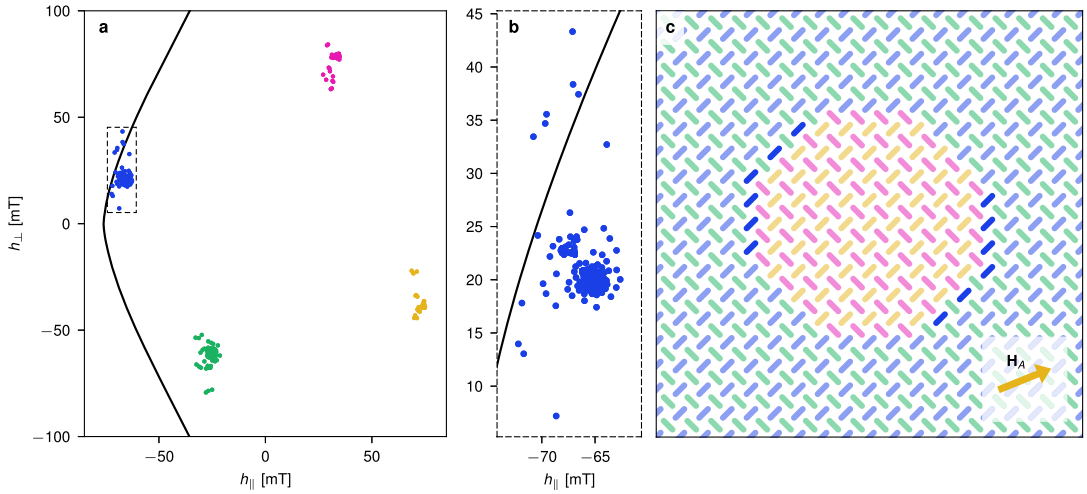


**Fig. 4 | Astroid clusters showing relative locations of all the magnets within their respective switching astroids.** The plots show clusters and astroid (black curve) for the pinwheel system shown in (**c**), when subject to the clock field $\mathbf{H}_A$. **a** astroid cluster plot where each dot represents the total field $\mathbf{h}_i = \mathbf{H}_A + \mathbf{h}_{\text{dip}}^{(i)}$ experienced by a magnet $i$, projected onto its parallel ($h_\parallel$) and perpendicular ($h_\perp$) axis. Note that the positive direction of the parallel component is with respect to the magnetization direction of each nanomagnet. The colors in the plot correspond to magnet state. Note that the astroid plot shows location relative to each magnet's own switching threshold, e.g., orange magnets are far from switching as they are aligned with $\mathbf{H}_A$. **b** closeup of the blue cluster, revealing a sub-group of blue magnets that lie outside the switching astroid and are eligible for switching. These magnets are highlighted in **c**, and are all found to lie along the vertical and +45° domain walls. The data is obtained from flatspin simulations.

gradually over time, with only a thin layer of the domain advancing after each clock pulse. The growth is monotonic and step-wise, driven by the clock pulses.

A curious property is that the domain grows mainly in the horizontal direction. In Fig. 3 (2–8), the magnets along the vertical domain walls are the only ones to switch. If the growing domain reaches the edges of the array, the direction of growth changes and becomes vertical, eventually filling the entire array (Fig. 5).

Inverting the clock pulses (*ab* clocking), will instead grow the outer (blue/green) domain and consequently shrink (reverse) the inner (orange/pink) domain. As can be seen in Fig. 3 (9–12), domain reversal from (8) proceeds in both vertical and horizontal directions, resulting in reversal of the inner domain in fewer clock cycles compared to growth. Hence there is an apparent asymmetry in the direction of domain growth and reversal.

## Growth and reversal mechanism

To understand the mechanism behind the domain growth and reversal, we consider the larger domain shown in Fig. 4c, subject to $\mathbf{H}_A$. In Fig. 4a, we plot the relative locations of all the magnets within their respective switching astroids. Each dot represents the total field $\mathbf{h}_i = \mathbf{H}_A + \mathbf{h}_{\text{dip}}^{(i)}$ experienced by a magnet $i$ in its local frame of reference. There are four clusters of dots within the astroids, corresponding to the four magnet colors, where only the blue magnets are close to switching.

The internal structure of each astroid cluster is a result of the nanomagnet dipolar coupling, and a direct consequence of the ASI geometry. In the absence of dipolar fields, each cluster collapses into a single point. The dipolar fields add complex structure to the clusters, with sub-groups corresponding to different subsets of magnets within the ASI. For a detailed analysis of neighbor contributions, see Supplementary Discussion.

The inset shown in Fig. 4b reveals the structure of the blue cluster. Notice there are a few blue dots that lie outside the astroid, corresponding to magnets that are eligible for switching, which are highlighted in Fig. 4c. Evidently, the switchable magnets all lie along the vertical and +45° domain walls.

When a magnet switches, its location within the astroid jumps to the cluster of opposite spin, e.g., a blue magnet switches to the orange state. In addition, neighboring magnets will see a change in the dipolar fields, causing movement within their respective clusters. In this way, the switching of a magnet may enable future switching in neighboring magnets, either during the current or a future clock pulse. As can be seen in Fig. 4b, the mechanism hinges on both the internal structure of the astroid clusters, and at what angle the cluster approaches the astroid edge. Clock angles around 22° work because they allow only magnets along certain domain walls to switch. Other clock angles, such as ±45°, are unsuitable since large parts of the astroid cluster will lie close to the astroid edge (at $h_\perp = 0$), resulting in avalanches of switching within a sublattice.

The observed horizontal domain growth can now be explained from the internal structure of the astroid clusters. We have seen that magnets along certain types of domain walls can be selectively switched under an applied clock field. Switching the blue (highlighted in Fig. 4c) magnets along these domain walls reverses their dipolar fields, which affects the structure of the green cluster. Consequently, green magnets that are part of the domain walls will approach the switching astroid. When the $\mathbf{H}_B$ field is subsequently applied, these magnets will be outside the astroid and hence switch. As this cycle repeats, the result is an apparent horizontal domain growth emerging from the dipolar interactions and clock fields.

During domain reversal, both horizontal and vertical domain walls take part in the process. As a result, reversal requires fewer clock cycles compared to growth. During reversal, the switchable magnets lie along both the horizontal, vertical and −45° domain walls (Supplementary Fig. 1).

We find that the horizontal domain wall movement, particular to reversal, is dependent on the curvature of the reversing domain. If the horizontal domain wall is surrounded by a blue/green domain on three sides, there is a stronger dipolar "push" towards the astroid

https://doi.org/10.1038/s41467-024-45319-7

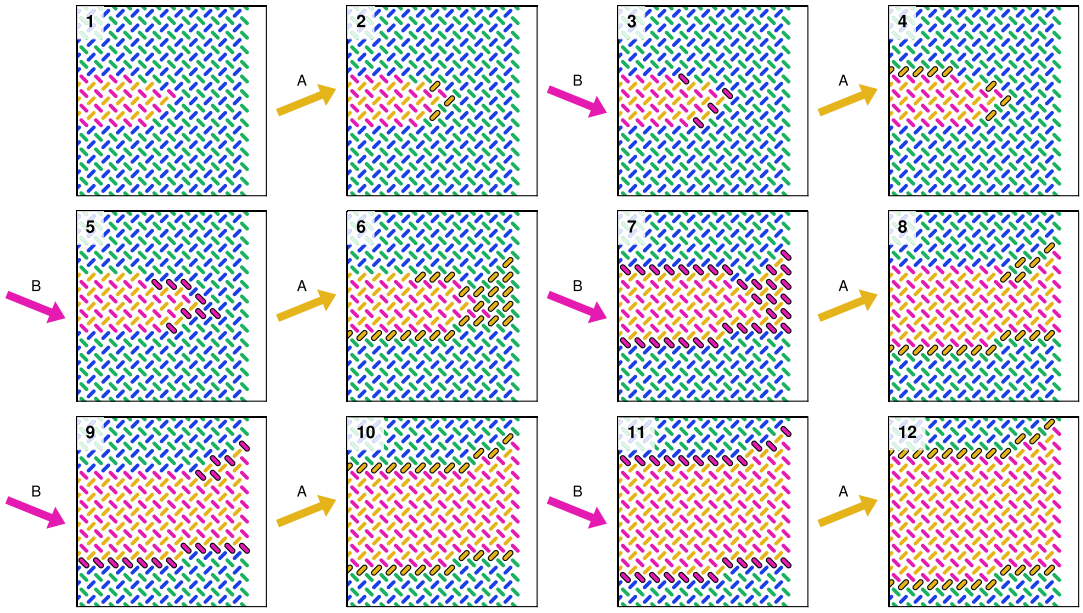


**Fig. 5 | Unipolar *AB* clocking of an orange/pink (rightwards) domain as it reaches the edge of the array.** There is an apparent transition from horizontal to vertical domain growth (5–6). Vertical growth proceeds by avalanches of spin flips, starting at the bottom-left and top-right corners of the domain at the array edge. Magnets that change state between snapshots are highlighted by a solid black outline.

edge. As such, domain shape plays a crucial role in the reversal process.

When a domain grows to reach the edges of the array, there is an apparent transition from horizontal to vertical growth (Fig. 5). We find that vertical growth proceeds by avalanches along the domain wall, starting at the bottom-left and top-right corners of the domain, close to the array edges.

## Experimental growth and reversal

Next, we demonstrate astroid clocking of pinwheel ASI experimentally. Samples are imaged with x-ray magnetic circular dichroism photoemission electron microscopy (XMCD-PEEM), with an in-situ vector magnet to perform astroid clocking. See Methods for details.

After polarizing all magnets in the leftwards direction (bright contrast), we perform steps of *AB* clocking, imaging in-between each clock cycle. Figure 6a shows total magnetization of the ensemble, obtained from the XMCD-PEEM images, which increases in a stable, monotonic fashion. Selected experiment snapshots are shown in Fig. 6b. Snapshots (1–3) show that domains nucleate at the vertical edges then predominantly expand horizontally.

Domain formation at the vertical array edges can be explained by the dipolar field-driven mechanism behind *AB* clocking. While domain nucleation along horizontal edges is possible, continued growth primarily occurs in the horizontal direction, preventing further expansion of horizontal edge nucleated domains. Spatial control of nucleation could be achieved, e.g., by changing the edge geometry, introducing internal edges or reducing the coercivity of selected magnets.

In any physical ASI system, the nanomagnets will exhibit a range of intrinsic switching thresholds, a *disorder*, due to imperfections and microscopic variations of material composition. Disorder affects both domain shape and growth dynamics, as evident in our experimental results. Compared to the idealized simulations, domains appear more organic, with distinct features such as jagged edges, slanted domain walls, and sporadic holes. In terms of dynamics, some domain borders get stuck for several clock cycles, while others advance more than one step during a single cycle (see Fig. 7).

By introducing disorder to the simulations (see Methods), we obtain results that more closely resemble the experiment. The magnetization curve and snapshots from simulations with disorder are included in Fig. 6. Notice how the simulated snapshots show organic-looking domains that resemble the domains of the experiment.

After growth, we apply the reversal clock protocol, *ab* clocking. For each *ab* clock cycle, the magnetization reduces sharply, with domains shrinking more rapidly compared to the increase during growth. Comparing snapshot (3) and (4) of Fig. 6b, it is clear that the domains shrink in both vertical and horizontal directions.

Next, we conduct a control experiment to verify that simply repeating a clock pulse *A* or *B* does not result in domain growth. After re-initializing the system, we apply several pulses of *A*, then several pulses of *B*, imaging after each pulse. As seen in the last part of Fig. 6a, only the first application of *A* or *B* results in growth (see also Supplementary Fig. 2). Growth progresses only when the type of clock pulse is changed, which confirms that the alternating pattern of *A* and *B* is what drives the observed domain growth.

These experiments affirm the viability of astroid clocking in the face of experimental sensitivities (as low as $<1$ mT from Fig. 4) and potential impediments such as fabrication imperfections, temperature effects, and material degradation. While unstable individual magnets and inaccuracies in the image analysis induce some noise, it is negligible compared to the effect of astroid clocking. Experimental astroid clocking is surprisingly robust, demonstrating that it is possible to precisely control the spin flip dynamics of ASIs using global fields.

## Bipolar clocking

In bipolar clocking, each clock may be pulsed in both polarities. We consider two clock protocols illustrated in Fig. 8, namely *aAbB* and its inverse, *AaBb* clocking. In contrast to unipolar clocking, the magnetic fields in these bipolar clock protocols are balanced, i.e., the sum of all

https://doi.org/10.1038/s41467-024-45319-7

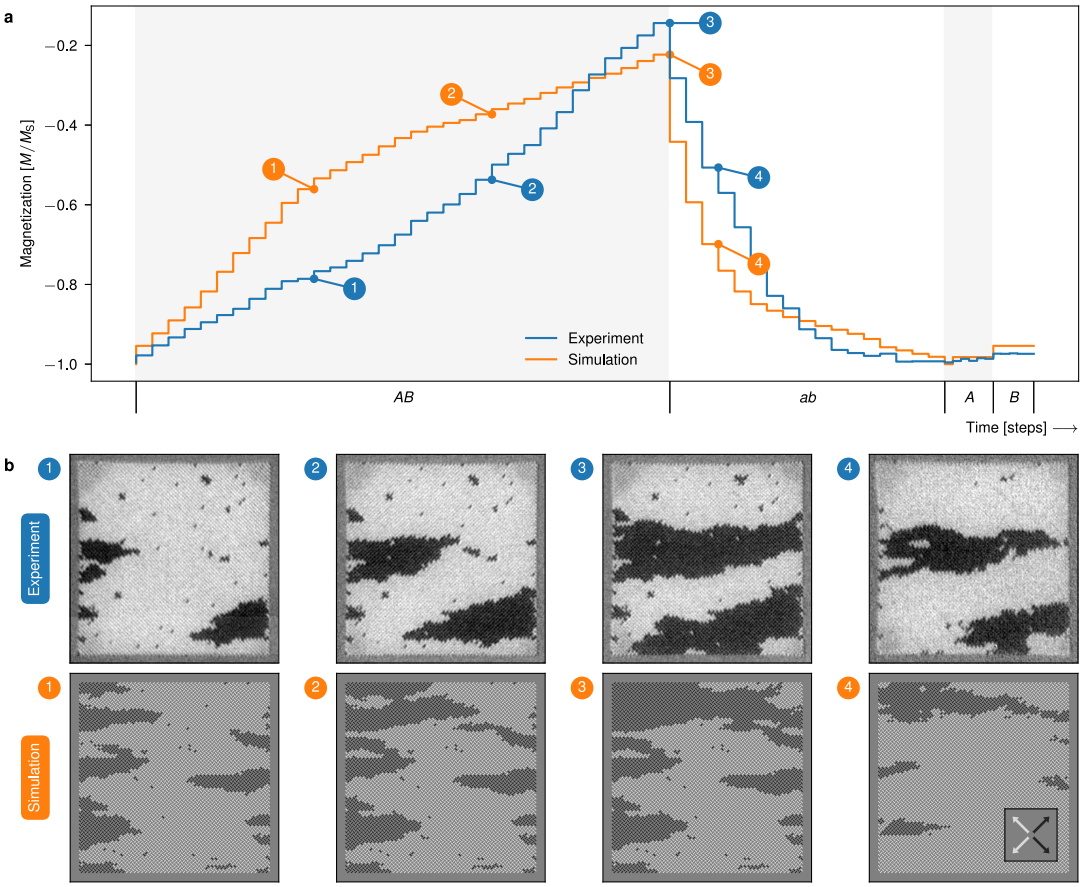


**Fig. 6 | Results of growth and reversal with unipolar clock protocols, and control experiment. a** total magnetization of the ensembles subject to the different clock protocols. The timeline indicates clock time, labeled by the clock protocol. During *AB* clocking, the ensembles undergo growth and hence an increase in magnetization. The second phase, *ab* clocking, quickly reverses domains and total magnetization. The control experiment, consisting of separate *A* and *B* clock sequences, show no development of the domains. **b** magnetic image snapshots (experiemental XMCD-PEEM images and flatspin simulated XMCD-PEEM contrast images) of the ensembles at the specified points in time. The depicted ensembles are approximately 12.5 µm × 12.5 µm (50 × 50 pinwheel ASI, 5100 magnets). All XMCD-PEEM images are available in Fig. 7 and Supplementary Fig. 2. Videos of the experiment and simulation are provided in Supplementary Movies 1 and 2.

clock fields is zero. One might then expect that this results in a net zero magnetization change.

On the contrary, bipolar clocking also results in domain growth and reversal, and a net change in magnetization. Figure 9a plots the total magnetization of pinwheel ASI subject to bipolar clocking. As can be seen, *aAbB* clocking results in net domain growth, while *AaBb* clocking results in domain reversal.

In contrast to unipolar clocking, bipolar clocking can also induce morphological changes to the growing domains. As a result of the bipolarity of the clock pulses, domains are now able to both grow and shrink within the same clock cycle. In the experiment snapshots of Fig. 9b, we observe growth from (1) to (2), followed by a clear change in domain morphology from (2) to (3), and further growth between (3) to (4). In simulations, we can observe the step-wise details of simultaneous growth and morphology changes, as shown in the zoomed in snapshots. Inverting the clock protocol (*AaBb* clocking) results in domain reversal.

The deciding factor for growth or reversal is the polarity of the last clock pulse at the transition between the two clocks. Each clock in *aAbB* clocking, for example, ends on the positive polarity at the transition (*aA* and *bB*), resulting in growth of the rightwards (orange/pink) domains.

Within a bipolar clock cycle, there is an apparent competition between growth and reversal. Some domain wall configurations result in net domain growth (others in net reversal), in a "one step back, two steps forward" process (see Supplementary Discussion). In this way, a domain may grow horizontally and reverse vertically, thereby gradually changing shape over time (see Fig. 10). While the balance between growth and reversal can be delicate, there is a clear trend for the clock protocols explored here, namely growth for *aAbB*, and reversal for *AaBb*.

Compared to unipolar clocking, the dynamics in bipolar clocked pinwheel ASIs are more varied and complex. While there is a gradual net domain growth, the activity can intermittently spike and linger, depending on the particular state of the ensemble (see Supplementary Movies 3 and 4). Bipolar clocking hence unlocks a wide variety of complex dynamic behavior in pinwheel ASI, while at the same time offering considerable control by choice of clock protocol.

https://doi.org/10.1038/s41467-024-45319-7

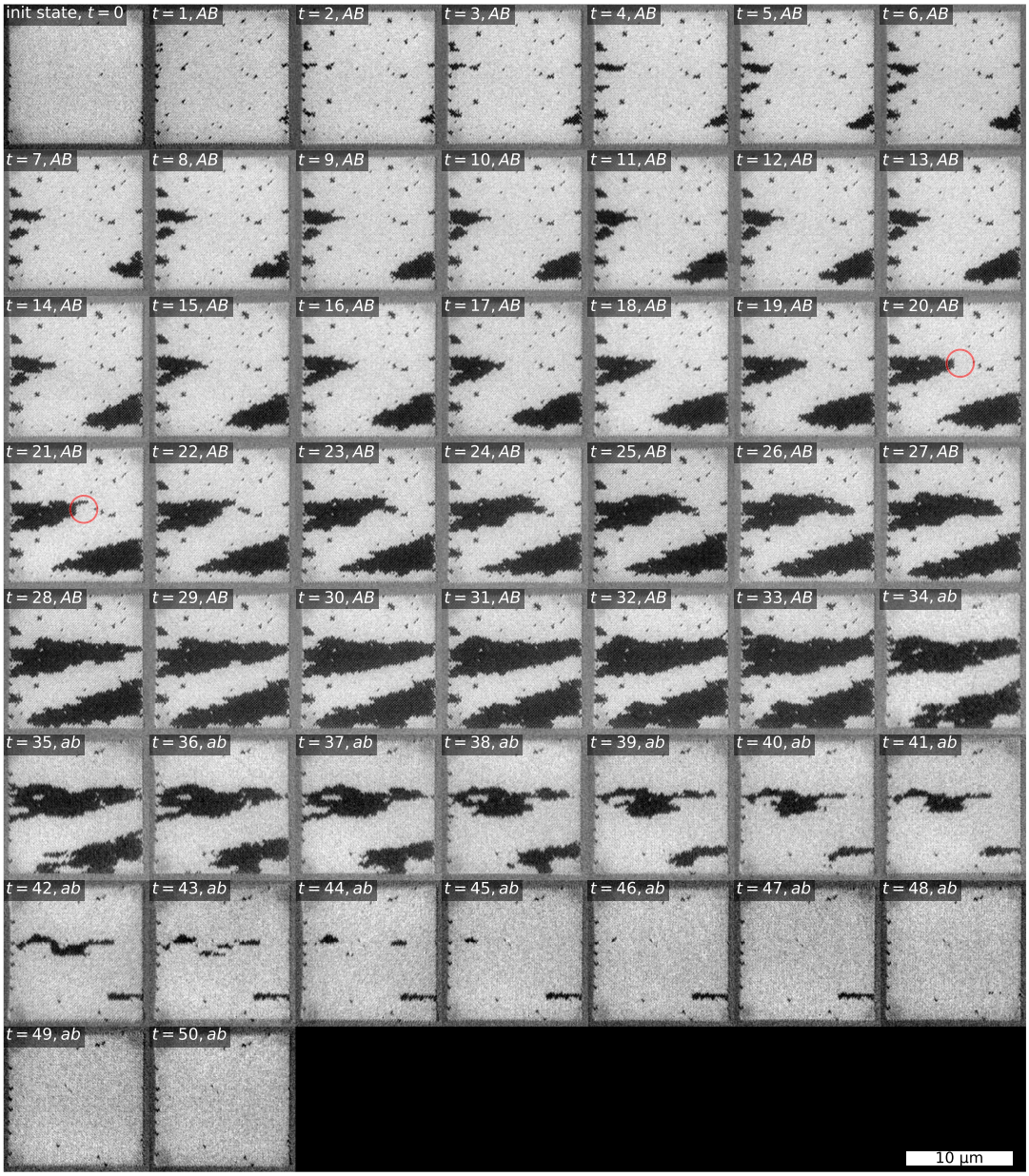


**Fig. 7 | XMCD-PEEM images of all steps from the relevant unipolar clock protocol series.** Time starts at $t = 0$, and is incremented by 1 for each clock step, with clock pulses indicated by the labels. The black (rightwards) domains grow with application of *AB* clocking, and quickly reverses with *ab* clocking. Red circle highlights: The short, vertical domain wall terminating the black domain in the center region of snapshot $t = 20$ exemplifies both avalanching domain growth and a stuck domain wall. In snapshot $t = 21$ the top part of the domain wall has progressed in an avalanche to form a finger extension of the domain, while the bottom part of the domain wall remains as before.

## Discussion

We have introduced astroid clocking, a scheme for field-driven evolution in nanomagnetic metamaterials. The method exploits the shape and orientation of the nanomagnet switching astroids, combined with local dipolar coupling, to selectively address subsets of the nanomagnets. Importantly, astroid clocking only requires global fields, yet offers a remarkable degree of control at the microscopic scale. Pulsing specific fields in sequence results in clocked dynamics that are both gradual and discrete in time. Furthermore, considerable control of the dynamics is available through choice of clock protocol.

This work demonstrates how astroid clocking can be used to control the growth and reversal of ferromagnetic domains in pinwheel ASI.

https://doi.org/10.1038/s41467-024-45319-7

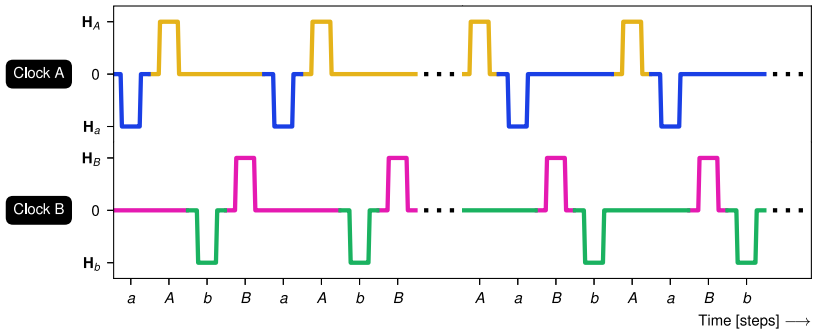


**Fig. 8 | Clock diagram of bipolar *aAbB* clocking followed by its inverse, *AaBb* clocking.** Bipolar clocking employs both positive and negative clock pulses.

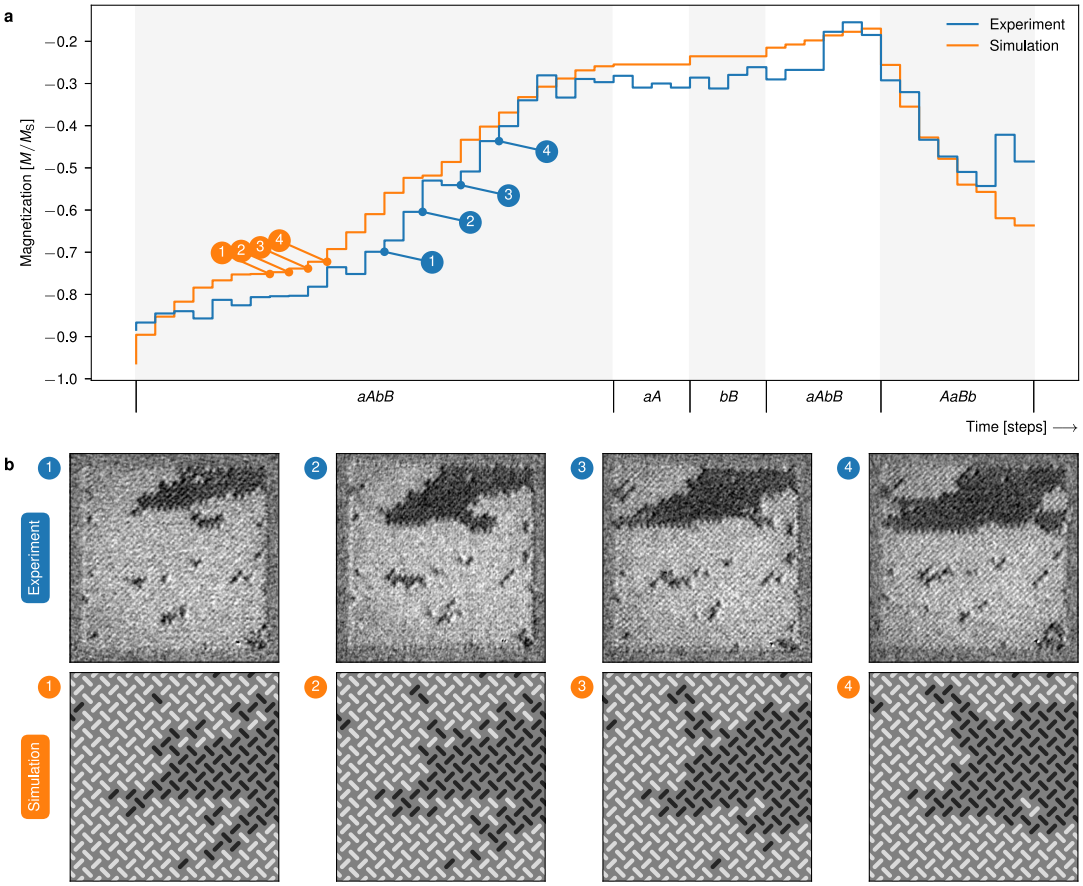


**Fig. 9 | Results of growth and reversal with bipolar clocking, and control experiment. a** total magnetization of the ensembles subject to the different bipolar clock protocols. The timeline indicates clock time, labeled by the clock protocol. During the first phase, *AaBb* clocking, the ensembles undergo domain growth and increase in magnetization. The controls, *aA* clocking and *bB* clocking, show no net growth. Further growth (*aAbB* clocking) and reversal (*AaBb* clocking) occur after the controls. **b** magnetic image snapshots of the experimental ensemble, and zoomed in views of the flatspin simulated ensemble, at the specified points in time. The growing domains change morphology during the clock protocol. All XMCD-PEEM images are available in Supplementary Fig. 3. Videos of the experiment and simulation are provided in Supplementary Movies 3 and 4.

https://doi.org/10.1038/s41467-024-45319-7

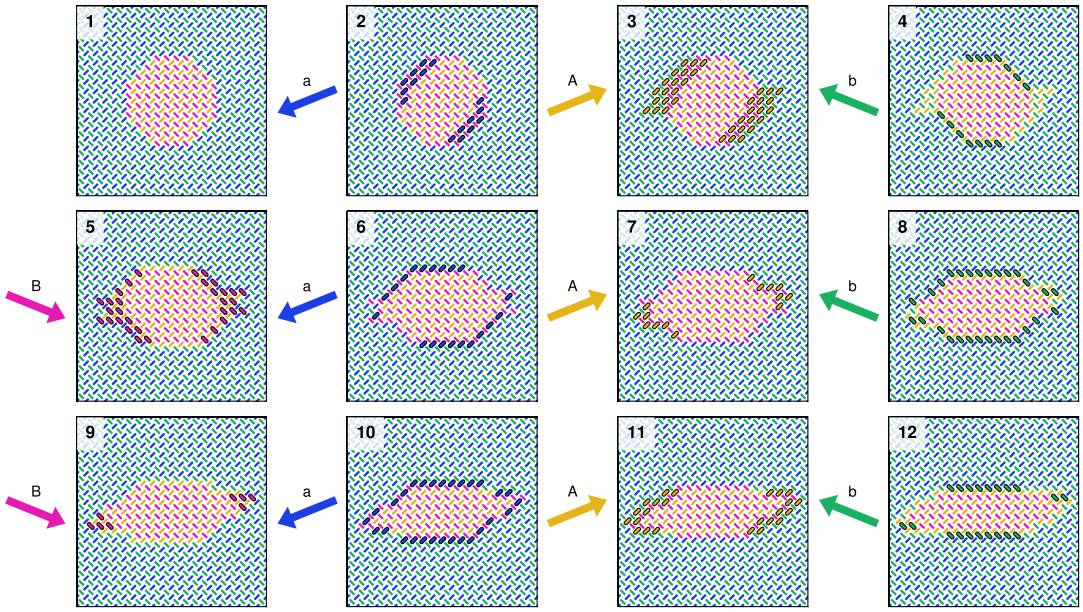


**Fig. 10 | Bipolar *aAbB* clocking of pinwheel ASI.** Each snapshot shows a zoomed-in view of a 50 × 50 system, at different points during a clock protocol. (1) shows the initial state, an orange/pink (rightwards) domain in the center of an otherwise polarized blue/green (leftwards) array. (2–12) show the state during *aAbB* clocking, with simultaneous domain growth (horizontally) and reversal (vertically). As a result the domain gradually changes morphology over time. Magnets that change state between snapshots are highlighted by a solid black outline.

In this system, unipolar clocking results in monotonic domain growth or reversal, while bipolar clocking adds more complex dynamics that include changes to domain morphology. The level of control far exceeds what is possible with conventional ferromagnetic materials, and what has previously been achieved in magnetic metamaterials.

The principles of astroid clocking are not limited to pinwheel ASI, and are pertinent to a range of coupled nanomagnetic systems. Preliminary simulation results of both square and kagome ASI strongly suggest the method is widely applicable. However, further work is needed to establish the most suitable protocols for these geometries. Exploring the clocked dynamics of established and future nanomagnetic metamaterials is an exciting research direction. Notably, with a large variety of possible clock protocols, the method opens for the exploration of new and exotic metamaterial states.

Astroid clocking offers significant control of ASI dynamics in both time and space, enabling the full richness of emergent behavior to be explored and exploited. The method enables entirely new directions in both fundamental and applied metamaterial research, and is key for the development of nanomagnetic technology.

## Methods

### Sample fabrication details

The samples are arrays of permalloy nanomagnets fabricated in pinwheel ASI geometries on a silicon substrate. The resist mixture, 1:2 CSAR 62:anisole, is spin-coated onto the substrate at 4000 rpm, achieving a thickness of ~100 nm. Following coating, samples are soft baked at 150 °C for 1 min. The desired patterns, arrays of 220 nm × 80 nm stadium shaped nanomagnets in 30 × 30 and 50 × 50 pinwheel geometries, with lattice spacing 255 nm and 248 nm, respectively, are then exposed using the Elionix ELS-G100 EBL system. Samples are post-exposure baked at 150 °C for 1 min. The patterned resist is developed using AR600-546 for 1 min, rinsed with isopropanol, and nitrogen dried. Permalloy ($Ni_{0.79}Fe_{0.21}$) is deposited to a thickness of 25 nm via electron beam evaporation using a Pfeiffer Vacuum Classic 500 system, and capped with a 2 nm aluminium layer. Finally, the samples undergo ultrasound-assisted lift-off using a dedicated stripper (AR600-71), leaving behind the patterned permalloy nanomagnets. Post-fabrication, the precision and quality of the fabricated nanomagnet arrays are inspected using scanning electron microscopy (SEM). This SEM inspection confirmed that the permalloy nanomagnets are properly formed, free-standing, and without significant defects.

### XMCD-PEEM and clocking procedure

Experimentally realized clocking of fabricated ASIs is carried out under magnetic microscopy inspection. We use a photoemission electron microscope with x-ray magnetic circular dichroism (XMCD-PEEM) for magnetic contrast to observe single magnet states of the ASI ensembles[35]. An in-plane, bi-axial quadrupole magnet with two pairs of coils and a split 2D-yoke provides astroid clocking fields[36]. The signal at the Fe $L_3$ edge is exploited for ferromagnetic XMCD contrast.

The orientation of the ASI ensembles, applied magnetic fields, and XMCD contrast is carefully selected. Samples are mounted with top and bottom ensemble edges parallel to the synchrotron light, with each nanomagnetic element oriented ±45° to the light. This orientation guarantees balanced magnetic contrast for nanomagnets of both sublattices $L_a$ and $L_b$. The in-plane field direction is given relative to the incoming x-ray illumination, with angle values increasing counter-clockwise. Consequently, the field directions and ensemble orientation align with the illustration in Fig. 1, with an added light axis (providing magnetic contrast) parallel to the $h_x$-axis.

The general experimental procedure is to initialize the ASI system, then apply clock protocols interspersed with magnetic imaging. We initialize the system by applying a strong, polarizing magnetic field

(72 mT along 180°), followed by two smaller fields, (18 mT along 0° and 3.5 mT along 180°) to demagnetize the yoke. For the bipolar clocking, however, the polarizing field strength is 82 mT. The difference in field strength is due to observed differences in the ensemble coercivity. Successful initialization is confirmed by imaging a fully polarized ensemble (fully bright contrast (leftwards), as in snapshot $t = 0$ of Fig. 7) and the absence of remaining image translation in the PEEM (indicating a demagnetized yoke).

After initialization, we perform steps of the clock protocols by alternating the application of clock pulses *A*, *B*, *a* or *b*. Each *step* of a clock protocol comprises at least one *clock pulse* (ramping the applied field to $\mathbf{H}_i$, holding the max field value, ramping down to zero applied field), and a magnetic contrast image acquisition. The value of $H$ that defines the $\mathbf{H}_i$ magnitudes is 62 mT for the unipolar clocking, and 75 mT for the bipolar clocking. After applying the first cycle of a clock protocol, before imaging, we shift the image, using the electron microscope optics, to re-center the ensemble, compensating for a small remanent magnetization in the yoke. We carry out multiple cycles, each consisting of applying clock pulses and capturing an image, while maintaining the same image shift throughout.

In addition to the growth and reversal protocols, we conduct a control experiment by applying repeated clock pulses of *A* and *B* separately.

### flatspin simulations

Numerical simulations were done using flatspin, a large-scale ASI simulator[33]. flatspin approximates each nanomagnet as a point dipole with position $\mathbf{r}_i$ and orientation $\theta_i$. Each dipole then has two possible magnetization directions along $\theta_i$, i.e., a binary macrospin $s_i \in \{-1, +1\}$.

Each spin $i$ is influenced by a total field $\mathbf{h}_i = \mathbf{h}_{\text{dip}}^{(i)} + \mathbf{h}_{\text{ext}}^{(i)} + \mathbf{h}_{\text{th}}^{(i)}$, where $\mathbf{h}_{\text{dip}}^{(i)}$ is the total dipolar field from neighboring magnets, $\mathbf{h}_{\text{ext}}^{(i)}$ is a global or local external field, and $\mathbf{h}_{\text{th}}^{(i)}$ is a stochastic magnetic field representing thermal fluctuations in each magnetic element. The total dipolar field is given by the magnetic dipole-dipole interaction,

$$\mathbf{h}_{\text{dip}}^{(i)} = \alpha \sum_{j \neq i} \frac{3\mathbf{r}_{ij}(\mathbf{m}_j \cdot \mathbf{r}_{ij})}{|\mathbf{r}_{ij}|^5} - \frac{\mathbf{m}_j}{|\mathbf{r}_{ij}|^3}, \tag{1}$$

where $\mathbf{r}_{ij} = \mathbf{r}_i - \mathbf{r}_j$ is the distance vector from spin $i$ to $j$, and $\alpha$ scales the dipolar coupling strength between spins. The coupling strength $\alpha$ is given by $\alpha = \frac{\mu_0 M}{4\pi a^3}$, where $a$ is the lattice spacing, $M$ is the net magnetic moment of a single magnet, and $\mu_0$ is the vacuum permeability.

Nanomagnet switching (magnetization reversal) occurs if the total field is directed against the current magnetization $\mathbf{m}_i$ and the magnitude of the field exceeds the coercive field $h_c$. flatspin employs a generalized Stoner-Wohlfarth model, where $h_c$ depends on the angle of the total field $\mathbf{h}_i$ with respect to the magnet orientation. Associated with each magnet is a switching astroid, which describes $h_c$ in terms of the parallel (easy axis) and perpendicular (hard axis) component of the total field, $\mathbf{h}_\parallel$ and $\mathbf{h}_\perp$. The shape of the switching astroid is described by the equation

$$\left(\frac{h_\parallel}{bh_k}\right)^{2/\gamma} + \left(\frac{h_\perp}{ch_k}\right)^{2/\beta} = 1, \tag{2}$$

where $h_k$ denotes the coercive field along the hard axis. The parameters $b$, $c$, $\beta$, and $\gamma$ adjust the shape of the astroid: $b$ and $c$ define the height and width, respectively, while $\beta$ and $\gamma$ adjust the curvature of the astroid at the easy and hard axis, respectively. Astroid parameters are typically tuned to obtain a shape that agrees with results from micromagnetic simulations.

Fabrication imperfections are modelled as variation in the coercive fields $h_k^{(i)}$, which are sampled from a normal distribution $\mathcal{N}(h_k, \sigma)$, where $\sigma = k_{\text{disorder}} \cdot h_k$ and $k_{\text{disorder}}$ is a user-defined parameter.

Dynamics are modeled using a deterministic single spin flip strategy. At each simulation step, the total magnetic field $\mathbf{h}_i$ is calculated. Next, we obtain a list of spins that may flip, according to the switching astroid. Finally, the spin which is furthest outside its switching astroid is flipped. The dipolar fields are recalculated after every spin flip, and the above process is repeated until there are no more flippable spins. This relaxation process is performed with constant external and thermal fields.

In this work, a global external field is used ($\mathbf{h}_{\text{ext}}^{(i)} = \mathbf{h}_{\text{ext}}$), and thermal fluctuations are assumed to be negligible ($\mathbf{h}_{\text{th}}^{(i)} = 0$).

The coupling strength $\alpha = 0.0013$ was estimated to match the experimental results from the 50 × 50 fabricated pinwheel sample. The value of $\alpha = 0.0013$ is lower than predicted by theory ($\alpha \approx 0.0025$), which is likely due to demagnetizing oxidation of the permalloy. A partially oxidized nanomagnet will have a reduced magnetic moment and a smaller effective size as the surface layer is no longer ferromagnetic. The smaller 30 × 30 sample used in Fig. 9 had a slightly larger magnet spacing and $\alpha = 0.0012$ was used in this case.

For the simulation studies, a field strength $H = 76.5$ mT and no disorder was used. Simulations accompanying the experimental results used a slightly lower field strength of $H = 75.8$ mT for Fig. 6 and $H = 75.9$ mT for Fig. 9.

Switching parameters were estimated from micromagnetic simulations of a 220 nm × 80 nm × 25 nm stadium magnet using mumax[37], namely $h_k = 0.2$ T, $b = 0.38$, $c = 1$, $\beta = 1.3$, and $\gamma = 3.6$. Other parameters include $k_{\text{disorder}} = 4\%$ and a neighbor distance of 10.

## Data availability

The XMCD-PEEM data, XAS data, and simulation results generated in this study have been deposited in the Zenodo database under accession code 10044134 at https://zenodo.org/doi/10.5281/zenodo.10044133.

## Code availability

Numerical simulations were performed using the open-source flatspin simulator (https://flatspin.gitlab.io/). Simulation details are included as part of the dataset (see above).

## References


1. Ladak, S., Read, D. E., Perkins, G. K., Cohen, L. F. & Branford, W. R. Direct observation of magnetic monopole defects in an artificial spin-ice system. *Nat. Phys.* **6**, 359–363 (2010).
2. Gliga, S. et al. Emergent dynamic chirality in a thermally driven artificial spin ratchet. *Nat. Mater.* **16**, 1106–1111 (2017).
3. Sendetskyi, O. et al. Continuous magnetic phase transition in artificial square ice. *Phys. Rev. B* **99**, 214430 (2019).
4. Heyderman, L. J. & Stamps, R. L. Artificial ferroic systems: novel functionality from structure, interactions and dynamics. *J. Phys.: Condensed Matter* **25**, 363201 (2013).
5. Skjærvø, S. H., Marrows, C. H., Stamps, R. L. & Heyderman, L. J. Advances in artificial spin ice. *Nat. Rev. Phys.* **2**, 13–28 (2020).
6. Jensen, J. H., Folven, E., Tufte, G. Computation in artificial spin ice. In: ALIFE 2018: The 2018 Conference on Artificial Life, pp. 15–22. MIT Press, Tokyo, Japan https://doi.org/10.1162/isal_a_00011 (2018).
7. Arava, H. et al. Engineering relaxation pathways in building blocks of artificial spin ice for computation. *Phys. Rev. Appl.* **11**, 054086 (2019).
8. Gypens, P., Leliaert, J. & Van Waeyenberge, B. Balanced magnetic logic gates in a kagome spin ice. *Phys. Rev. Appl.* **9**, 034004 (2018).
9. Jensen, J. H. & Tufte, G. Reservoir Computing in Artificial Spin Ice. In: ALIFE 2020: The 2020 Conference on Artificial Life, pp. 376–383. MIT Press, Online https://doi.org/10.1162/isal_a_00268 (2020).
10. Hon, K. et al. Numerical simulation of artificial spin ice for reservoir computing. *Appl. Phys. Express* **14**, 033001 (2021).
11. Kaffash, M. T., Lendinez, S. & Jungfleisch, M. B. Nanomagnonics with artificial spin ice. *Phys. Lett. A* **402**, 127364 (2021).

12. Gartside, J. C. et al. Reconfigurable training and reservoir computing in an artificial spin-vortex ice via spin-wave fingerprinting. *Nat. Nanotechnol.* **17**, 460–469 (2022).
13. Schumann, A., Sothmann, B., Szary, P. & Zabel, H. Charge ordering of magnetic dipoles in artificial honeycomb patterns. *Appl. Phys. Lett.* **97**, 022509 (2010).
14. Mengotti, E. et al. Real-space observation of emergent magnetic monopoles and associated Dirac strings in artificial kagome spin ice. *Nat. Phys.* **7**, 68–74 (2011).
15. Morgan, J. P., Stein, A., Langridge, S. & Marrows, C. H. Magnetic reversal of an artificial square ice: dipolar correlation and charge ordering. *N J. Phys.* **13**, 105002 (2011).
16. Pollard, S. D., Volkov, V. & Zhu, Y. Propagation of magnetic charge monopoles and Dirac flux strings in an artificial spin-ice lattice. *Phys. Rev. B* **85**, 180402 (2012).
17. León, A. Heavy and light monopoles in magnetic reversion in artificial spin ice. *Curr. Appl. Phys.* **13**, 2014–2018 (2013).
18. Gilbert, I. et al. Direct visualization of memory effects in artificial spin ice. *Phys. Rev. B* **92**, 104417 (2015).
19. Li, Y. et al. Superferromagnetism and domain-wall topologies in artificial "pinwheel" spin ice. *ACS Nano* **13**, 2213–2222 (2019).
20. Bingham, N. S. et al. Collective ferromagnetism of artificial square spin ice. *Phys. Rev. Lett.* **129**, 067201 (2022).
21. Popy, R. B., Frank, J. & Stamps, R. L. Magnetic field driven dynamics in twisted bilayer artificial spin ice at superlattice angles. *J. Appl. Phys.* **132**, 133902 (2022).
22. Wang, R. F. et al. Artificial 'spin ice' in a geometrically frustrated lattice of nanoscale ferromagnetic islands. *Nature* **439**, 303–306 (2006).
23. Wang, R. F. et al. Demagnetization protocols for frustrated interacting nanomagnet arrays. *J. Appl. Phys.* **101**, 09–104 (2007).
24. Nisoli, C. et al. Ground state lost but degeneracy found: the effective thermodynamics of artificial spin ice. *Phys. Rev. Lett.* **98**, 1–4 (2007).
25. Ke, X. et al. Energy minimization and ac demagnetization in a nanomagnet array. *Phys. Rev. Lett.* **101**, 037205 (2008).
26. Qi, Y., Brintlinger, T. & Cumings, J. Direct observation of the ice rule in an artificial kagome spin ice. *Phys. Rev. B* **77**, 094418 (2008).
27. Nisoli, C. et al. Effective temperature in an interacting vertex system: theory and experiment on artificial spin ice. *Phys. Rev. Lett.* **105**, 047205 (2010).
28. Phatak, C., Petford-Long, A. K., Heinonen, O., Tanase, M. & De Graef, M. Nanoscale structure of the magnetic induction at monopole defects in artificial spin-ice lattices. *Phys. Rev. B* **83**, 174431 (2011).
29. Perrin, Y., Canals, B. & Rougemaille, N. Extensive degeneracy, Coulomb phase and magnetic monopoles in artificial square ice. *Nature* **540**, 410–413 (2016).
30. Bingham, N. S. et al. Experimental realization of the 1D random field ising model. *Phys. Rev. Lett.* **127**, 207203 (2021).
31. Nomura, H., Yoshioka, N., Miura, S. & Nakatani, R. Controlling operation timing and data flow direction between nanomagnet logic elements with spatially uniform clock fields. *Appl. Phys. Exp.* **10**, 123004 (2017).
32. Macêdo, R., Macauley, G. M., Nascimento, F. S. & Stamps, R. L. Apparent ferromagnetism in the pinwheel artificial spin ice. *Phys. Rev. B* **98**, 014437 (2018).
33. Jensen, J. H. et al. flatspin: a large-scale artificial spin ice simulator. *Phys. Rev. B* **106**, 064408 (2022).
34. Tannous, C. & Gieraltowski, J. The Stoner–Wohlfarth model of ferromagnetism. *Eur. J. Phys.* **29**, 475–487 (2008).
35. Aballe, L., Foerster, M., Pellegrin, E., Nicolas, J. & Ferrer, S. The ALBA spectroscopic LEEM-PEEM experimental station: layout and performance. *J. Synchrotron Radiat.* **22**, 745–752 (2015).
36. Foerster, M. et al. Custom sample environments at the ALBA XPEEM. *Ultramicroscopy* **171**, 63–69 (2016).
37. Vansteenkiste, A. et al. The design and verification of MuMax3. *AIP Adv.* **4**, 107133 (2014).
38. Själander, M., Jahre, M., Tufte, G., & Reissmann, N. EPIC: an energy-efficient, high-performance GPGPU computing research infrastructure. Preprint at arXiv:1912.05848 (2019) arxiv:1912.05848.

## Acknowledgements

These experiments were performed at the CIRCE beamline at ALBA Synchrotron with the collaboration of ALBA staff. This work was funded by the Norwegian Research Council through the IKTPLUSS project SOCRATES (Grant no. 270961) and the TEKNOKONVERGENS project SPrINTER (Grant No. 331821), and by the EU FET-Open RIA project SpinENGINE (Grant No. 861618). The Research Council of Norway is acknowledged for the support to the Norwegian Micro- and Nano-Fabrication Facility, NorFab, project number 295864. Simulations were executed on the NTNU EPIC compute cluster[38]. M.A.N., M.F. and M.W.K. acknowledge funding from MCIN through grant number PID2021-122980OB-C54 and M.W.K. also acknowledges support through Marie Sklodowska-Curie grant agreement No. 754397 (DOC-FAM) from EU Horizon 2020.

## Author contributions

J.H.J. and A.S. conceived and designed the study and contributed equally to this work. J.H.J. did the initial discovery in simulations and did the simulation study. A.S. fabricated the samples. A.S. led the XMCD-PEEM experiments and J.H.J., I.B., A.P., G.T. and E.F. contributed to these measurements. M.F., M.A.N. and M.W.K. provided support during XMCD-PEEM measurements and PEEM vector magnet operation. A.S. and J.H.J. performed the analysis with assistance from I.B. and A.P. E.F. and G.T. oversaw the project and provided feedback and direction throughout. J.H.J. and A.S. wrote the manuscript with input from all authors.

## Funding

Open access funding provided by Norwegian University of Science and Technology.

## Competing interests

The authors declare no competing interests.

## Additional information

**Supplementary information** The online version contains supplementary material available at https://doi.org/10.1038/s41467-024-45319-7.

**Correspondence** and requests for materials should be addressed to Johannes H. Jensen or Anders Strømberg.

**Peer review information** *Nature Communications* thanks Will Branford, and the other, anonymous, reviewer(s) for their contribution to the peer review of this work. A peer review file is available.

# Supplementary information: Clocked dynamics in artificial spin ice

Johannes H. Jensen[1*†], Anders Strømberg[2*†], Ida Breivik[2], Arthur Penty[1], Miguel Angel Niño[3], Muhammad Waqas Khaliq[3], Michael Foerster[3], Gunnar Tufte[1], Erik Folven[2]

[1*]Department of Computer Science, Norwegian University of Science and Technology, Trondheim, Norway.
[2*]Department of Electronic Systems, Norwegian University of Science and Technology.
[3]ALBA Synchrotron Light Facility, Carrer de la Llum 2 – 26, Cerdanyola del Vallés, 08290, Barcelona, Spain.

*Corresponding author(s). E-mail(s): johannes.jensen@ntnu.no; anders.stromberg@ntnu.no;
†These authors contributed equally to this work.

# 1 Supplementary Figures

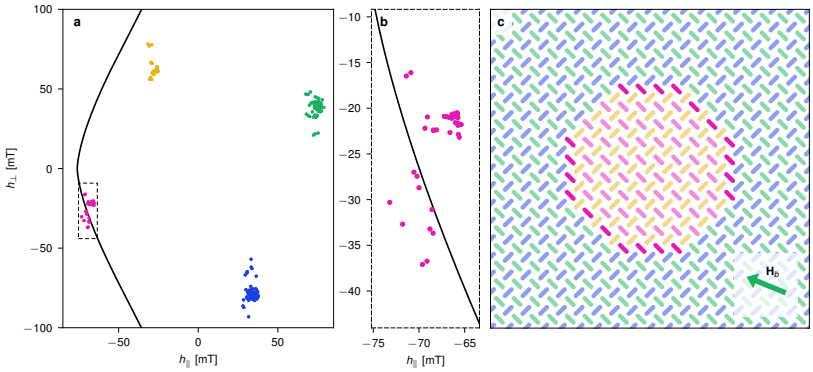


**Fig. 1** Astroid clusters showing relative locations of all the magnets within their respective switching astroids. The plots show **a-b**, astroid clusters during reversal, when the pinwheel system shown in **c** is subject to the negative clock field $\mathbf{H}_b$. Each dot represents the total field $\mathbf{h}_i = \mathbf{H}_b + \mathbf{h}_{\text{dip}}^{(i)}$ experienced by a magnet $i$, projected onto its parallel ($h_\parallel$) and perpendicular ($h_\perp$) axis. Note that the positive direction of the parallel component is with respect to the magnetization direction of each nanomagnet. **b**, astroid clusters during reversal have a different structure compared to growth. Switchable magnets outside the astroid are highlighted in **c**. During reversal, the switchable magnets are along both the horizontal, vertical and $-45°$ domain walls. Switchable magnets along the horizontal domain wall is attributed to the curvature of the inner domain.

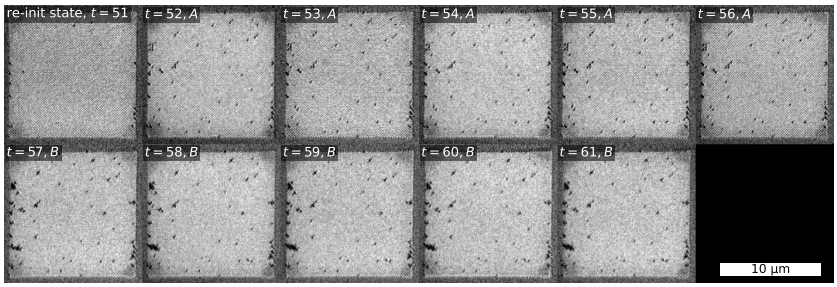


**Fig. 2** XMCD-PEEM images of the control experiment. The system is reinitialized at $t = 51$ (following from Fig. 7 in the main text), and $t$ is incremented by 1 for each clock step, with clock pulses indicated by the labels. The first $A$ clock pulse promotes dark (rightwards) magnets, equivalent to half a clock cycle, while subsequent applications of $A$ incurs no further change. When the clock pulse is changed to $B$, dark (rightwards) magnets are again promoted, equivalent to the second half of an $AB$ clock cycle. Furthermore, additional $B$ clock pulses incurs no change in the state.

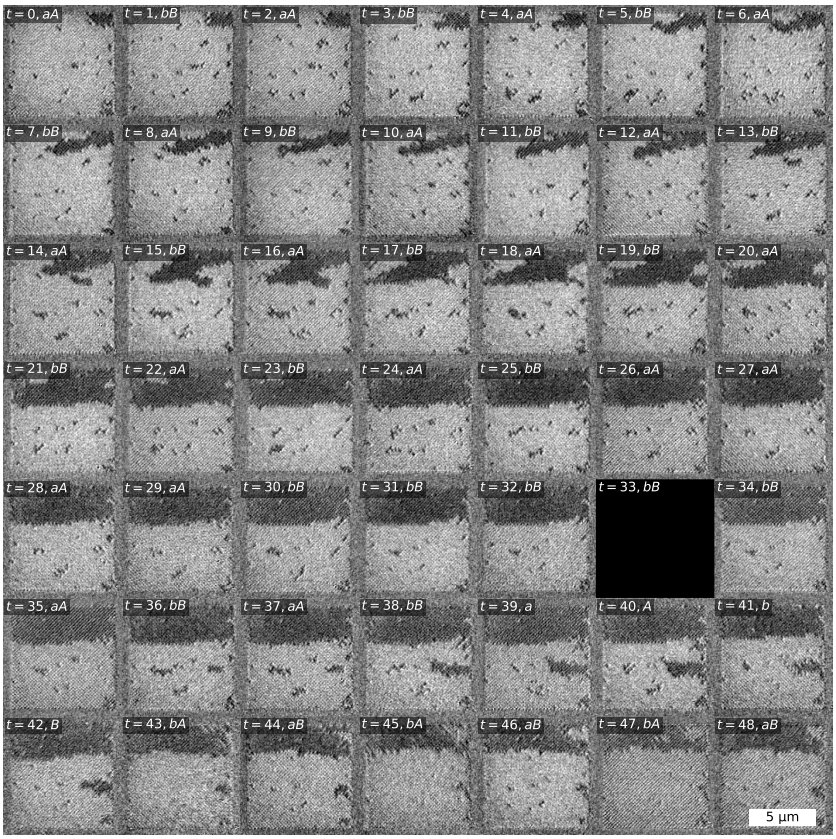


**Fig. 3** XMCD-PEEM images of all steps from the bipolar clock protocol series. The time starts at $t = 0$, and is incremented by 1 for each image, with clock pulses indicated by the labels. The black (rightwards) domains grow and change shape as the $aAbB$ protocol is applied. There are two control series where $aA$ and $bB$ are applied, where no change occurs. Note that there is missing data for $t = 33$, but the ensemble was still subjected to the clock pulses. At $t = 39$ we image after each single clock pulse. From $t = 42$ the reverse protocol $BbAa$ is applied, and the black (rightwards) domains shrink. Note that during the reversal protocol we still image after a final $A$ or $B$ pulse, in order to keep a constant image shift.

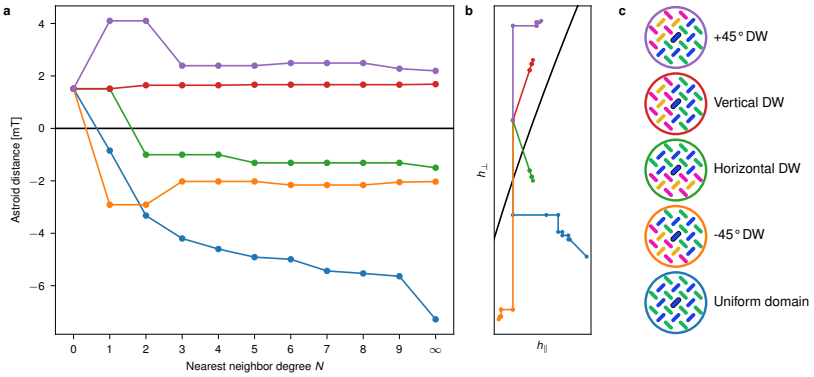


**Fig. 4** Minimum distance to the astroid edge as the neighborhood is increased, for the highlighted blue magnet in the center of each scenario in **c**. Each scenario is color-coded according to the circles in **c**. In all cases, the clock field $\mathbf{H}_A$ is applied, as defined in Fig. 1 in the main text. **a**, distance to the astroid for the highlighted magnet, as the neighborhood is increased when calculating the dipolar fields. For each nearest neighbor degree $N$, the dipolar fields include all magnets within a radius of the $N$th nearest neighbor. **b**, trace of the position within the astroid as the nearest neighbor degree $N$ is increased. Each dot represents the total field projected onto the parallel ($h_\parallel$) and perpendicular ($h_\perp$) axis of the blue center magnet. The positive direction of the parallel component is with respect to the magnetization direction of the nanomagnet. Note that the scenarios all start at the same point (no neighbors), then diverge.

# 2 Supplementary Discussion

## 2.1 Neighborhood interactions

Here we analyse what type of neighbor interactions causes switching to occur selectively along the vertical and +45° domain walls. We consider five different prototype cases shown in Fig. 4c: a uniform blue/green (leftwards) domain, and two domains separated by horizontal, vertical, and ±45° domain walls (DWs). Within each prototype case, the subject of study is the highlighted blue magnet in the center. The circled insets in the figure show only a limited neighborhood in the center of a larger $50 \times 50$ system which is initialized according to each prototype case.

Fig. 4a plots the distance to the astroid for the center magnet, as the number of neighbors are increased when calculating the dipolar fields. For each nearest neighbor degree $N$, the dipolar fields include all magnets within a radius of the $N$th nearest neighbor (NN). After adding the total dipolar field to the external clock field $H_A$, the shortest distance to the astroid is calculated. We define astroid distance as positive outside the astroid and negative inside.

Astroid distance is plotted for each of the five prototype cases in Fig. 4c. With zero neighbors, and hence no dipolar fields, all five cases start at the same point outside the astroid. As the first NNs are included, the cases split into four: the uniform domain and the −45° domain wall enter the astroid. In other words, the dipolar fields from the first NNs stabilize and prevent switching in these two cases. Including also the second

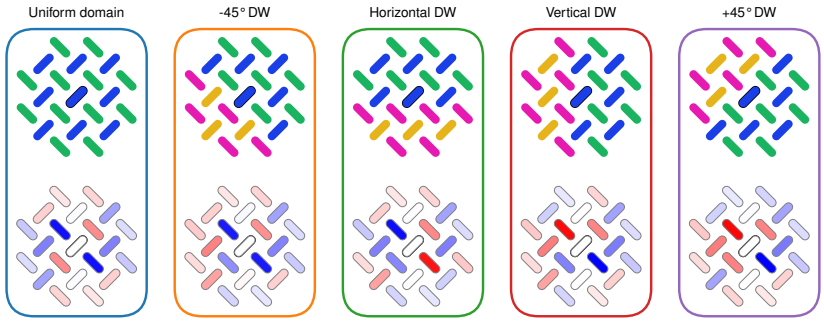


**Fig. 5** Neighborhood influence with respect to center magnet, for nearest neighbor degree 1-4. Each scenario depicts the magnetization state (top) and the corresponding influence of the neighbors (bottom). In all cases, the clock field $\mathbf{H}_A$ is applied, as defined in Fig. 1 in the main text. Stronger red signifies that the magnet is biasing the center magnet *towards* switching, and stronger blue signifies that the magnet is biasing the center magnet *away* from switching.

NNs causes the horizontal domain wall to enter the astroid. Horizontal domain walls are hence stabilized by 2nd NN interactions. For the horizontal and $-45°$ domain walls, astroid distance does not change significantly as the neighborhood is increased further. For the uniform domain, however, astroid distance increases further as the number of NNs are increased, with significant stabilizing interactions also beyond 9NNs.

Next, we consider the two cases where switching *does* occur, namely the vertical and $+45°$ domain walls. Somewhat curious, the astroid distance for the vertical domain wall appears to stay nearly constant across all NNs. The $+45°$ domain walls travel further outside the astroid due to 1st NN interactions, then the 3rd NN interactions bring it closer to the astroid again, after which it remains at a near-constant distance.

Fig. 4b shows a trace of the location within the astroid as the NNs are increased. For the vertical domain wall (red line), there is indeed movement due to dipolar interactions, but the movement is exclusively *parallel* to the astroid edge. Hence, the astroid distance in this case remains constant. For the $+45°$ domain wall (purple line), the movement is purely in the perpendicular ($h_\perp$) direction for the 1st NN interactions, then purely parallel ($h_\parallel$) from the 3rd NN fields.

An even more detailed picture is provided in Fig. 5, where each neighbor magnet is colored according to the contribution of its dipolar field. Specifically, a magnet is colored red (blue) if its dipolar field pushes the center magnet further out of (into) the astroid. The shade of red (blue) represents how much the dipolar field contributes to promote (prevent) switching of the center magnet. A magnet is colored white if its dipolar field has no contribution on the resulting astroid distance.

As can be seen in Fig. 5, the neighborhood in the uniform domain is dominated by magnets that prevent switching (colored blue), with the highest contribution from the first NNs along the hard axis of the center magnet. The same subset of the NNs are also the primary stabilizing force of the $-45°$ DW. For the horizontal DW case,

the dipolar fields from the first NNs cancel out, and it is the second NNs that prevent switching.

For the vertial DW, there is an apparent symmetry between neighbors that prevent and promote switching. As a result the vertical DW is not stabilized and hence easily switched. We saw earlier how this is because the dipolar fields are directed parallel to the astroid edge. The +45° DW is the least stable, where 3/4 of the first NNs promote switching (colored red).

## 2.2 Growth and reversal in bipolar clocking

During bipolar clocking, domain growth and reversal in a single clock cycle can be observed for several domain wall configurations. Fig. 6 shows the time evolution of different types of domain walls, subject to $aAbB$ clocking. A straightforward example of simultaneous growth and reversal can be seen in Fig. 6d, which shows a +45° domain wall. Notice that the first clock pulse $a$ moves the domain wall one step towards the left, and hence a reversal of the orange/pink domain. However, the subsequent $A$ pulse immediately undoes this change *and* moves the domain wall another step towards the right, advancing the domain wall a total of two layers of the sublattice $L_a$ (orange magnets). Next, the $b$ pulse has no effect, since the pink magnets along the domain wall are stabilized by the dipolar fields from their neighbors. Finally, the $B$ pulse moves the domain another step towards the right, flipping the next layer of magnets from sublattice $L_b$ (from green to pink). As can be seen, the result is an apparent growth of the orange/pink domain by a single layer along the domain wall. The other domain wall cases in Fig. 6 also show simultaneous growth and reversal, but are not discussed in further detail.

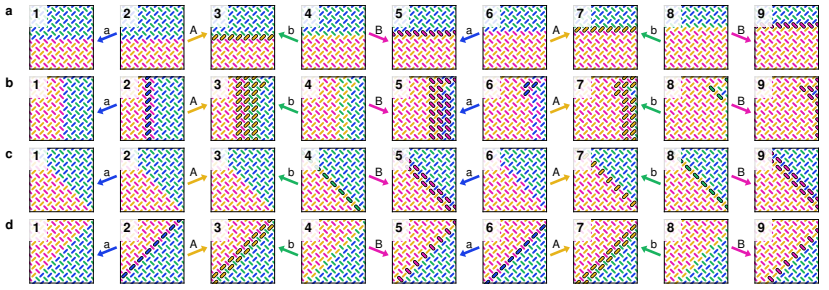


**Fig. 6** Bipolar $aAbB$ clocking of four types of domain walls in pinwheel ASI: **a**, horizontal DW, **b**, vertical DW, **c**, −45° DW and **d**, +45° DW. Each domain wall is initialized to fill the whole $50 \times 50$ system from edge to edge. Each snapshot shows a zoomed-in view of the system, at different points during a clock protocol. (1) shows the initial state. (2-12) show the state during $aAbB$ clocking. Magnets that change state between snapshots are highlighted by a solid black outline.

There is an apparent competition between growth and reversal. For the +45° domain wall discussed earlier, the competition seems to favor growth. However, the

situation strongly depends on the particular shape of the domain. Fig. 10 in the main text shows the time evolution of a hexagonal domain subject to $aAbB$ clocking. As can be seen, the domain both grows horizontally and reverses vertically, and hence gradually changes shape over time. Since vertical domain reversal depends on the curvature of the domain, the process will stop when the domain grows too wide. The domain will continue to grow horizontally, as horizontal domain growth is not dependent on curvature. As a result, domain growth seems to out-compete reversal in this case. The end result is an apparent tendency towards horizontally elongated domains.

*This page is intentionally left blank*